

AD \_\_\_\_\_

Award Number: W81XWH-08-1-0128

TITLE: Real-Time Tracking of Implanted Markers During Radiation Treatment by Use  
of Simultaneous kV and MV Imaging

PRINCIPAL INVESTIGATOR: Rodney D. Wiersma, Ph.D.

CONTRACTING ORGANIZATION: Stanford University School of Medicine  
Stanford, CA 94305

REPORT DATE: March 2009

TYPE OF REPORT: Final

PREPARED FOR: U.S. Army Medical Research and Materiel Command  
Fort Detrick, Maryland 21702-5012

DISTRIBUTION STATEMENT: Approved for Public Release;  
Distribution Unlimited

The views, opinions and/or findings contained in this report are those of the author(s) and should not be construed as an official Department of the Army position, policy or decision unless so designated by other documentation.

REPORT DOCUMENTATION PAGE				Form Approved OMB No. 0704-0188	
Public reporting burden for this collection of information is estimated to average 1 hour per response, including the time for reviewing instructions, searching existing data sources, gathering and maintaining the data needed, and completing and reviewing this collection of information. Send comments regarding this burden estimate or any other aspect of this collection of information, including suggestions for reducing this burden to Department of Defense, Washington Headquarters Services, Directorate for Information Operations and Reports (0704-0188), 1215 Jefferson Davis Highway, Suite 1204, Arlington, VA 22202-4302. Respondents should be aware that notwithstanding any other provision of law, no person shall be subject to any penalty for failing to comply with a collection of information if it does not display a currently valid OMB control number. <b>PLEASE DO NOT RETURN YOUR FORM TO THE ABOVE ADDRESS.</b>					
1. REPORT DATE 1 March 2009		2. REPORT TYPE Final		3. DATES COVERED 1 Feb 2008 – 1 Dec 2008	
4. TITLE AND SUBTITLE  Real-Time Tracking of Implanted Markers During Radiation Treatment by Use of Simultaneous kV and MV Imaging				5a. CONTRACT NUMBER	
				5b. GRANT NUMBER W81XWH-08-1-0128	
				5c. PROGRAM ELEMENT NUMBER	
6. AUTHOR(S)  Rodney D. Wiersma, Ph.D.  E-Mail: wriersma@uchicago.edu				5d. PROJECT NUMBER	
				5e. TASK NUMBER	
				5f. WORK UNIT NUMBER	
7. PERFORMING ORGANIZATION NAME(S) AND ADDRESS(ES)  Stanfor University School of Medicine Stanford, CA 94305				8. PERFORMING ORGANIZATION REPORT NUMBER	
9. SPONSORING / MONITORING AGENCY NAME(S) AND ADDRESS(ES) U.S. Army Medical Research and Materiel Command Fort Detrick, Maryland 21702-5012				10. SPONSOR/MONITOR'S ACRONYM(S)	
				11. SPONSOR/MONITOR'S REPORT NUMBER(S)	
12. DISTRIBUTION / AVAILABILITY STATEMENT Approved for Public Release; Distribution Unlimited					
13. SUPPLEMENTARY NOTES					
14. ABSTRACT In the presence of organ motion, geometric target uncertainty can hamper the benefits of highly conformal dose techniques such as IMRT. A critical step in dealing with intra-fraction prostate tumor motion is the real-time monitoring of the tumor position. The aim of this investigation is the first time demonstration of a real-time 3D internal fiducial tracking system based on onboard kV diagnostic imaging together with a MV electronic portal-imaging device (EPID). A Varian radiotherapy system equipped with both kV and MV imaging systems was used in this work. An in house built marker detection tool using prior CT based knowledge was created to locate gold cylindrical markers in the kV/MV frames. The geometric tracking capabilities of the system were evaluated using a pelvic phantom with embedded fiducials placed on a 3D moveable stage to mimic actual prostate motion. The maximum 3D tracking speed of the kV-MV system is approximately 9 Hz. The geometric accuracy of the system is found to be on the order of less than 1 mm in all three spatial dimensions. This investigation has demonstrated the use of a real-time 3D fiducial tracking system using combined kV and MV imaging for the first time.					
15. SUBJECT TERMS IMRT, IGRT, Real-Time, Tracking, MV Imaging, kV Imaging					
16. SECURITY CLASSIFICATION OF:			17. LIMITATION OF ABSTRACT  UU	18. NUMBER OF PAGES  70	19a. NAME OF RESPONSIBLE PERSON USAMRMC
a. REPORT U	b. ABSTRACT U	c. THIS PAGE U			19b. TELEPHONE NUMBER (include area code)

## Table of Contents

	<u>Page</u>
Introduction.....	4
Body.....	4
Key Research Accomplishments.....	8
Reportable Outcomes.....	8
Conclusion.....	10
References.....	10
Appendices.....	11

## **I. INTRODUCTION**

The postdoctoral fellowship grant was awarded to the principal investigator (PI) for the period of Feb. 1, 2008—Dec. 1, 2008. The aim of this investigation is the development of a near real-time 3D internal fiducial tracking system based on the combined use of kilo-voltage (kV) and mega-voltage (MV) imaging. Specific goals of the proposal included: (1) initial system setup and configuration; (2) creation of image processing and analysis algorithms; and (3) evaluation of the overall performance of the MV-kV technique. Under the generous support from the U.S. Army Medical Research and Materiel Command (AMRMC), the PI has contributed significantly to the radiation treatment of prostate cancer. Several conference abstracts and refereed papers have been resulted from the support. The fellowship also allowed the PI to obtain research training in prostate cancer while accomplishing the proposed projects. The preliminary data and research opportunity gained under the support of this grant has enabled the PI to obtain a faculty instructor position in the Department of Radiation and Cellular Oncology at The University of Chicago.

## **II. RESEARCH AND ACCOMPLISHMENTS**

In radiation therapy (RT), creating a highly conformal dose distribution to a static 3D target is largely solved by techniques such as intensity modulated radiation therapy (IMRT)<sup>1, 2</sup>. What remains problematic is how to take into account the dynamic nature of human anatomy, where both inter- and intra-fraction organ motion can limit target dose conformity<sup>3, 4</sup> and therefore local tumor control<sup>5</sup>. Tumor motion can be addressed by increasing the planning target volume (PTV) to include the entire range of motion of the target, however, usually at the cost of irradiating more healthy tissues. Other techniques used to address tumor motion are direct patient intervention through breath-hold techniques<sup>6</sup>, or the delivery of radiation only when the target is in a known geometric location by the use of gating<sup>7-10</sup>. These techniques transform the problem of targeting a moving tumor into a more easily manageable static treatment case. Ideally, one would like to deliver highly conformal radiation, as provided by IMRT in the static case, to a moving target without beam interruption or patient intervention. Promising candidates in this direction include tumor tracking by moving the radiation source itself<sup>11-13</sup> or the beam defining multi-leaf collimator (MLC)<sup>14-16</sup>.

To successfully guide a gating or a tracking RT delivery system, a real-time knowledge of the target geometric location is necessary. Several methods of obtaining the real-time tumor position are available, and these can be categorized as being either indirect (surrogate-based) or direct (fiducial/image) in nature. In general, indirect tumor location methods, such as external skin marker tracking<sup>10, 17, 18</sup> or breath monitoring techniques<sup>19</sup>, rely on the correlation between external body parameters and the tumor. In reality, the relationship between external parameters and internal organ motion is complex and a large uncertainty may be present in predicting the tumor location based on external signals<sup>20, 21</sup>. The unreliable correlation represents one of the weakest links in the quality

chain of respiration-gated and 4D RT. A direct tumor position measurement is highly desirable for therapeutic guidance.

With the emergence of RT machines equipped with both onboard kV imaging and EPID, the potential exists to obtain the tumor position in real-time during the radiation delivery process through a combined use of the MV treatment beam and kV projection images. In this proposal we report our implementation of such a real-time 3D tracking system and demonstrate that a spatial accuracy of  $< 1$  mm is achievable in tracking fiducials using the proposed technique. The method takes advantage of the MV-kV imaging devices already mounted on commercially available treatment machines, thus providing an easily implemented method for monitoring intra-fractional tumor motion. Since projection data containing 2D target information is obtained using the actual treatment beam, the proposed method only requires the use of one kV source in gaining the other spatial dimension necessary for full 3D target localization. Compared to other fluoroscopic tracking systems, which require the use of two or more additional kV x-ray imaging systems, the technique may offer potential radiation sparing to the patient and overall system cost reductions. With the use of real-time spatial trajectory information of fiducials, it is hoped that uncertainties in intra-fraction target localization can be greatly reduced, thus ensuring a more accurate delivery of the planned conformal dose distribution.

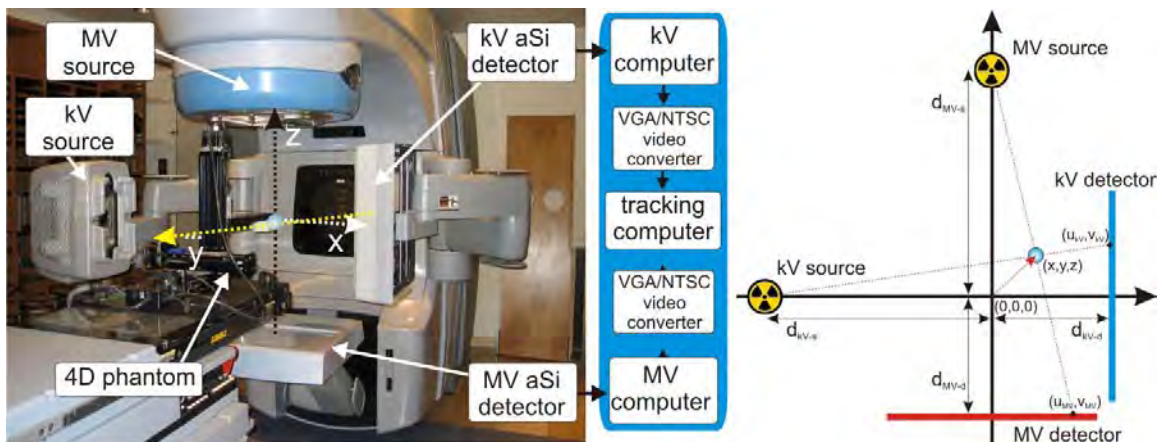


**Fig. 1: Varian Trilogy with MV and kV imagers in extended positions (left). Laboratory frame of reference is denoted by dashed arrows. A 4D stepper motor phantom is located on the couch. Process paths used for image acquisition are indicated. Right is a geometric sketch detailing variables used for calculation of a marker's  $(x, y, z)$  position from isocenter  $(0,0,0)$ . The xz-plane is shown with the y-axis pointing out of the page.**

Fig. 1 shows the experimental setup used for real-time 3D MV-kV tracking. The maximum frames per second (fps) obtainable from the MV and kV detectors currently are 9.5 Hz and 15 Hz, respectively. The kV and MV source detector distances (SDD) were set to 180 cm and 150 cm, respectively, though in principle this can be varied to a wide variety of distances as allowed by the robotic arms (Fig. 1).

With orthogonally placed MV and kV imagers on the gantry the detected marker's projection on the images can be converted to real-space  $(x,y,z)$  locations from system

isocenter using the geometric relationships depicted in Fig. 1 and given by the following relations (Eq. 1 – 4),

$$\frac{x_{MV}}{d_{MV-s} + d_{MV-d}} = \frac{x}{d_{MV-s} - z} \quad (1)$$

$$\frac{y_{MV}}{d_{MV-s} + d_{MV-d}} = \frac{y}{d_{MV-s} - z} \quad (2)$$

$$\frac{x_{kV}}{d_{kV-s} + d_{kV-d}} = \frac{z}{d_{kV-s} + x} \quad (3)$$

$$\frac{y_{kV}}{d_{kV-s} + d_{kV-d}} = \frac{y}{d_{kV-s} + x} \quad (4)$$

Here (x,y,z) corresponds to the marker's position from system isocenter. The MV and kV photon source-to-isocenter distances are given by dMV-s and dkV-s, respectively. The isocenter to MV and kV detector distances are given by dMV-d and dkV-d, respectively. The algorithm also takes into account gantry angle ( $\theta$ ) by use of a rotational transform matrix equation to connect the systems frame of reference with that of the laboratory,

$$\begin{bmatrix} \cos \theta & 0 & \sin \theta \\ 0 & 1 & 0 \\ -\sin \theta & 0 & \cos \theta \end{bmatrix} \begin{pmatrix} x \\ y \\ z \end{pmatrix} = \begin{pmatrix} x' \\ y' \\ z' \end{pmatrix} \quad (5)$$

where (x',y',z') denotes the marker's coordinates from system isocenter in the lab's frame of reference.

A dedicated image processing PC was used to process and analyze both kV and MV video streams simultaneously as detailed in Fig. 1. Initially, an intensity-based filter was used to segment the metallic markers from the captured MV and kV images, however it was found that for the MV images, an intensity based method was problematic when the marker was moving in the vicinity of high density objects such as bone. Additionally, the inherent low contrast of EPID imaging between different material densities is problematic for successful fiducial identification. We have therefore replaced with filter with a template matching algorithm as recently reported by Mao et al.<sup>22</sup>.

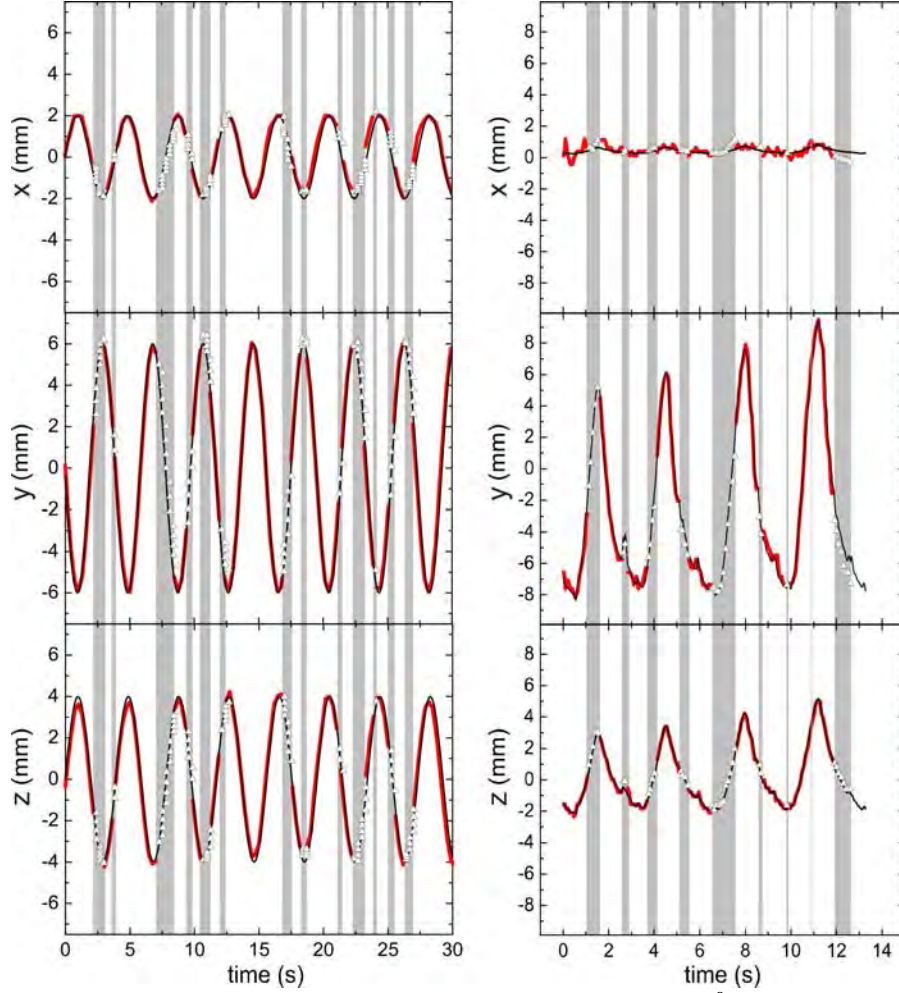


**Fig. 2:** Tracked geometric 3D motion of a marker over time for the 180° gantry angle during a SS-IMRT delivery for an oscillating phantom (left) and for a simulated lung patient (right). Grey strips correspond to MV beam interrupts or 'steps' of the MLC controller. The thick red line is the experimentally tracked motion using the MV-kV method. Triangles represent the use of correlation to estimate the markers position in the event of MV beam interruption. Thin black line is the pre-programmed motion.

The MV-kV method was evaluated using a programmable 4D motion platform (Fig. 1) to reproduce actual, irregular, patient motion data. Input trajectory files were created from pre-recorded lung tumor motion obtained using a Cyberknife Synchrony (Accuray, Palo Alto, CA). SS-IMRT lung plans originating from prior treated patients were used to reproduce the typical beam interrupts seen clinically. Fig. 2 highlights a portion of the tracked motion for lung patient #1 along the x, y, and z directions (thick red line) using a typical SS-IMRT plan. As shown, the MV-kV tracked motion agrees well with the actual inputted motion into the platform (thin black line). Grey strips represent tracked data gaps as the MV beam was interrupted due to MLC steps. The points (triangles) during the step portions correspond to where linear correlation was used to estimate the 3D coordinates during MV beam loss. Comparison of the measured to the actual inputted motion at this particular gantry angle reveals a RMSE of  $x = 0.16$  mm,  $y = 0.31$  mm, and  $z = 0.1$  mm. This error increases to a RMSE of  $x = 0.23$  mm,  $y = 0.62$  mm, and  $z = 0.21$  mm when only one imager is used for tracking together with an updated correlation model.

The correlation model used in Fig. 2 (triangles) was developed as a method to increase the robustness of MV-kV tracking. Radiation treatment modalities as step-and-shoot IMRT, where the treatment beam is turned off every time the MLC steps to a new segment, inherently contain MV beam interruptions. Additionally, dose sparing can be further improved by application of a correlation model together with MV-kV imaging since the kV beam can be turned off whenever tracking can be accomplished by the MV imager alone. It remains to be investigated as to what extent the kV imaging can be reduced with the prerequisite of maintaining continuous real-time 3D target tracking.

### **III. KEY RESEARCH ACCOMPLISHMENTS**

- First demonstration of a real-time 3D internal marker tracking system based on combined MV-kV imaging.
- Built an internal fiducial marker algorithm detection algorithm for the use of MV images.
- Developed a correlation algorithm for the MV-kV tracker to buffer against sudden imager interrupts and for potential kV diagnostic dose reduction.
- Demonstrated the first use of MV-kV tracking during arc radiotherapy.
- Several research groups have initiated projects involving MV-kV imaging and one radiotherapy equipment manufacture has shown interest in using MV-kV tracking in their future products.

### **IV. REPORTABLE OUTCOMES**

The following is a list of publications resulted from the grant support. Copies of the publication materials are enclosed with this report.

#### **Refereed Publications:**

- Wiersma R. D., Riaz N, Dieterich S, Suh Y, Xing L., Use of MV and kV imager correlation for maintaining continuous real-time 3D internal marker tracking during beam interruptions, *Phys Med Biol.*, 54 (1), 89-103 (2009)
- Liu W, Wiersma R. D., Mao W, Luxton G, Xing L., Real-time 3D internal marker tracking during arc radiotherapy by the use of combined MV-kV imaging, *Phys Med Biol.*, 53 (24), 7197-213 (2008)
- Mao W, Riaz N, Lee L, Wiersma R. D., Xing L., A fiducial detection algorithm for real-time image guided IMRT based on simultaneous MV and kV imaging, *Med Phys.*, 35 (8), 3554-64 (2008)
- Mao W, Wiersma R. D., Xing L., Fast internal marker tracking algorithm for onboard MV and kV imaging systems, *Med Phys.*, 35 (5), 1942-9 (2008)

- R. D. Wiersma, W. Mao, and L. Xing, Combined kV and MV imaging for real-time tracking of implanted fiducial markers, *Med. Phys.*, 35 (4), 1191-1198 (2008)

#### **Published Abstracts:**

- Wiersma, RD; Mao, W; Xing, L; Riaz, N, Prediction of Fiducial Motion in Respiratory Tumors for Image-Guided Radiotherapy, *MEDICAL PHYSICS* Volume: 35 Issue: 6 Pages: 2626-2626 Published: JUN 2008
- Wiersma, RD; Mao, W; Xing, L; Luxton, G, Liu, W; Riaz, N, Nearly Real-Time Tumor Position Monitoring During Arc Therapy with Combined MV and kV Imaging, *MEDICAL PHYSICS* Volume: 35 Issue: 6 Pages: 2626-2626 Published: JUN 2008
- Wiersma, RD; Mao, W; Lee, K; Xing, L, Riaz, N, Tracking Multiple Moving Fiducials During Treatment Based on Simultaneous Onboard kV and Treatment MV Imaging, *MEDICAL PHYSICS* Volume: 35 Issue: 6 Pages: 2621-2621 Published: JUN 2008
- Riaz, N; Wiersma, RD; Mao, W; Xing, L, Improving Tracking of Implanted Radio-Opaque Markers on MV and kV Imaging with Techniques from Computer Vision and Machine Learning, *MEDICAL PHYSICS* Volume: 35 Issue: 6 Pages: 2618-2618 Published: JUN 2008
- Wiersma, RD; Mao, W; Riaz, N; Xing, L, Use of Synchronized Beam Switching for Real-Time 3D kV-MV Internal Marker Tracking with Step-and-Shoot IMRT, *MEDICAL PHYSICS* Volume: 35 Issue: 6 Pages: 2598-2598 Published: JUN 2008
- Mao, W; Riaz, N; Lee, K; Wiersma, RD; King, C;Hsu, A; Luxton, G; Xing, L, Using Treatment Beam Imaging to Monitor Prostate Motion in Near Real-Time On a Conventional LINAC, *MEDICAL PHYSICS* Volume: 35 Issue: 6 Pages: 2634-2634 Published: JUN 2008
- Wiersma, RD; Mao, W; Riaz, N; Xing, L, Real-time tracking of implanted fiducial markers using combined kV and MV imaging, *MEDICAL PHYSICS* Volume: 35 Issue: 6 Pages: 2634-2634 Published: JUN 2008

#### **Patents Filed:**

Number: Disclosure #S07-268 Stanford Office of Technology Licensing (OTL)

Title: *3D geometric tracking of human anatomy as a function of time using combined kV and MV x-ray imaging*

## New Employment:

With the help of this grant and associated publications, the PI has obtained a faculty position at the Instructor level in the Department of Radiation and Cellular Oncology at The University of Chicago. The PI would like to continue his research in using MV-kV tracking for prostate cancer treatment and to contribute to better prostate patient care by application to the 2009 DOD New Investigator Award.

## V. CONCLUSION

A real-time 3D fiducial tracking system using combined kV and MV imaging has been successfully demonstrated for the first time. This technique is especially suitable for RT systems already equipped with on board kV and EPID imaging devices. The geometric accuracy of the system is found to be on the order of 1 mm in all three spatial dimensions. Given its simplicity and achievable accuracy, the proposed approach, should find widespread clinical application in real-time monitoring of the tumor position and in providing control signal to respiration-gated and even 4D radiation therapy.

## References:

- <sup>1</sup> AAPM IMRT Sub-committee, Medical Physics **30**, 2089 (2003).
- <sup>2</sup> L. Xing, Y. Wu, Y. Yang, and A. L. Boyer, in *Intensity Modulated Radiation Therapy: A Clinical Perspective*, edited by A. J. Mundt and J. C. Roeske (BC Decker Inc., Hamilton & London, 2005), p. 20.
- <sup>3</sup> H. Shirato, Y. Seppenwoolde, K. Kitamura, R. Onimura, and S. Shimizu, *Seminars in Radiation Oncology* **14**, 10 (2004).
- <sup>4</sup> L. Xing, B. Thorndyke, E. Schreibmann, Y. Yang, T. F. Li, G. Y. Kim, G. Luxton, and A. Koong, *Med Dosim* **31**, 91 (2006).
- <sup>5</sup> M. van Herk, *Seminar in Radiation Oncology* **14**, 52 (2006).
- <sup>6</sup> J. Hanley, et al., *Int J Radiat Oncol Biol Phys* **45**, 603 (1999).
- <sup>7</sup> H. D. Kubo, P. M. Len, S. Minohara, and H. Mostafavi, *Medical physics* **27**, 346 (2000).
- <sup>8</sup> S. S. Vedam, P. J. Keall, V. R. Kini, and R. Mohan, *Medical Physics* **28**, 2139 (2001).
- <sup>9</sup> X. A. Li, C. Stepaniak, and E. Gore, *Med Phys* **33**, 145 (2006).
- <sup>10</sup> N. Wink, M. Chao, J. Antony, and L. Xing, *Physics in Medicine and Biology*, submitted. (2007).
- <sup>11</sup> A. Schweikard, G. Glosser, M. Bodduluri, M. J. Murphy, and J. R. Adler, *Comput. Aided Surg.* **5**, 263 (2000).
- <sup>12</sup> P. J. Keall, K. Wijesooriya, S. Vedam, R. George, D. Todor, M. Murphy, J. Siebers, J. Williamson, and R. Mohan, *International Journal of Radiation Oncology Biology Physics* **60**, S338 (2004).
- <sup>13</sup> C. Ozhasoglu, *Medical Physics* **33**, 2245 (2006).
- <sup>14</sup> P. J. Keall, V. R. Kini, S. S. Vedam, and R. Mohan, *Physics in Medicine and Biology* **46**, 1 (2001).

- 15 T. Neicu, H. Shirato, Y. Seppenwoolde, and S. B. Jiang, *Physics in Medicine and*  
16 *Biology* **48**, 587 (2003).  
17 L. Papiez, *Mathematical and Computer Modelling* **37**, 735 (2003).  
18 H. D. Kubo and B. C. Hill, *Physics in Medicine and Biology* **41**, 83 (1996).  
19 C. Ozhasoglu and M. J. Murphy, *International Journal of Radiation Oncology*  
20 *Biology Physics* **52**, 1389 (2002).  
21 L. Simon, P. Giraud, V. Servois, and J. C. Rosenwald, *International Journal of*  
22 *Radiation Oncology Biology Physics* **63**, 602 (2005).  
S. S. Vedam, V. R. Kini, P. J. Keall, V. Ramakrishnan, H. Mostafavi, and R.  
Mohan, *Medical Physics* **30**, 505 (2003).  
J. D. P. Hoisak, K. E. Sixel, R. Tirona, P. C. F. Cheung, and J. P. Pignol,  
*International Journal of Radiation Oncology Biology Physics* **60**, 1298 (2004).  
W. Mao, R. D. Wiersma, and L. Xing, *Medical Physics* **35**, 1942 (2008).

**Appendix. Copies of manuscripts (see attachment)**

## Use of MV and kV imager correlation for maintaining continuous real-time 3D internal marker tracking during beam interruptions

R D Wiersma, N Riaz, Sonja Dieterich, Yelin Suh and L Xing

Department of Radiation Oncology, Stanford University School of Medicine, Stanford, CA 94305-5847, USA

E-mail: [r.wiersma@stanford.edu](mailto:r.wiersma@stanford.edu)

Received 14 August 2008, in final form 5 November 2008

Published 5 December 2008

Online at [stacks.iop.org/PMB/54/89](http://stacks.iop.org/PMB/54/89)

### Abstract

The integration of onboard kV imaging together with a MV electronic portal imaging device (EPID) on linear accelerators (LINAC) can provide an easy to implement real-time 3D organ position monitoring solution for treatment delivery. Currently, real-time MV–kV tracking has only been demonstrated by simultaneous imaging by both MV and kV imaging devices. However, modalities such as step-and-shoot IMRT (SS-IMRT), which inherently contain MV beam interruptions, can lead to loss of target information necessary for 3D localization. Additionally, continuous kV imaging throughout the treatment delivery can lead to high levels of imaging dose to the patient. This work demonstrates for the first time how full 3D target tracking can be maintained even in the presence of such beam interruption, or MV/kV beam interleave, by use of a relatively simple correlation model together with MV–kV tracking. A moving correlation model was constructed using both present and prior positions of the marker in the available MV or kV image to compute the position of the marker on the interrupted imager. A commercially available radiotherapy system, equipped with both MV and kV imaging devices, was used to deliver typical SS-IMRT lung treatment plans to a 4D phantom containing internally embedded metallic markers. To simulate actual lung tumor motion, previous recorded 4D lung patient motion data were used. Lung tumor motion data of five separate patients were inputted into the 4D phantom, and typical SS-IMRT lung plans were delivered to simulate actual clinical deliveries. Application of the correlation model to SS-IMRT lung treatment deliveries was found to be an effective solution for maintaining continuous 3D tracking during ‘step’ beam interruptions. For deliveries involving five or more gantry angles with 50 or more fields per plan, the positional errors were found to have  $\leq 1$  mm root mean squared error (RMSE) in all three spatial directions. In addition to increasing the robustness of MV–kV tracking against beam interruption, it was also found that use of correlation can be an effective way of lowering kV dose

to the patient and for increasing kV image quality by reduction of MV scatter interference.

(Some figures in this article are in colour only in the electronic version)

## 1. Introduction

In radiation therapy (RT), creating a highly conformal dose distribution to a static 3D target is largely solved by techniques such as intensity modulated radiation therapy (IMRT) (AAPM IMRT Sub-committee, 2003, Xing *et al* 2005). What remains problematic is how to take into account the dynamic nature of human anatomy, where both inter- and intra-fraction organ motion can limit target dose conformity (Shirato *et al* 2004, Xing *et al* 2006) and therefore local tumor control (van Herk 2006). Techniques as beam gating (Kubo *et al* 2000, Li *et al* 2006, Wink *et al* 2008) and beam tracking by moving the radiation source itself (Schweikard *et al* 2000, Ozhasoglu 2006) or the beam defining multi-leaf collimator (MLC) (Keall *et al* 2001, Neicu *et al* 2003, Papiez 2003) address this issue, and potentially can reduce normal tissue complications while increasing local control through dose escalation to mobile tumors in the thorax and abdomen. Such techniques necessitate precise geometrical tumor knowledge at all times. Recently, real-time 3D tumor position tracking during the actual radiation delivery has been demonstrated by use of MV treatment beam imaging combined with kV imaging (Wiersma *et al* 2008). Unlike stereoscopic kV-based methods, which require two or more kV sources for 3D marker positioning (Shirato *et al* 1999, Berbeco *et al* 2004), only one kV source is required for full geometric information of the implanted markers since the actual MV treatment beam is used for positioning. This is particularly beneficial to LINACs pre-equipped with both an onboard kV imager and an electronic portal imaging device (EPID) since the MV–kV method can be implemented without significant hardware upgrades. Additionally, the use of the MV beam for geometric tumor information reduces the total imaging dose needed for tracking since only one kV source is needed compared to other techniques using multiple kV sources.

Currently, the MV–kV tracking method has only been demonstrated when both MV and kV images are acquired simultaneously (Wiersma *et al* 2008). However, in actual clinical situations, continuous and uninterrupted acquisition of both MV and kV image data simultaneously is generally not feasible. Radiation treatment modalities as step-and-shoot IMRT (SS-IMRT), where the treatment beam is turned off every time the MLC steps to a new segment, inherently contain MV beam interruptions. Such interruptions would lead to geometric tracking errors due to loss of MV target information. In this work, we provide a solution for allowing continuous real-time MV–kV tracking even in the event of MV or kV beam interruption through the use of correlation between the MV–kV imagers.

The central idea of our approach is that even when one imaging beam is off, two positional degrees of freedom of the actual target are still measured by the other imager, leading to a strong dimensional correlation that can be used to estimate the missing degree of freedom. The main prerequisites for the technique are (1) the establishment of a correlation model based on prior target information and (2) that at least one imaging source, either the MV or kV imager, is available at the specific instant of time during the delivery. To lower the chance of target positional error, a moving time window approach is used to continuously update the correlation function. This differs from other correlation methods, which initially establish an external to internal marker correlation function at the beginning, and then only periodically update this function every 30–60 s (Kanoulas *et al* 2007). Applied to step-and-shoot IMRT,

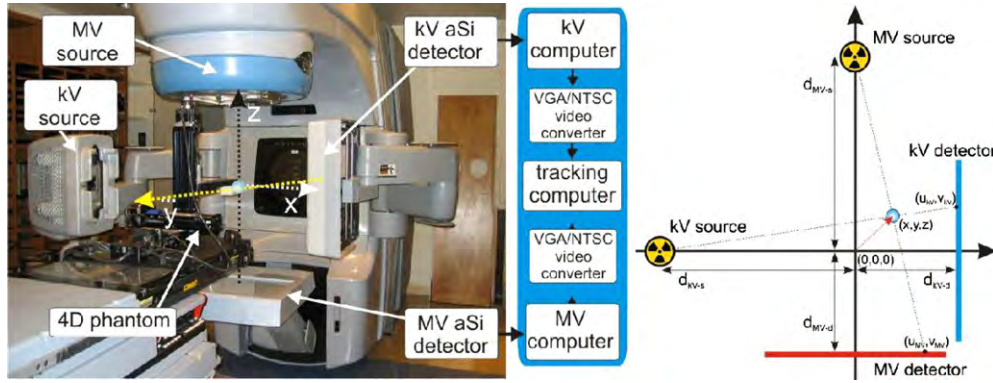


**Figure 1.** Varian trilogy with MV and kV imagers in extended positions (left). Laboratory frame of reference is denoted by dashed arrows. A 4D stepper motor phantom is located on the couch. Process paths used for image acquisition are indicated. Right is a geometric sketch detailing variables used for calculation of a marker's  $(x, y, z)$  position from the isocenter  $(0, 0, 0)$ . The  $xz$  plane is shown with the  $y$ -axis pointing out of the page.

the method allows continuous real-time 3D marker tracking by taking both MV and kV images during the ‘shoot’ portions and only kV images during the ‘step’ portions.

One of the primary motivators of using external-to-internal correlation for fluoroscopic tracking systems based on multiple kV  $x$ -ray sources is to reduce the imaging dose cost to the patient (Kanoulas *et al* 2007, Schweikard *et al* 2000, Murphy 2004). MV–kV tracking is naturally advantageous in this aspect, since projection data containing 2D target information are obtained using the actual treatment beam without additional imaging dose to the patient. Thus, for full 3D target localization, only one kV source is required, effectively lowering the imaging dose to the patient in comparison with other stereoscopic kV tracking systems.

## 2. Materials and method

### 2.1. Hardware set-up

A Varian Trilogy<sup>TM</sup> system (Varian Medical Systems, Palo Alto, CA) operating in the 6 MV photon mode was used for this study. Images of the MV beam were acquired using an amorphous silicon (aSi) EPID (PortaVision MV aS-1000, Varian Medical Systems, Palo Alto, CA) attached to the LINAC as shown in figure 1. The kV imaging was obtained by using the onboard kV imaging system located perpendicular to the treatment beam. The device consists of a 125 kV  $x$ -ray tube together with an aSi flat panel imager (PaxScan 4030CB, Varian Medical Systems, Salt Lake City, UT). The kV imager has a pixel area of 40 cm  $\times$  30 cm with a pixel pitch of 388  $\mu$ m, corresponding to a maximum resolution of 1024  $\times$  768. The MV detector has a pixel width of 392  $\mu$ m and a maximum resolution of 1024  $\times$  768, corresponding to a 40 cm  $\times$  30 cm effective area of detection. The maximum frames per second (fps) obtainable from the kV and MV detectors in this work are 15 Hz and 9.5 Hz, respectively. Both kV and MV source-to-detector distances (SDD) were set to 150 cm.

### 2.2. MV–kV cylindrical marker detection and 3D localization

A previously reported in-house pattern matching algorithm specifically designed for both MV- and kV-based images was used to segment the cylindrical markers from the image

background (Mao *et al* 2007). The detection algorithm employed a two criteria system based on a correlation score and a scaling factor to extract the spatial coordinates of the fiducials. This allowed successful marker detection even on MV images where inherent low contrast can make image-intensity-based marker detection difficult.

Two coordinate systems were used; the system frame of reference can rotate with the gantry, whereas the laboratory frame depicted in figure 1 is fixed in space. Therefore, the system and laboratory reference frames are connected to a simple rotational transform around the superior–inferior (SI) axis:

$$\begin{bmatrix} \cos \theta & 0 & \sin \theta \\ 0 & 1 & 0 \\ -\sin \theta & 0 & \cos \theta \end{bmatrix} \begin{pmatrix} x' \\ y' \\ z' \end{pmatrix} = \begin{pmatrix} x \\ y \\ z \end{pmatrix} \quad (1)$$

where  $\theta$  denotes the gantry angle and  $x$ ,  $y$  and  $z$  denote the marker's coordinates away from isocenter in the laboratory frame of reference. After the detection of the marker's center-of-mass on the imager (denoted by  $(u_{kV}, v_{kV})$  and  $(u_{MV}, v_{MV})$ ), the marker locations from system isocenter were calculated using the following relations:

$$\frac{u_{kV}}{d_{kV-s} + d_{kV-d}} = \frac{z'}{d_{kV-s} + x'} \quad (2)$$

$$\frac{v_{kV}}{d_{kV-s} + d_{kV-d}} = \frac{y'}{d_{kV-s} + x'} \quad (3)$$

$$\frac{u_{MV}}{d_{MV-s} + d_{MV-d}} = \frac{x'}{d_{MV-s} - z'} \quad (4)$$

$$\frac{v_{MV}}{d_{MV-s} + d_{MV-d}} = \frac{y'}{d_{MV-s} - z'}. \quad (5)$$

Here  $x'$ ,  $y'$  and  $z'$  correspond to the marker's position relative to isocenter where the isocenter is defined at 100 cm SSD and the center of the MV beam. The MV and kV photon source-to-isocenter distances are denoted by  $d_{MV-s}$  and  $d_{kV-s}$ , respectively. The isocenter to kV and MV detector distances are given by  $d_{kV-d}$  and  $d_{MV-d}$ , respectively.

### 2.3. MV–kV imager correlation

SS-IMRT leads to frequent interruption of MV image acquisition as the MV beam is turned off for each step instance during delivery (figure 2(a)). Loss of either the MV or kV detector will prevent full 3D localization since the coordinates  $(u, v)$  provided by a single detector are insufficient to solve equations (2)–(5) for  $x$ ,  $y$  and  $z$ . However, under appropriate circumstances, the two-dimensional position of a marker in the imager plane  $(u, v)$  can still provide valuable tracking information. Such real-time information, together with appropriate correlation models and prediction algorithms, can provide an accurate estimation of the full 3D position of the marker. Although theoretically a marker could move independently in all three dimensions, the nature of human anatomy and the physiology behind common tumor movements (e.g. respiration) would suggest that a marker's motion in one dimension should be correlated with its motion in another dimension. In this work, we take advantage of this inter-dimensional correlation to maintain the 3D position of the tumor even when one imager is shut off. Here we build a model consisting of a moving linear regression with a sliding window for the training period.

To further elucidate this concept, let us consider the geometrical arrangement in figure 1. Here the kV imager is recording the anterior–posterior ( $u_{kV}$ ) and superior–inferior ( $v_{kV}$ )

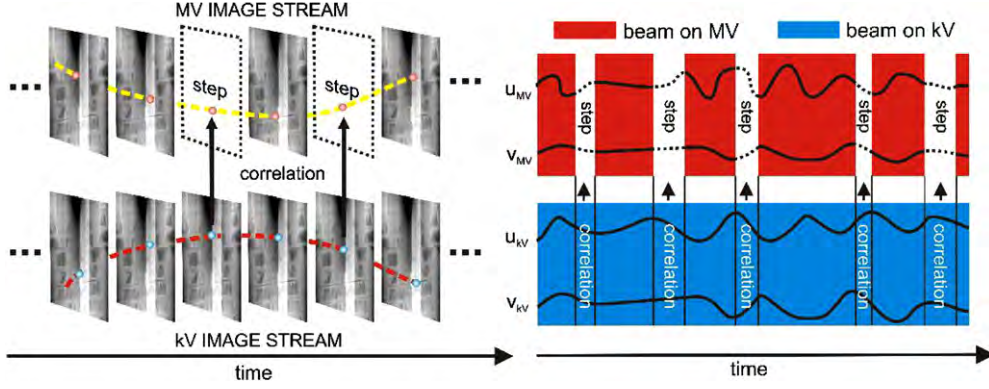


**Figure 2.** Use of kV imaging to fill in missing ‘step’ gaps through a correlation model (left). The right panel shows the detected marker coordinates as a function of time. Black arrows represent time intervals when kV information data are used together with correlation to compensate for missing geometric information during beam interruption. Note that  $v_{kV}$  and  $v_{MV}$  are redundant along the y-axis.

directions of motion. Since the imagers are orthogonal, this means the MV imager is recording the position of the target in the left–right ( $u_{kV}$ ) and superior–inferior ( $v_{MV}$ ) directions. When the MV imager is off during the step portions on an IMRT plan, we can easily determine  $v_{MV}$  from  $v_{kV}$  after adjusting for differences in source-to-imager differences between the two imaging systems, since both imagers are recording the movement of the target in the same direction. However, the kV imager does not provide us with any information about the position of the maker in the left–right or ( $u_{MV}$ ) direction. If we assume that the motion of a target is not independent in all three dimensions, but rather correlated, we can construct a linear regression function relating ( $u_{MV}$ ) to the two dimensions measured on the kV imager as

$$u_{MV}(t) = \sum_{i=0}^p (a_i u_{kV}(t-i) + b_i v_{kV}(t-i)), \quad (6)$$

where  $a_i$  and  $b_i$  are coefficients determined by ordinary least-squares regression and  $p$  is the number of prior positions to consider. Hence, the unknown dimension can be determined as a linear combination of the other two known dimensions. Before one can start correlating the unknown dimension, one needs to determine the coefficients above,  $a_i$  and  $b_i$ . This can be accomplished with a relatively short training period ( $N_{\text{train}}$ ) of as little as 10 frames ( $\sim 1$  s), where the full 3D information is determined by both imagers simultaneously. We can solve for the coefficients by using the so-called normal equations from traditional linear regression, where

$$X = \begin{bmatrix} u_{kV}(t) & \dots & u_{kV}(t-p) & v_{kV}(t-p) & \dots & v_{kV}(t-p) \\ \vdots & & & & & \\ u_{kV}(t-i) & \dots & u_{kV}(t-i-p) & v_{kV}(t-i-p) & \dots & v_{kV}(t-i-p) \\ \vdots & & & & & \\ u_{kV}(t-N_{\text{train}}) & \dots & u_{kV}(t-N_{\text{train}}-p) & v_{kV}(t-N_{\text{train}}-p) & \dots & v_{kV}(t-N_{\text{train}}-p) \end{bmatrix}$$

and

$$Y = \begin{bmatrix} u_{MV}(t) \\ \vdots \\ u_{MV}(t-N_{\text{train}}) \end{bmatrix}. \quad (7)$$

Then the coefficient vector  $B$  can be determined by

$$Y = BX, \quad (8)$$

and is solvable using standard mathematical software packages. The number of prior positions to use ( $p$  in equation (6)) and the size of the training period ( $N_{\text{train}}$ ) are hyper-parameters of this model that were determined empirically by performing a grid search, varying  $p$  between 1 and 5 and the training set size between 10 and 100. We found  $p = 2$  and a training set size of 25 as optimal for minimizing the root mean squared error (RMSE). However, all values tested in these intervals gave reasonable RMSE values. These optimized values ( $p = 2$ ,  $N_{\text{train}} = 25$ ) were used for all analysis of the data presented in this work.

As the treatment progresses, the target may change its pattern of movement, and hence the original coefficients may no longer be accurate for computing the missing dimension. To account for such changes, the linear correlation model was continuously updated by recalculating the coefficients using the most recent 25 positions for which full 3D information was known as the training set. That is, our model consisted of moving linear regression with a sliding window for the training period. This model is similar to a local regression model considered by another group but used for a different purpose (Ruan *et al* 2007).

Using the above model, the missing  $u_{\text{MV}}$  and  $v_{\text{MV}}$  coordinates can be predicted during ‘step’ portions. Likewise, during loss of kV imaging, the missing  $u_{\text{kV}}$  and  $v_{\text{kV}}$  coordinates can be estimated from  $u_{\text{MV}}$  and  $v_{\text{MV}}$ . Having estimated the missing spatial information, it is relatively straightforward to calculate the markers’ positions from machine isocenter by use of equations (2)–(5). As shown in figure 2,  $v_{\text{kV}}$  and  $v_{\text{MV}}$  provide a redundant measurement along the laboratory y-axis and may be magnified due to different source-to-imagers distances.

#### 2.4. Performance evaluation

We evaluated our method with two phantom-based experiments: one consisting of simple sinusoidal motion and the other consisting of complex 4D motion generated from real patient treatment recordings. The first method experimentally investigated the accuracy of the MV–kV correlation method by sinusoidally moving a block of solid water (measuring  $5 \times 5 \times 10 \text{ cm}^3$ ) containing three embedded BB metallic markers (3 mm in diameter). A 4D motion platform (Washington University, St Louis, MO) holding the block of solid water (figure 1) was programmed to produce the oscillatory motion with a period of 4 s and amplitude of 4 mm, 12 mm and 8 mm in the  $x$ -,  $y$ - and  $z$ -directions, respectively. The ranges of motion investigated were chosen to correspond to the more extreme motion ranges observed in actual lung tumor cases (Keall *et al* 2006, Maxim *et al* 2007). The motion platform is capable of reproducing motion in accordance with a pre-programmed trajectory and was previously investigated to have an accuracy with a RMS trial-to-trial error of less than 0.2 mm from the inputted trajectory (Malinowski *et al* 2007).

The second experiment used the programmable 4D motion platform to reproduce actual, irregular, patient motion data. Input trajectory files were created from pre-recorded lung tumor motion obtained using a Cyberknife Synchrony (Accuray, Palo Alto, CA). The pre-recorded lung tumor motion data were obtained from five lung cancer patients treated in Georgetown University Hospital from July 2005 to January 2006 (table 1). The use of the data for research purposes was approved by the Georgetown Institutional Review Board (IRB-2005-309). Synchrony is a subsystem of the Cyberknife system (Adler *et al* 1997, Schweikard *et al* 2000, Murphy 2004) used to compensate for tumor motion during radiotherapy. The tracking system estimates the real-time 3D internal tumor positions by use of a correlation model linking external patient motion to internal fiducial locations, and by a prediction algorithm.

**Table 1.** Properties of the lung tumor motion data for the five different patients used in this study. The maximum (max), minimum (min), mean and standard deviation (SD) for the peak-to-trough distance and respiratory period are given. Note that each patient dataset represents motion recorded during a single radiotherapy fraction.

Patient	Peak-to-trough (mm)				Period (s)			
	Mean	Max	Min	SD	Mean	Max	Min	SD
Lung #1	14.4	19.9	7.1	1.9	3.4	6.4	2.4	0.4
Lung #2	12.5	16.9	3.9	2.2	5.1	8.5	2.0	0.9
Lung #3	7.0	21.8	1.5	1.7	2.6	6.4	1.8	0.5
Lung #4	10.3	22.2	3.2	2.4	3.8	8.8	1.3	0.5
Lung #5	8.5	28.0	0.9	1.9	5.3	8.2	2.5	0.8

**Table 2.** Properties of the three SS-IMRT lung plans used to quantify the performance of the MV-kV correlation method. ‘Total dose’ is the total dosage for a single fraction. ‘Beam dir.’ and ‘Segments’ correspond to the number of gantry angles and fields used, respectively. The time range for the MLC steps and treatment beam shoots are given for each plan.

Plan	Total dose (MU)	Dose rate (MU min <sup>-1</sup> )	Beam dir. #	Segments #	Step range (s)	Shoot range (s)
SS-IMRT #1	335	400	5	50	0.06–1.70	0.95–1.08
SS-IMRT #2	1298	400	5	60	0.27–1.94	1.74–5.43
SS-IMRT #3	499	400	7	76	0.16–1.70	0.99–1.50

Therefore, the tumor motion analyzed in this study is not actual, but estimated from the correlation model of the tracking system. The uncertainty of the tracking system motion data from the actual target motion has RMSEs of  $1.5 \pm 0.8$  mm (Suh *et al* 2008). The estimation errors could be due to inaccuracy of the correlation models of the tracking system, or temporal variations in the internal/external correlation model between measurements (Murphy 2004, Korreman *et al* 2008, Nishioka *et al* 2008). The uncertainty obtained for the current dataset ( $1.5 \pm 0.8$  mm) is consistent with the values published by Seppenwoolde *et al* (2007), who simulated the Synchrony method using respiratory and orthogonal fluoroscopic measured data in an eight-patient study. They concluded from their data that the systematic error of the position estimation was less than 1 mm for all patients and the mean 3D error was less than 2 mm for over 80% of the time.

SS-IMRT lung plans originating from three prior treated patients were used to reproduce the typical beam interrupts seen clinically (table 2). To simulate clinically seen step-and-shoot times, all SS-IMRT plans were delivered using the same dose rates and doses as originally used in the clinic. All SS-IMRT plans examined in the study were created using the Eclipse Treatment Planning System (Varian Medical Systems, Palo Alto, CA). The SS-IMRT plans were delivered to either the moving pelvic phantom or the cube of solid water attached to the 4D motion platform.

In general, the average step time was found to range from 0.68 to 1.00 s for the three SS-IMRT lung plans. This is primary governed by the MLC leaf that must undergo the maximal displacement from one segment to the next. Within a particular plan, step intervals have been observed to range from 0.06 to 1.94 s (table 2). The clinical dose rates used were 400 MU min<sup>-1</sup>, resulting in shoot times varying from 0.95 to 5.43 s (table 2).

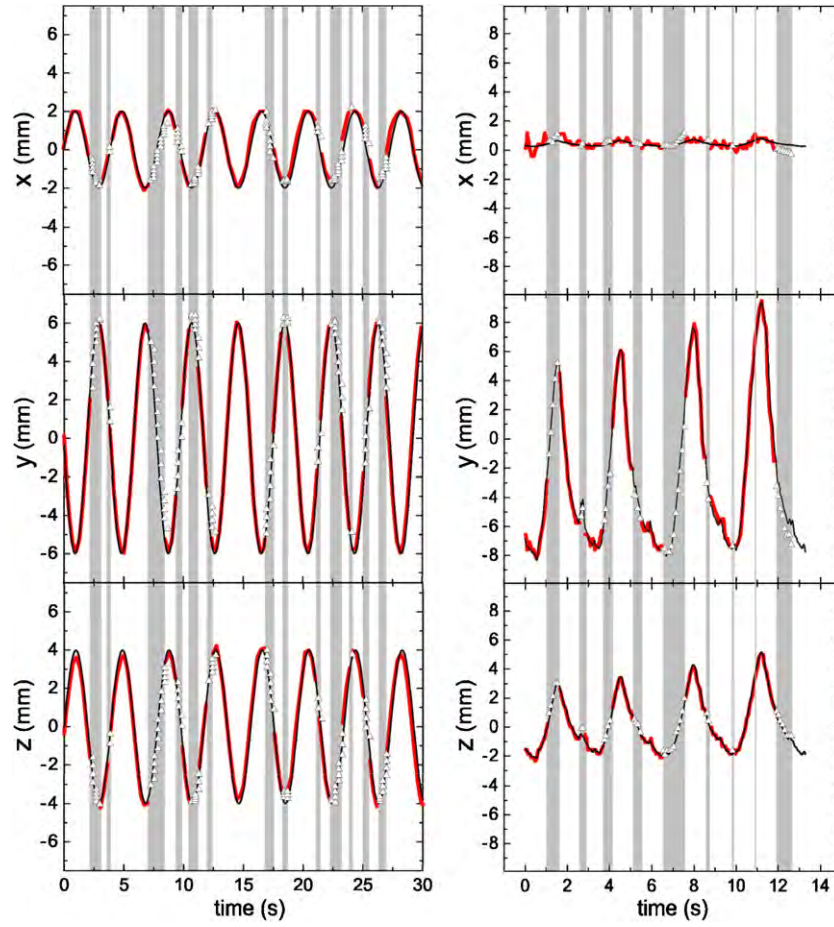


**Figure 3.** Tracked geometric 3D motion of a marker over time for the  $180^\circ$  gantry angle during a SS-IMRT #1 delivery for an oscillating phantom (left) and for a simulated lung patient 1 (right). Gray strips correspond to MV beam interrupts or ‘steps’ of the MLC controller. The thick line is the experimentally tracked motion using the MV–kV method. Triangles represent the use of correlation to estimate the markers position in the event of MV beam interruption. Thin line is the pre-programmed motion.

### 3. Results

As a preliminary study to demonstrate the accuracy of the correlation method to fill in missing geometric information during beam interruption, three stainless steel BBs (3 mm in diameter) were oscillated and a SS-IMRT plan delivered. A fixed amplitude of  $x = 4$  mm,  $y = 12$  mm,  $z = 8$  mm and a period to 4 s were inputted into the 4D stage. SS-IMRT plan 1 (table 2) was delivered using a  $400 \text{ MU min}^{-1}$  dose rate in 6 MV beam mode with both MV and kV imagers in cine acquisition mode. Figure 3(a) plots the theoretical sinusoidal curve (thin solid line) inputted in the motion stage together with the measured tracked data (thick line). As seen, gaps in the experimental data occur due to interruption of the MV beam by MLC steps. Step times for this particular plan range from a minimum of 0.06 s to a maximum of 1.7 s. Using the correlation model,  $u_{\text{MV}}$  and  $v_{\text{MV}}$  were estimated based on equation (6) and the marker motion along  $x$ ,  $y$  and  $z$  from the isocenter was calculated using equations (1)–(5) (symbolized

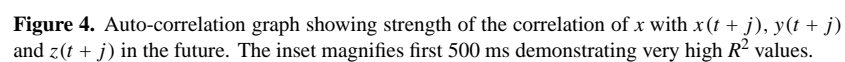
**Table 3.** Total geometric accuracy of using MV–kV to track internal markers during SS-IMRT delivery for five different lung patients while applying three different IMRT plans. RMSEs between theoretical and measured motion are expressed as the net displacement vector in the laboratory frame of reference. Linear correlation is used for prediction during MLC steps.

Motion	SS-IMRT #1 (mm)	SS-IMRT #2 (mm)	SS-IMRT #3 (mm)
Lung #1	0.40	0.47	0.36
Lung #2	0.13	0.51	1.05
Lung #3	0.54	0.86	0.60
Lung #4	0.50	0.31	0.11
Lung #5	0.23	0.19	0.25

by triangles). Comparison of the expected sinusoidal motion data to the experimental data, with exclusion of the step portions (gray strips), reveals a RMSE of 0.21 mm, 0.36 mm and 0.30 mm for the  $x$ ,  $y$  and  $z$  motion, respectively. This error corresponds to the MV–kV tracking precision with both MV and kV imagers recording simultaneously. Analyzing only the step regions, where the MV imager is off and the kV imager is on, and using the correlated model together with the kV imager data to predict marker positions reveal a slightly increased RMSE of 0.34 mm, 0.56 mm, and 0.41 mm for the  $x$ -,  $y$ - and  $z$ -directions, respectively.

In general, use of pure sinusoidal oscillation as in figure 3(a) is not representative of actual lung tumor motion and is relatively simple to predict with a correlation model. A more realistic model was performed by repeating the same experiment, but, with the use of actual patient 4D tumor motion data. Experimentally recorded 4D lung tumor data from five different patients were used to reproduce the motion of metallic fiducials internally embedded in lung tumors. The three SS-IMRT lung plans, summarized in table 2, were delivered to the moving phantom while imaging with both MV and kV imagers. Figure 3(b) highlights a portion of the tracked motion for lung patient 1 along the  $x$ -,  $y$ - and  $z$ -directions (thick line) using SS-IMRT plan 1 at the 180° gantry angle. As shown, the tracked motion agrees well with the actual inputted motion into the platform (thin black line). Gray strips represent tracked data gaps as the MV beam was interrupted due to MLC steps. The points (triangles) during the step portions correspond to where linear correlation was used to estimate the 3D coordinates during MV beam loss. Comparison of the measured to the actual inputted motion at this particular gantry angle reveals RMSEs of  $x = 0.16$  mm,  $y = 0.31$  mm and  $z = 0.1$  mm. These errors increase to RMSEs of  $x = 0.23$  mm,  $y = 0.62$  mm and  $z = 0.21$  mm when only one imager is used for tracking together with an updated correlation model. Analyzing all the correlated data gathered over the five different beam directions for SS-IMRT plan 1 leads to a net positional vector error of 0.40 mm. This experiment was repeated using the same lung patient motion data (lung patient 1), but using the other two treatment plans to account for a wide variety of different step-and-shoot times.

The lung-based tumor motions of five patients were reproduced and for each of these patients the three SS-IMRT plans were delivered to simulate many different clinical situations. To save space the main results are reported in table 3, which is a summary of the geometric accuracy when using a correlation model together with MV–kV tracking during SS-IMRT delivery. Results between the theoretically inputted stage motion and experimentally measured motion using correlation to fill in the MV beam interrupts are given as a net 3D vector RMSE. In all cases, it is found that the average deviation of the motion away from the expected even when using the correlation model is no greater than 1 mm. These high accuracies are surprising considering the simple correlation model used and demonstrate a strong inter-dimensional correlation present in lung-based tumors.



## 4. Discussion

A critical step needed to deal with intra-fraction tumor motion is the real-time monitoring of target position during the radiotherapy process. As demonstrated previously, MV–kV tracking holds key advantages over other solely fluoroscopy-based techniques since tracking can be accomplished with only one kV source, leading to reduced imaging radiation to the patient.

This work further strengthens the MV–kV tracking modality by using inter-dimensional tumor correlation to address the problem of MV or kV imager interruption during 4D MV–kV tracking, and, to our knowledge, constitutes the first of its kind. This is ideal for SS-IMRT, or other radiotherapy modalities, that may contain MV beam interruptions. Compared to indirect tumor location methods, such as external skin marker tracking (Kubo and Hill 1996, Ozhasoglu and Murphy 2002) or breath monitoring techniques (Simon *et al* 2005), where correlation is between external body parameters and the internal organ motion, the presented correlation scheme is much simpler in nature since a direct tumor position measurement is made with at least one imaging source. This leaves only one degree of freedom to be predicted by the correlation model, reducing the potential for error.

Clinically, it is envisioned that the correlation model would be implemented with MV–kV tracking during SS-IMRT using the following steps. (1) Pre-treatment patient set-up and positioning would proceed as according to standard protocols for the clinic. (2) SS-IMRT delivery of the first field would start. Both MV and kV imaging take place simultaneously during the first segment to build a training dataset. (3) Upon completion of the first segment, the kV beam would remain on and the MV beam would turn off for the MLC step. The real-time kV imager data together with the correlation model would be used to predict the 3D position of the target during the step time interval. (4) The MV beam turns on for the next segment and simultaneous MV–kV imaging occurs to update the correlation model. The process is repeated for the remaining steps of the particular field. During gantry rotation to the next field, both MV and kV beams would be switched off and the correlation model would be considered invalid. At the start of each field, steps 2–4 would be repeated. It is important to note that to allow for adequate training time at the start of the field, it may be necessary to reorganize the field segments in such a manner that the largest dose segment is delivered first. In the case when the model's coefficients cannot be constructed during the first segment, simultaneous MV–kV imaging may be carried over to the next segment, however, with an associated penalty in tracking accuracy taking place during the first MLC step. Nevertheless, even with the relatively simple correlation model used in this study, accurate 3D target predictions could be accomplished on lung tumor patients showing extreme target displacements in a training time of 1–4 s. With the use of improved prediction algorithms, and of a more sophisticated correlation model, it is expected that the training time can be further reduced, allowing accurate real-time 3D target prediction during the first MLC step.

Use of the kV imager at the initiation of therapy and for maintaining an accurate model, i.e. updating the model periodically, will add additional imaging dose to the patient. Positional information from the treatment beam (MV EPID images) is acquired with no additional dose to the patient. However, to properly update the model, kV images need to be acquired as well. In this study, we acquired kV images whenever MV images were being acquired; thus, additional dose would be proportional to the treatment time. Wen *et al* (2007) have reported that the dose to the soft tissue structures for a CBCT scan (with 630 images) is  $\sim 4$  cGy. At an acquisition speed of 15 fps, the kV dose is about  $0.1 \text{ cGy s}^{-1}$  ( $4 \text{ cGy}/630 \times (15 \text{ s}^{-1}) = 0.1 \text{ cGy s}^{-1}$ ). However, this represents a worse-case scenario, and it is envisioned that techniques as use of a lower frame rates and by turning off the kV beam whenever tracking can be accomplished with the MV beam and correlation/prediction models alone will significantly reduce the imaging dose. In terms of the initiation of therapy, prior 4D-CT scan information can also be used to build an initial correlation model. This method would require no additional dose to the patient but intra-fraction changes in respiratory pattern would not be accounted for until several maintenance steps have occurred.

In general, it is found that for both the oscillatory and actual lung tumor motion data, the resulting RMSE is largest in the y-direction. This increase in error can be attributed to two

processes: (1) experimentally induced motion artifacts and (2) increased difficulty of accurate prediction via the correlation model. The first issue (1) is attributed to hardware limitation of the imagers. It is found that the tracking error increases with increasing marker velocity. With the increased velocity, the captured marker images become more blurred and elongated (Wiersma *et al* 2008). This is primary due to the lower 9.5 Hz capture rate of the MV imager with respect to the 15 Hz capture rate of the kV imaging system. Since the SI direction (y-axis) is the direction of greatest motion for all experimentally investigated marker motions in this study, it is also the direction of the greatest experimental RMSEs. The second issue (2) leading to the larger RMSEs along the y-axis is again related to the greatest target motion occurring along the y-axis. In this case, the correlation model is more likely to predict a position away from the actual location due to increased displacements over a short time period. Nevertheless, the accuracy is still found to be acceptable for all the motions investigated.

Although a rather standard linear regression model was used in this work, the results are nevertheless found to be excellent, with a RMSE not exceeding 1 mm (table 3). We have also considered more complicated models including adaptive linear filters, support vector regression and regression trees in other motion prediction contexts (Riaz *et al* 2008); however, we did not pursue them in this case due to very good performance by the simple model employed. It is envisioned that with continual development and refinement, one of these more sophisticated techniques specifically suited to MV–kV tracking will lead to even further RMSE reductions. One current drawback of a simplified model though is that we do not directly account for hysteresis that is different for tumor trajectories on inspiration and exhalation. However, studies measuring the effects of hysteresis have found it to be present in only 50% of patients and generally of a small magnitude, namely 1–4 mm (Seppenwoolde *et al* 2002). Further, since we are tracking two coordinates of the tumor at all times, presumably all dimensions of tumor motion are undergoing hysteresis. This hypothesis seems plausible since our RMSE values are already very low, suggesting that we do not need to directly model hysteresis.

The RMSE associated with tracking using a single imager was found to be  $\leq 1$  mm and thus small. This is provided that a well-defined correlation model can be constructed and that the target can be detected by at least the MV or kV imager. This accuracy is more than suitable for compensating for the missing geometrical information provided by the kV imager. It is therefore a natural extension of this work to use correlation to further reducing the imaging dose to the patient by turning off the kV beam whenever tracking can be accomplished by the MV imager alone. It remains to be investigated as to what extent the kV imaging can be reduced with the prerequisite of maintaining continuous real-time 3D target tracking. It is assumed that kV imaging will be necessary during MLC step portions and that occasional kV imaging will be necessary during shoot portions for correlation model updating. Additionally, for small beam interruption or MLC step times in the 200–400 ms range, it is envisioned that a suitable prediction algorithm can fill in the missing geometric information, foregoing the need to turn on the kV imager. Currently, due to manufacture constraints, we do not have the ability to gate, or turn on and off, the kV radiation source; however, in the future we expect this feature to become available.

When using larger phantoms, it was found that scattered radiation from the treatment beam could deteriorate kV image quality when large MV beam defining apertures are used (Wiersma *et al* 2008). This was especially noticed for isocenter-to-imager distances of  $d_{\text{kV-d}} \leq 70$  cm. The scattered MV radiation superimposes over the kV imaging beam at the kV aSi detector, making fiducial detection more difficult. Use of MV–kV imager correlation offers a potential solution since only one imager can accomplish 3D tracking. By controlled MV and kV beam gating, such that the amount of time when both the MV and kV source are

simultaneously on is minimized, possible MV scatter interference could be reduced during the kV imaging process.

A possible scenario that would lead to a failure of the MV–kV correlation technique is the case where internal fiducial marker motion is strictly in the out of plane direction of the kV imager. Data collected with this imager would result in zero detectable motion, preventing correlation from being used during MLC step intervals. In this case, it may be necessary to resort to a prediction algorithm to provide 3D positional data of the internal fiducial markers. However, it is important to note that in analyzing five different patients at various gantry angles we have detected no instances of this strictly out of plane, or zero detectable, motion occurring for either the MV or kV imagers. In all cases, the residual in-plane detected motion was found to be adequate for application of the correlation model. This is attributed to respiratory tumors having motion primary in the superior–inferior direction, which is a common axis to both MV–kV imagers (figure 1), and thus detectable. It remains to be seen if other tumor sites, as the prostate, are more susceptible to this type of motion and if a strong inter-dimensional correlation exists. This is under current investigation and will be reported in future work.

## 5. Conclusion

This work has demonstrated for the first time how full 3D target tracking can be maintained even in the presence of beam interruption by use of MV–kV tracking together with a relatively simple correlation model. It is found that a strong inter-dimensional correlation exists between the  $x$ ,  $y$  and  $z$  degrees of freedom for lung tumor motion, and that this can be used advantageously for the prediction of missing geometric information during either MV or kV imager interruption. Application of a correlation model to SS-IMRT lung treatment deliveries demonstrates a positional accuracy of  $\leq 1$  mm in all three spatial directions. Additionally, the use of correlation allows for further reduction of kV imaging dose to the patient and can increase kV image quality by reducing MV scatter interference. Such improvements increase the robustness of MV–kV tracking, making it a viable solution for future real-time target monitoring in the clinic.

## Acknowledgments

This work was supported in part by grants from the Department of Defense Prostate Cancer Research Program (PC073690) and National Cancer Institute (1R01 CA98523 and CA104205).

## Appendix

An ACF shows the strength of the correlation degrading with time. A point estimate of the correlation coefficient is shown at time point zero—that is the correlation between  $x$  and  $y$ ,  $x$  and  $z$ , and  $y$  and  $z$  can be determined by looking at time point zero on the graph. In time series analysis, auto-correlation is defined as

$$R(t, s) = \frac{E[(X_t - \mu)(X_s - \mu)]}{\sigma^2},$$

where  $E$  is the expected value operator,  $X_t$  is the position of the fiducial in one particular dimension at time  $t$ ,  $X_s$  is the position at time  $s$  and  $\mu$  is the mean position of the fiducial in that dimension.  $R(t, s)$  can vary between  $-1$  and  $1$ ; however, we plot  $R(t, s)^2$  to demonstrate the strength of the relationship. The graph demonstrates the correlation between a point  $t$  some

points in the future,  $t + j$ , where  $j$  is plotted on the  $x$ -axis. The two other lines on the graph are not technically auto-correlations, but represent a similar concept of the correlation between one dimension and another dimension as time progresses.

## References

- AAPM IMRT Sub-committee 2003 Guidance document on delivery, treatment planning, and clinical implementation of IMRT: report of the IMRT subcommittee of the AAPM radiation therapy committee *Med. Phys.* **30** 2089–115
- Adler J R, Chang S D, Murphy M J, Doty J, Geis P and Hancock S L 1997 The cyberknife: a frameless robotic system for radiosurgery *Stereotact. Funct. Neurosurg.* **69** 124–8
- Berbeco R I, Jiang S B, Sharp G C, Chen G T Y, Mostafavi H and Shirato H 2004 Integrated radiotherapy imaging system (IRIS): design considerations of tumour tracking with linac gantry-mounted diagnostic x-ray systems with flat-panel detectors *Phys. Med. Biol.* **49** 243–55
- Kanoulas E, Aslam J A, Sharp G C, Berbeco R I, Nishioka S, SHIRATO H and Jiang S B 2007 Derivation of the tumor position from external respiratory surrogates with periodical updating of the internal/external correlation *Phys. Med. Biol.* **52** 5443–56
- Keall P J *et al* 2006 The management of respiratory motion in radiation oncology report of AAPM Task Group 76 *Med. Phys.* **33** 3874–900
- Keall P J, Kini V R, Vedam S S and Mohan R 2001 Motion adaptive x-ray therapy: a feasibility study *Phys. Med. Biol.* **46** 1–10
- Korremans S S, Juhler-Notttrup T and Boyer A L 2008 Respiratory gated beam delivery cannot facilitate margin reduction, unless combined with respiratory correlated image guidance *Radiother. Oncol.* **86** 61–8
- Kubo H D and Hill B C 1996 Respiration gated radiotherapy treatment: a technical study *Phys. Med. Biol.* **41** 83–91
- Kubo H D, Len P M, Minohara S and Mostafavi H 2000 Breathing-synchronized radiotherapy program at the University of California Davis Cancer Center *Med. Phys.* **27** 346
- LI X A, Stepaniak C and Gore E 2006 Technical and dosimetric aspects of respiratory gating using a pressure-sensor motion monitoring system *Med. Phys.* **33** 145–54
- Malinowski K, Noel C, LU W, Lechleiter K, Hubenschmidt J, Low D and Parikh P 2007 Development of the 4D phantom for patient-specific, end-to-end radiation therapy QA *SPIE 6510—Medical Imaging, Physics of Medical Imaging, 65100E (San Diego, CA, USA)* ed J Hsieh and M J Flynn
- Mao W, Wiersma R D and Xing L 2007 Fast internal marker tracking algorithm for onboard MV and kV imaging systems *Med. Phys.* **35** 1942–49
- Maxim P G, Loo B W, Shirazi H, Thorndyke B, Luxton G and LE Q T 2007 Quantification of motion of different thoracic locations using four-dimensional computed tomography: implications for radiotherapy planning *Int. J. Rad. Oncol. Biol. Phys.* **69** 1395–401
- Murphy M J 2004 Tracking moving organs in real time *Semin. Radiat. Oncol.* **14** 91–100
- Neicu T, Shirato H, Seppenwoolde Y and Jiang S B 2003 Synchronized moving aperture radiation therapy (SMART): average tumour trajectory for lung patients *Phys. Med. Biol.* **48** 587–98
- Nishioka S, Nishioka T, Kawahara M, Tanaka S, Hiromura T, Tomita K and Shirato H 2008 Exhale fluctuation in respiratory-gated radiotherapy of the lung: a pitfall of respiratory gating shown in a synchronized internal/external marker recording study *Radiother. Oncol.* **86** 69–76
- Ozhasoglu C 2006 Synchrony—real-time respiratory compensation system for the CyberKnife *Med. Phys.* **33** 2245–6
- Ozhasoglu C and Murphy M J 2002 Issues in respiratory motion compensation during external-beam radiotherapy *Int. J. Radiat. Oncol. Biol. Phys.* **52** 1389–99
- Papiez L 2003 The leaf sweep algorithm for an immobile and moving target as an optimal control problem in radiotherapy delivery *Math. Comput. Model.* **37** 735–45
- Riaz N, Wiersma R, Mao W and Xing L 2008 Prediction of Fiducial motion in respiratory tumors for image-guided radiotherapy *Med. Phys.* **35** 2626
- Ruan D, Fessler J A and Balter J M 2007 Real-time prediction of respiratory motion based on local regression methods *Phys. Med. Biol.* **52** 7137–52
- Schweikard A, Glosser G, Bodduluri M, Murphy M J and Adler J R 2000 Robotic motion compensation for respiratory movement during radiosurgery *Comput. Aided Surg.* **5** 263–77
- Seppenwoolde Y, Berbeco R I, Nishioka S, Shirato H and Heijmen B 2007 Accuracy of tumor motion compensation algorithm from a robotic respiratory tracking system: a simulation study *Med. Phys.* **34** 2774–84
- Seppenwoolde Y, Shirato H, Kitamura K, Shimizu S, Van Herk M, Lebesque J V and Miyasaka K 2002 Precise and real-time measurement of 3D tumor motion in lung due to breathing and heartbeat, measured during radiotherapy *Int. J. Radiat. Oncol. Biol. Phys.* **53** 822–34

- Shirato H, Seppenwoolde Y, Kitamura K, Onimura R and Shimizu S 2004 Intrafractional tumor motion: lung and liver *Semin. Radiat. Oncol.* **14** 10–8
- Shirato H, Shimizu S, Shimizu T, Nishioka T and Miyasaka K 1999 Real-time tumour-tracking radiotherapy *Lancet* **353** 1331–2
- Simon L, Giraud P, Servois V and Rosenwald J C 2005 Lung volume assessment for a cross-comparison of two breathing-adapted techniques in radiotherapy *Int. J. Radiat. Oncol. Biol. Phys.* **63** 602–9
- Suh Y, Dieterich S, Cho B and Keall P J 2008 An analysis of thoracic and abdominal tumour motion for stereotactic body radiotherapy patients *Phys. Med. Biol.* **53** 3623–40
- Van Herk M 2006 Errors and margins in radiotherapy *Semin. Radiat. Oncol.* **14** 52–64
- Wen N, Guan H Q, Hammoud R, Pradhan D, Nurushev T, Li S D and Movsas B 2007 Dose delivered from Varian's CBCT to patients receiving IMRT for prostate cancer *Phys. Med. Biol.* **52** 2267–76
- Wiersma R D, Mao W H and Xing L 2008 Combined kV and MV imaging for real-time tracking of implanted fiducial markers *Med. Phys.* **35** 1191–8
- Wink N M, Chao M, Antony J and Xing L 2008 Individualized gating windows based on four-dimensional CT information for respiration-gated radiotherapy *Phys. Med. Biol.* **53** 165–75
- Xing L, Thorndyke B, Schreiber E, Yang Y, Li T F, Kim G Y, Luxton G and Koong A 2006 Overview of image-guided radiation therapy *Med. Dosim.* **31** 91–112
- Xing L, Wu Y, Yang Y and Boyer A L 2005 Physics of intensity modulated radiation therapy *Intensity Modulated Radiation Therapy: A Clinical Perspective* ed A J Mundt and J C Roeske (Hamilton, London: BC Decker)

## Real-time 3D internal marker tracking during arc radiotherapy by the use of combined MV–kV imaging

W Liu, R D Wiersma, W Mao, G Luxton and L Xing

Department of Radiation Oncology, Stanford University School of Medicine, Stanford, CA 94305-5847, USA

E-mail: [wuliu@stanford.edu](mailto:wuliu@stanford.edu)

Received 5 September 2008, in final form 5 November 2008

Published 28 November 2008

Online at [stacks.iop.org/PMB/53/7197](http://stacks.iop.org/PMB/53/7197)

### Abstract

To minimize the adverse dosimetric effect caused by tumor motion, it is desirable to have real-time knowledge of the tumor position throughout the beam delivery process. A promising technique to realize the real-time image guided scheme in external beam radiation therapy is through the combined use of MV and onboard kV beam imaging. The success of this MV–kV triangulation approach for fixed-gantry radiation therapy has been demonstrated. With the increasing acceptance of modern arc radiotherapy in the clinics, a timely and clinically important question is whether the image guidance strategy can be extended to arc therapy to provide the urgently needed real-time tumor motion information. While conceptually feasible, there are a number of theoretical and practical issues specific to the arc delivery that need to be resolved before clinical implementation. The purpose of this work is to establish a robust procedure of system calibration for combined MV and kV imaging for internal marker tracking during arc delivery and to demonstrate the feasibility and accuracy of the technique. A commercially available LINAC equipped with an onboard kV imager and electronic portal imaging device (EPID) was used for the study. A custom built phantom with multiple ball bearings was used to calibrate the stereoscopic MV–kV imaging system to provide the transformation parameters from imaging pixels to 3D world coordinates. The accuracy of the fiducial tracking system was examined using a 4D motion phantom capable of moving in accordance with a pre-programmed trajectory. Overall, spatial accuracy of MV–kV fiducial tracking during the arc delivery process for normal adult breathing amplitude and period was found to be better than 1 mm. For fast motion, the results depended on the imaging frame rates. The RMS error ranged from ~0.5 mm for the normal adult breathing pattern to ~1.5 mm for more extreme cases with a low imaging frame rate of 3.4 Hz. In general, highly accurate real-time tracking of implanted

markers using hybrid MV–kV imaging is achievable and the technique should be useful to improve the beam targeting accuracy of arc therapy.

(Some figures in this article are in colour only in the electronic version)

## 1. Introduction

Arc-based radiotherapy modalities (Crooks *et al* 2003, Yu 1995, Ramsey *et al* 2001, Wong *et al* 2002, Cameron 2005, Otto 2008, Verellen *et al* 1997, 1998), such as conformal arc, RapidArc volumetric arc therapy (Varian Medical Systems, Palo Alto, CA, USA) (rapidArc 2008) and volumetric intensity modulated arc therapy (VMAT) (Elekta Corporate, Stockholm, Sweden) (VMAT 2008), have recently become available for clinical use. These techniques are capable of delivering therapeutic radiation dose to the tumor target while simultaneously moving the MLC leaves and the gantry. Both dose rate and gantry speed can vary. For certain types of diseases, arc therapy demonstrated marked advantages over conventional intensity modulated radiation therapy (IMRT). For prostate treatment, Palma *et al* (2008) report that the variable dose rate VMAT technique resulted in more favorable dose distributions than the conventional IMRT technique with much reduced monitor units. In addition to generating superior dose distribution for deep-seated tumors, an important advantage of arc-based therapy is its fast delivery, which may significantly increase the clinical throughput.

The increased dose conformality of the new arc-based delivery schemes poses more stringent requirement on beam targeting (Xing *et al* 2006). Typically, for arc-based radiotherapy sessions, initial patient setup is done once before the start of treatment using kV or MV projection images. Such method does not take into consideration intra-fraction organ motion. With the inherent short treatment time, and high dose conformity of modern arc therapy, unaccounted intra-fractional target motion could offset the benefits of arc therapy and lead to undesired dose distribution. Indeed, intra-fractional organ motion is a major factor hindering the full exploitation of the efficacy of modulated arc therapy for disease sites such as the thorax or upper abdomen. Real-time monitoring of tumor position during the course of arc delivery represents a critical step to alleviate the adverse effect of intrafractional organ motion and ensures adequate doses to target volumes and safe doses to normal tissues. The real-time position information will be used as an input of techniques such as gating, dynamic MLC or auto couch movement.

Stereoscopic imaging systems (Berbeco *et al* 2004, Ozhasoglu and Murphy 2002, Seppenwoolde *et al* 2002, Sharp *et al* 2004, Shirato *et al* 1999), which consist of two kV x-ray tubes mounted to the ceiling and the corresponding amorphous silicon detectors on the opposite side of the patient, have been developed for clinical use in fixed-gantry image guided radiation therapy (IGRT). In this work, we report on our experience in using combined MV treatment beam imaging and onboard kV imaging for real-time tracking of implanted fiducials during an arc therapy delivery. The feasibility of MV–kV beam triangulation for real-time tracking of implanted fiducials for fixed-gantry radiation therapy (Wiersma *et al* 2008) has been demonstrated. This work represents the first attempt of applying the hybrid imaging technique to guide the arc therapeutic delivery. Unlike conventional stereoscopic imaging-based methods (Shirato *et al* 1999), only one kV source is required for full 3D marker geometric information since the actual MV treatment beam is used to provide additional information for 3D positioning. Unlike fixed gantry radiotherapy, there are now several additional challenges to address before MV–kV tracking can be implemented on a rotating gantry. These include

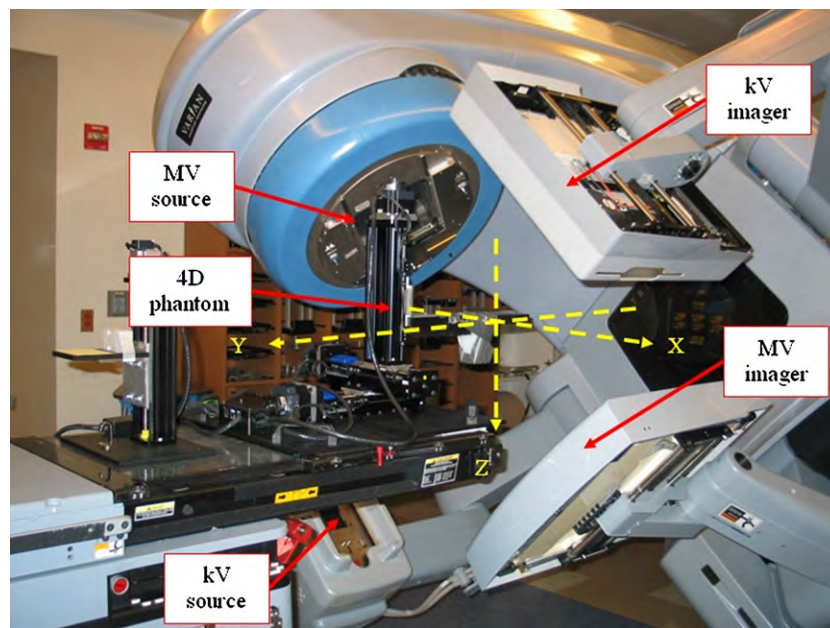


**Figure 1.** Varian Trilogy with kV and MV imagers in extended positions. System frame of reference is denoted by dashed arrows. A 4D motion phantom is located on the couch.

imager tilt, gantry flex and additional detection error caused by the combined motion of the marker and the gantry. As to what extent the gantry rotation affects the detection and monitoring accuracy for two imagers have not been discussed in the literature. For arc therapy guidance, this approach has three distinct advantages over the conventional stereoscopic approach. First, MV–kV tracking reduces the imaging dose since geometric tumor motion in the plane perpendicular to the incidence beam is obtained from the treatment beam without any overhead in radiation dose. Secondly, there is no blockage of the LINAC gantry during the arc delivery. Thirdly, the MV–kV method can be implemented without significant hardware modification for LINACs pre-equipped with both an onboard kV imager and an electronic portal imaging device (EPID). The general reference drawn from this study is that it is feasible to use the hybrid MV and kV imaging to track the 3D position of internally placed metallic markers during dynamic arc radiotherapy with an accuracy better than 1 mm. Factors that may limit the geometrical and temporal precision of MV–kV tracking, such as imager tilt and gantry flex, can be compensated through proper calibration of the system.

## 2. Materials and methods

### 2.1. MV–kV data acquisition

A Trilogy LINAC (Varian Medical Systems, Palo Alto, CA) operating in the 6 MV photon mode was used for the study. Images of the MV beam were acquired by an aSi EPID (PortalVision aS-1000, Varian Medical System, Palo Alto, CA) attached to the LINAC as shown in figure 1. The kV imaging was accomplished using the onboard imaging system located perpendicular to the treatment beam (figure 1). The kV imaging system consisted of a 125 kV x-ray tube together with an aSi flat panel imager (PaxScan 4030CB, Varian Medical

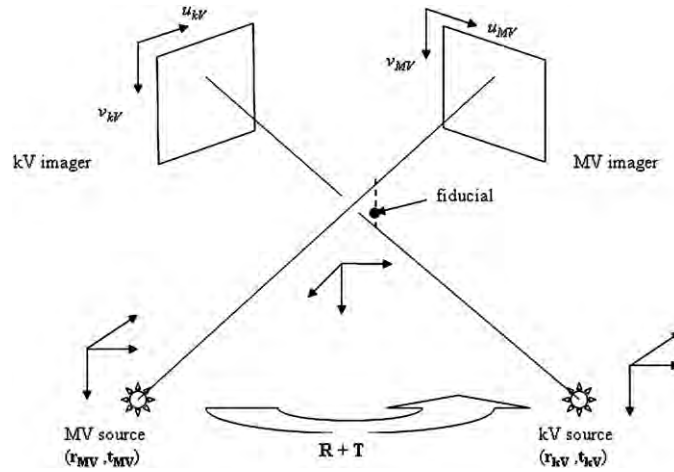


**Figure 2.** Illustration of the hybrid MV and kV imaging system. The rays and fiducial position are shown in the presence of measurement errors.

Systems, Salt Lake City, UT). Pixel sizes of the kV and MV detectors are 0.388 mm and 0.392 mm, respectively. Both detectors had a resolution of  $1024 \times 768$ , corresponding to an effective area of detection of approximately  $40 \text{ cm} \times 30 \text{ cm}$ . Both kV and MV source to imager distances (SID) were set to 150 cm in all experiments. The obtainable maximum MV and kV cine frame rates were  $\sim 8$  and  $\sim 15$  Hz at optimal condition, respectively. The frame rate used in this study is 3.4 Hz for both MV and kV imaging.

## 2.2. Fiducial localization

With measured positions of a fiducial marker on the MV and kV images, it is possible to stereoscopically reconstruct the 3D real-space position of the fiducial, provided that the gantry and imaging system geometry are known. The reconstruction can be done in nearly real time with the cine-mode acquisition of MV and kV images. This section describes our method for obtaining the 3D position of the fiducial from the detected projections of the fiducial in the simultaneously acquired MV and kV images.

**2.2.1. Definition of coordinate systems.** The coordinate systems introduced to describe the fiducial motion are depicted in figures 1 and 2. We will use matrix representation as traditionally used for these types of problems in computer vision. No assumptions are made about the orthogonality of the MV and kV systems since slight deviation of the two imaging systems from the ideal orthogonal situation is possible during rotational delivery. In an ideal situation where the two x-ray beams are orthogonal and the imagers are perfectly aligned, the following formulation can be reduced significantly. However, it is important to emphasize that the kV and MV imaging systems often do not constitute an ideal orthogonal setup because of gantry flex and imager tilt. Thus, a general theoretical framework for 3D reconstruction is needed.

A space fixed coordinate system (referred to as the world coordinate system) with its origin at the system iso-center is used to describe the motion of implanted fiducials. In this system, the  $x$ -,  $y$ - and  $z$ -axes point to the patient's left, inferior and posterior directions, respectively,

when the patient is treated in a supine position without couch rotation. The spatial position of a fiducial is described by

$$\vec{X}_w = (X_w, Y_w, Z_w)^T$$

in the world coordinate system.

For convenience, an imager-fixed coordinate system was defined for both kV and MV imaging systems (figure 2). The pixel coordinate system (a 2D coordinate system fixed to an imager with its origin at the top-left corner) was used to express the location of the fiducial projection in the digital MV or kV image in units of pixel number. The  $u$ - and  $v$ -axes in figure 2 are along the left to right and top to bottom directions. When  $\vec{X}_w$  is projected on the MV and kV imagers, the positions in the MV and kV image planes are denoted by

$$(u_{MV}, v_{MV})^T \quad \text{and} \quad (u_{kV}, v_{kV})^T$$

in the pixel coordinate system (figure 2). These projections are measured variables, and the task is to obtain the position of a fiducial in world coordinates,  $\vec{X}_w$ , from the two projections of the fiducial. For a general camera geometry, this is accomplished by the following 3D reconstruction procedure.

**2.2.2. Stereo triangulation—reconstruction of the world coordinates of an implanted fiducial from its projections on the kV and MV imagers.** The transformations from a set of projections  $(u_{MV}, v_{MV})^T$  and  $(u_{kV}, v_{kV})^T$  to the world coordinate system are determined by two geometric factors: (i) the geometries of the MV and kV imaging systems; (ii) the geometric relation between the MV and kV imaging systems. The first item relates the fiducial projection in units of image pixel to the real distances in units of millimeter (mm) in source-fixed coordinate systems, whereas the second one establishes the correspondence between projections and the world coordinates of the fiducial.

It is mathematically convenient to introduce a 3D radiation-source-fixed coordinate system for both kV and MV imaging systems, as depicted in figure 2. The introduction of the kV and MV source-fixed systems makes it possible for us to deal with the above two factors separately. The source-fixed system has its origin located at the MV or kV source (figure 2). A fiducial in these coordinate systems is described by

$$\vec{X}_{MV} = (X_{MV}, Y_{MV}, Z_{MV})^T \quad \text{and} \quad \vec{X}_{kV} = (X_{kV}, Y_{kV}, Z_{kV})^T.$$

In this system, the  $x$ - and  $y$ -axes are in the same directions as the  $u$ - and  $v$ -, and  $z$ -axes pointed to the iso-center. For convenience, let

$$\vec{U}_{MV} = (su_{MV}, sv_{MV}, s)^T \quad \text{and} \quad \vec{U}_{kV} = (s'u_{kV}, s'v_{kV}, s')^T$$

be homogeneous representations of the pixel coordinates  $(u_{MV}, v_{MV})^T$  and  $(u_{kV}, v_{kV})^T$  in MV and kV imager planes, respectively, where  $s$  and  $s'$  represent the coordinates of the fiducial in the direction perpendicular to the image planes. At this point, both  $s$  and  $s'$  are undetermined scaling factors and can take arbitrary values, which simply saying that the fiducial is along the ray joining the source and projection of the fiducial on the imager plane. It will be shown that  $s$  and  $s'$  will be  $Z_{MV}$  and  $Z_{kV}$ .

The pixel coordinates are related to source-fixed coordinates by calibration matrices  $\mathbf{K}_{MV}$  and  $\mathbf{K}_{kV}$  (Forsyth and Ponce 2003):

$$\vec{U}_{MV} = \mathbf{K}_{MV} \vec{X}_{MV}, \quad \vec{U}_{kV} = \mathbf{K}_{kV} \vec{X}_{kV} \quad (1)$$

$$\mathbf{K} = \begin{bmatrix} f \cdot k_u & 0 & u_0 \\ 0 & f \cdot k_v & v_0 \\ 0 & 0 & 1 \end{bmatrix}, \quad (2)$$

where  $f$  is the source-to-imager distance ( $k_u, k_v$ ) are imager horizontal and vertical pixel lengths and  $(u_0, v_0)$  are the pixel coordinates of the imager center. All the parameters in equation (2) are intrinsic system parameters and can be determined with calibration procedures. The world coordinates are related to the source coordinates by matrices representing a rigid-body motion (Forsyth and Ponce 2003):

$$\vec{X}_{MV} = \mathbf{r}_{MV} \vec{X}_w + \mathbf{t}_{MV}, \quad \vec{X}_{kV} = \mathbf{r}_{kV} \vec{X}_w + \mathbf{t}_{kV} \quad (3)$$

$$\mathbf{r} = \begin{bmatrix} r_{11} & r_{12} & r_{13} \\ r_{21} & r_{22} & r_{23} \\ r_{31} & r_{32} & r_{33} \end{bmatrix}, \quad \mathbf{t} = \begin{bmatrix} t_x \\ t_y \\ t_z \end{bmatrix} \quad (4)$$

where  $(\mathbf{r}, \mathbf{t})$  are the orientation and positions of the radiation sources in the world reference frame. The matrix elements in  $\mathbf{r}$  and  $\mathbf{t}$  depend on the gantry angle and the distance of the radiation source to the origin of world coordinates, and are extrinsic parameters. Note that, using the MV or kV equations in equations (1) and (3), one can project a fiducial in the world coordinates,  $\vec{X}_w$ , onto the MV or kV pixel coordinates. However, the reverse can only be done with information from both MV and kV equations in equations (1) and (3).

To obtain  $\vec{X}_w$  from equations (1) and (3), inversions of one of the two equations in equation (3) are performed. In this calculation, the relation between  $\vec{X}_{MV}$  and  $\vec{X}_{kV}$  is needed. In contrast to our previous work (see Wiersma *et al* (2008)), we do not assume that the MV and kV imagers are perfectly orthogonal. The two vectors  $\vec{X}_{MV}$  and  $\vec{X}_{kV}$  are related by the rigid motion equation:

$$\vec{X}_{kV} = \mathbf{R} \vec{X}_{MV} + \mathbf{T}, \quad (5)$$

where

$$\mathbf{R} = \mathbf{r}_{kV} \mathbf{r}_{MV}^T, \quad \mathbf{T} = \mathbf{t}_{kV} - \mathbf{R} \mathbf{t}_{MV} \quad (6)$$

are the rotation matrix and translation vector characterizing the rigid motion from MV reference frame to kV reference frame. For example, for the orthogonal case, the rotation matrix is simply

$$\mathbf{R} = \begin{pmatrix} 0 & 0 & -1 \\ 0 & 1 & 0 \\ 1 & 0 & 0 \end{pmatrix}.$$

A least-squares optimization is employed to derive the fiducial depth information ( $Z_{MV}$  and  $Z_{kV}$ ), and therefore,  $\vec{X}_w$ , because there are four equations (two from the MV projection and two from the kV projection) and three unknowns (3D world coordinates). This is an over-constrained problem. Because of the presence of noise, the ray from the MV source to the projected fiducial on the MV imager may not intercept with the ray from the kV source to the projected fiducial on the kV imager, as illustrated in figure 2. The least-squares solution allows better utilization of the redundant information compare to the method used in Wiersma *et al* (2008). Mathematically, this least-squares solution of equation (5) can be written as

$$\begin{bmatrix} Z_{MV} \\ Z_{kV} \end{bmatrix} = (\mathbf{A}^T \mathbf{A})^{-1} \mathbf{A}^T \mathbf{T}, \quad (7)$$

where  $\mathbf{A} = [-\mathbf{R} \vec{X}_{MV} / Z_{MV} \quad \vec{X}_{kV} / Z_{kV}]$ . The center of mass of the fiducial marker  $(u_{MV}, v_{MV})^T$  and  $(u_{kV}, v_{kV})^T$  on MV and kV images was converted to  $\vec{X}_{MV} / Z_{MV}$  and  $\vec{X}_{kV} / Z_{kV}$  according to equation (1). Having calculated either  $Z_{MV}$  or  $Z_{kV}$ , the world coordinates of the fiducial were solved with simple manipulation of equation (3), i.e.,

$$\vec{X}_w = \mathbf{r}_{MV}^T (\vec{X}_{MV} - \mathbf{t}_{MV}). \quad (8)$$

The above stereo-reconstruction algorithm applies to two imagers separated by any rotation and translation.

### 2.2.3. Fiducial localization in ideal situation with perfectly aligned MV–kV imaging systems.

To relate the detected pixel location of a fiducial in the projection images to the actual world coordinates, we need to know the intrinsic matrices  $\mathbf{K}_{MV}$  and  $\mathbf{K}_{kV}$  of the MV and kV system (equation (2)), the MV and kV source orientation  $\mathbf{r}_{MV}$  and  $\mathbf{r}_{kV}$  and position  $\mathbf{t}_{MV}$  and  $\mathbf{t}_{kV}$  defined in equation (4). System calibration for the arc therapy involves the determination of these matrices. In an ideal situation where the two beams are orthogonal to each other and the detectors are perfectly aligned, no actual measurement is necessary to obtain the calibration matrices,  $\mathbf{K}_{MV}$ ,  $\mathbf{K}_{kV}$ ,  $\mathbf{r}_{MV}$ ,  $\mathbf{r}_{kV}$ ,  $\mathbf{t}_{MV}$  and  $\mathbf{t}_{kV}$ . For illustration purpose, this special situation is described in this subsection.

Assuming that the center of the image is along the line joining the source and iso-center, the source-to-imager distance is exactly 1500 mm, and both the horizontal and vertical pixel sizes are exactly 0.392 mm for MV and 0.388 mm for kV, the  $\mathbf{K}_{MV}$  and  $\mathbf{K}_{kV}$  can be defined from equation (2). For example, at 90° gantry angle, the matrices  $\mathbf{r}_{MV}$  and  $\mathbf{t}_{MV}$  in equation (3) are given by

$$\mathbf{r} = \begin{bmatrix} \cos(\pi/2) & 0 & -\sin(\pi/2) \\ 0 & 1 & 0 \\ \sin(\pi/2) & 0 & \cos(\pi/2) \end{bmatrix}, \quad \mathbf{t} = \begin{bmatrix} 0 \\ 0 \\ \text{SAD} \end{bmatrix}$$

where SAD is the source-to-axis distance (1000 mm). The matrices  $\mathbf{r}_{kV}$  and  $\mathbf{t}_{kV}$  can be easily obtained because MV and kV beams are perpendicular as assumed above. Then, the 3D fiducial position in real-space can be determined upon the determination of the fiducial on the simultaneous MV and kV images.

In reality, the system parameters in the kV and MV imaging devices may be different from their ideal values and the variations are often gantry angle dependent because of the gantry flex and imager tilt. Thus, a careful system calibration needs to be performed to attain the system calibration matrices. This calibration allows us to maximally compensate for any inaccuracy in the manufacture's setup of the imaging systems and achieve optimal fiducial tracking accuracy. The calibration procedure is described in some details below.

**2.2.4. Fiducial localization with LINAC specific system calibration.** For accurate fiducial tracking, it is required to know the transformation matrices,  $\mathbf{K}_{MV}$ ,  $\mathbf{K}_{kV}$ ,  $\mathbf{r}_{MV}$ ,  $\mathbf{r}_{kV}$ ,  $\mathbf{t}_{MV}$  and  $\mathbf{t}_{kV}$ , for each source-to-imager distance (SID) and gantry angle. For a nominal SID and a nominal gantry angle, a machine-specific calibration following the procedure described below provides a set of calibration matrices. These matrices may be saved in the format of the lookup table.

The system calibration was done through the use of an in-house designed IGRT QA phantom containing 13 stainless steel BBs placed in known locations (Mao *et al* 2008b). After placing the phantom on the LINAC couch, the world coordinates,  $\vec{X}_w = (X_w, Y_w, Z_w)^T$ , of the BBs in the calibration phantom were known with an accuracy of ~0.3 mm in the laboratory frame of reference (Mao *et al* 2008b). At a nominal gantry angle and nominal SID, MV or kV system calibration was done by analyzing the projection image using the camera calibration functions provided in the open source computer vision library (openCV) (openCV 2008). This software used the projection coordinates of the BBs in a MV or kV frame as its input and minimizes the pixel re-projection error in the least-squares sense using a gradient descent method to derive the intrinsic camera parameters and the extrinsic parameters simultaneously. A direct linear transformation (DLT) method (Hartley and Zisserman 2003), which is commonly used for the calibration of a camera system based on a pinhole model, was used to initialize the extrinsic parameters.

After the lookup table is obtained, the following method can be used to perform fiducial tracking during an arc radiotherapy delivery: (i) to detect the fiducial on simultaneous MV

and kV images and its center-of-mass in units of pixel; (ii) to read out the nominal gantry angle and SID and find the corresponding transformation matrices in the lookup table and (iii) to reconstruct the 3D fiducial world coordinates as described in section 2.2.2.

### 2.3. Phantom validation

The tracking accuracy of the proposed method was first evaluated using a static fiducial. In this experiment, a semi-circular (90–270°) arc plan at 300 MU/min dose rates was delivered to a plastic phantom with an embedded ball bearing (BB) of 3 mm diameter. For simplicity, the field size was fixed at 10 cm × 10 cm at all angles. Three measurements with the fiducial placed at different positions were carried out. The tracking results were compared with the known coordinates of the fiducial. This measurement yields the best achievable tracking accuracy of the system because there is no complication caused by any fiducial motion.

In the next series of tests, a 4D motion platform (Washington University, St Louis, MO) (Malinowski *et al* 2007) capable of moving in accordance with a pre-programmed trajectory was used to move stainless steel BB enclosed in a plastic phantom. Accurate validation tests (Malinowski *et al* 2007) on the 4D platform showed a mean positional error of less than 0.2 mm from the inputted trajectory. Periodic motion patterns with two different amplitudes and three different periods were used to program the motion of the testing phantom. Specifically, the ranges of the two motions were set to be {10 mm (LR), 25 mm (SI) and 10 mm (AP)}, and {4 mm (LR), 12 mm (SI), and 8 mm (AP)}, respectively. For each motion range, a period of 3, 4 and 5 s was applied. The motion ranges and periods chosen here reflect some typical and extreme cases observed in actual lung tumor cases in clinical practice (Keall *et al* 2006, Maxim *et al* 2007).

Currently, clinical mode of the LINAC does not support turning on both the MV and kV imagers simultaneously. Therefore, all experiments were performed in maintenance mode. Two methods were used for acquiring MV and kV image data. The first method used two channels of a four-channel PCI video frame grabber card (ProVideo 149P, ProVideo Co., Taipei, Taiwan) to grab both the MV and kV video streams simultaneously at 30 fps on a dedicated imaging processing computer. In this case both capture and processing were done at near real-time speeds with an estimated system delay of ~150–200 ms (Wiersma *et al* 2008). This method supports synchronization of MV and kV images to the single fixed CPU clock of the image processing computer, allowing the corresponding MV–kV pairs to be determined for a particular time with relative ease. However, an associated drawback of this method was a reduction of the MV and kV image resolutions from their native 1024 × 768 aSi flat panel resolutions to the maximum 640 × 480 resolution of the video capture card. The second method recorded both MV and kV images in real time to their separate MV and kV imaging computers. This method allowed capture at their native 1024 × 768 imager resolutions. In this case, post-analysis was then performed to synchronize the two video streams by aligning image motion features along their *v*-axes.

## 3. Results

### 3.1. Accuracy of kV and MV imaging at different gantry angles during an arc delivery

Following the calibration procedure described in section 2.2.4, figure 3 shows the root mean square (RMS) errors between the detected and ground truth projected positions of the BBs as a function of gantry angle during arc delivery for the MV (+) and kV (\*) systems. The data at each gantry angle were obtained using the IGRT QA phantom with 13 embedded BBs. Each

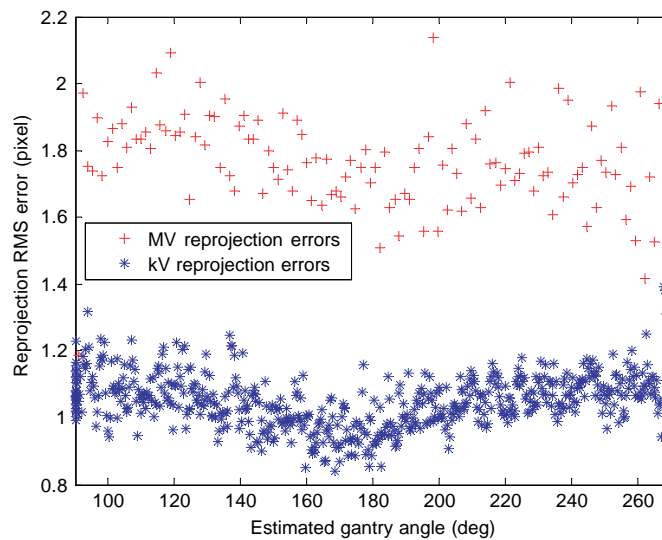


**Figure 3.** MV and kV re-projection RMS errors during system calibration.

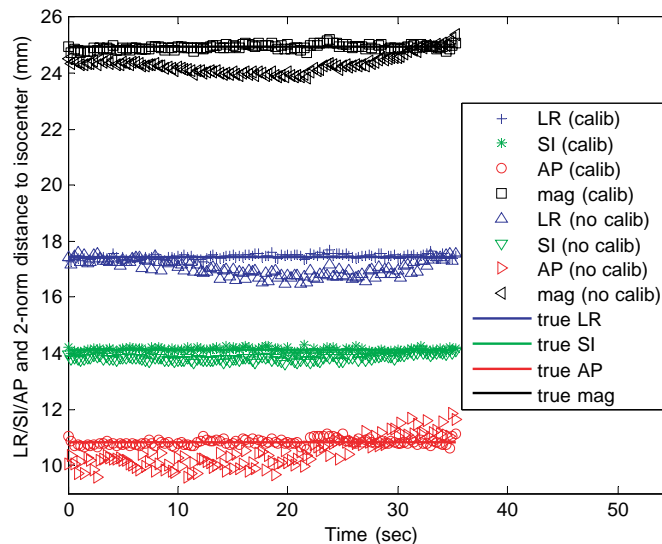


**Figure 4.** Real-time tracking of a static BB marker during arc delivery using the hybrid MV–kV method. The cross, star, circle and square symbols are the measured results with system calibration. The triangles are the results obtained in the absence of system calibration. The actual BB position coordinates are also plotted for comparison.

point represents the RMS error of the 13 BBs in the phantom. The RMS re-projection errors are  $\sim 1.7$  pixel for the MV imager and  $\sim 1.0$  pixel for the kV imager.

### 3.2. Fiducial tracking during arc therapy delivery

**3.2.1. Detection of a static fiducial.** Figure 4 shows real-time 3D tracking of a static marker during an arc delivery with the gantry rotating from  $90^\circ$  to  $270^\circ$  with and without system

**Table 1.** Summary of tracking accuracy with calibration. The frame rate of MV imaging was 3.4 Hz

	RMS error (LR) mm	RMS error (SI) mm	RMS error (AP) mm	RMS error (mag) mm	Max error (mag) mm
Static fiducial	0.08	0.07	0.11	0.16	0.35
Extreme pattern <sup>a</sup>	0.57	1.29	0.57	1.52	2.88
$T = 3$ s					
Extreme pattern <sup>a</sup>	0.43	0.75	0.40	0.95	2.30
$T = 4$ s					
Extreme pattern <sup>a</sup>	0.30	0.49	0.28	0.64	1.90
$T = 5$ s					
Normal pattern <sup>b</sup>	0.21	0.36	0.30	0.52	1.05
$T = 4$ s					

<sup>a</sup> Motion displacement range is {10 mm (LR), 25 mm (SI), 10 mm (AP)}.<sup>b</sup> Motion displacement range is {4 mm (LR), 12 mm (SI), 8 mm (AP)}.

calibration. In the absence of calibration (i.e. assuming the MV–kV imaging systems were perfectly aligned as described in section 2.2.3), the maximum fiducial tracking error was found to be 1.29 mm. With the use of system calibration, this was reduced to 0.35 mm. Specific to each direction, the maximum tracking error was 0.96, 0.50 and 1.25 mm in the LR, SI and AP directions, respectively, when no system calibration was applied. These were reduced to 0.23, 0.17 and 0.31 mm, respectively, when the calibration was applied. The tracking error varies from gantry angle to gantry angle and the error is negligible in the SI direction because the uncertainty of the system parameters in that direction is small during an arc delivery. The experiments were repeated by placing the fiducial at three different positions and similar results were found.

**3.2.2. Tracking of a moving fiducial.** Figure 5 shows the measurements of the pre-programmed motion of a fiducial as a function of time or gantry rotation angle (see section 2.3). For a ‘normal breathing’ pattern (i.e. the range of motion was {4 mm (LR), 12 mm (SI), 8 mm (AP)} corresponding to the mean thoracic tumor displacements reported in the literature (Keall *et al* 2006, Maxim *et al* 2007)) with a period of 4 s (figure 5(a)), the RMS and maximum tracking errors were found to be 0.52 mm and 1.05 mm, respectively, with calibration (table 1). The RMS errors in the three directions were {0.21 mm (LR), 0.36 mm (SI), 0.30 mm (AP)}. These results indicate that with the currently available MV–kV imaging technology, tracking a moving fiducial with an accuracy better than 1 mm during an arc therapy delivery is well achievable.

To test the limit of the hybrid kV and MV tracking, some more extreme cases were investigated. The tracking accuracy is influenced by the motion amplitude and ‘breathing’ period as they change the maximum speed of the fiducial. In figure 5(b), the range of motion was set to be {10 mm (LR), 25 mm (SI), 10 mm (AP)}, and the programmed motion period was 3 s. This setting has a maximum speed of approximately  $2.6 \text{ cm s}^{-1}$  and is close to be the ‘worst case’ seen in clinic for lung tumor motions (Keall *et al* 2006). Even for this unusual case, the tracked motion was found to be very close to the actually inputted motion. In the absence of calibration, the maximum fiducial tracking error was found to be 3.65 mm. With the use of system calibration, this was reduced to 2.88 mm. Specific to each direction, the maximum fiducial tracking errors were {1.63 mm (LR), 3.25 mm (SI), 2.06 mm (AP)} and {1.19 mm (LR), 2.68 mm (SI), 1.43 mm (AP)} without and with system calibration applied, respectively. As discussed in the next section, the fairly large maximum error observed here

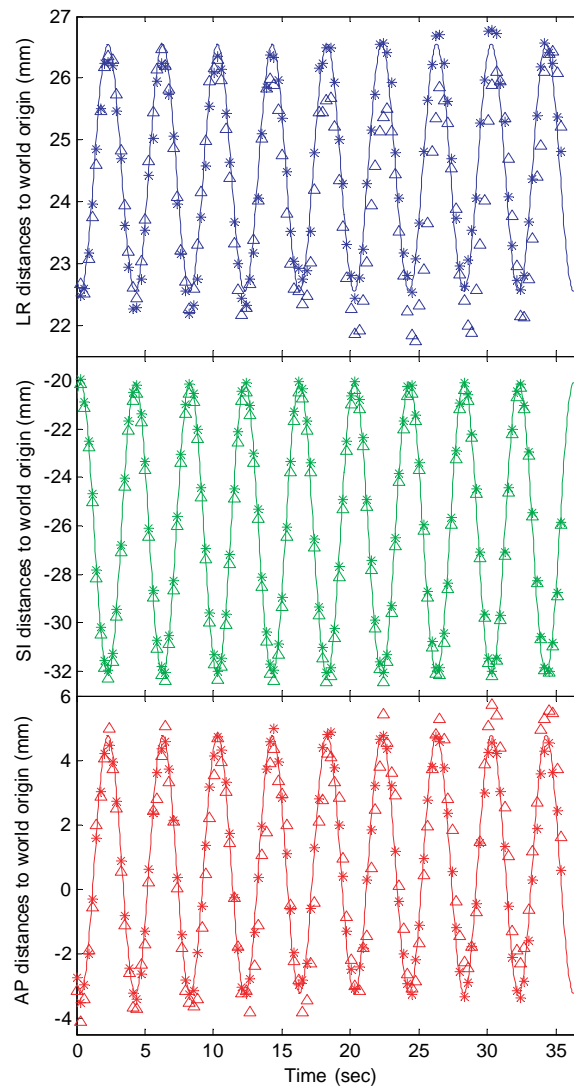


**Figure 5.** (a) MV–kV tracking of a moving fiducial during arc therapy. The range of motion was {4 mm (LR), 12 mm (SI), 8 mm (AP)} and the motion period was 4 s. Measured 3D fiducial positions obtained with calibration (\*) and using the system readouts without calibration ( $\Delta$ ) are shown. Deviation between programmed and experimental data points expressed as RMS error (table 1). Solid curve is the programmed 4D phantom motion. The gantry angle was from  $90^\circ$  to  $270^\circ$ . (b): MV–kV tracking of a moving fiducial during arc therapy. The range of motion was {10 mm (LR), 25 mm (SI), 10 mm (AP)} and the motion period was 3 s. Measured 3D fiducial positions obtained with calibration (\*) and using the system readouts without calibration ( $\Delta$ ) are shown. Deviation between programmed and experimental data points expressed as RMS error (table 1). Solid curve is the programmed 4D phantom motion. The gantry angle was from  $90^\circ$  to  $270^\circ$ .

is attributed to the slow frame rate of the MV imaging system for the dose rate used in our experiments.

The tracking accuracy was greatly improved when the motion period becomes more ‘normal’. By setting the ‘breathing’ period to 4 s while maintaining for the same large motion

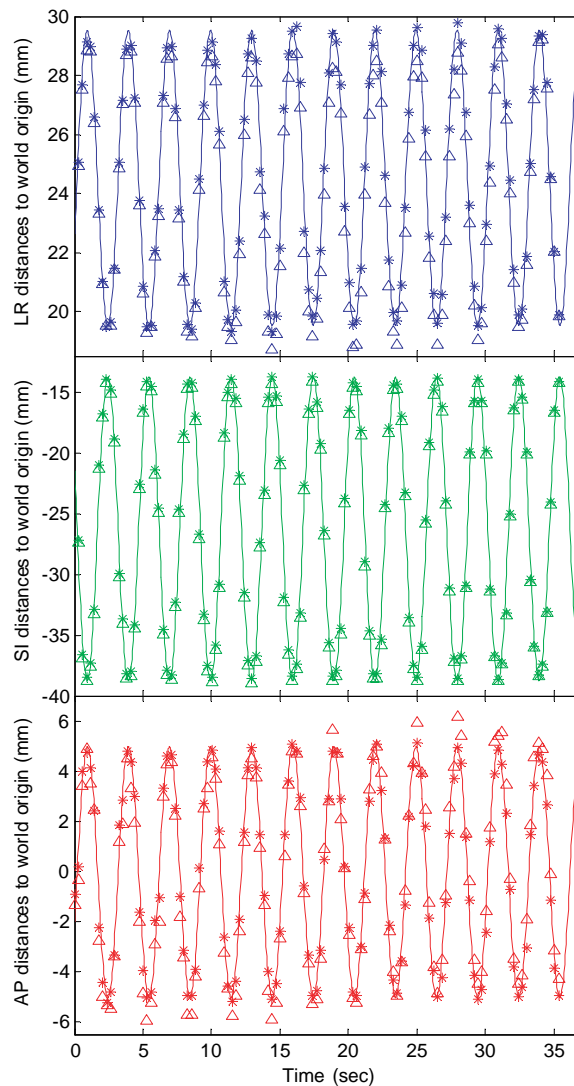
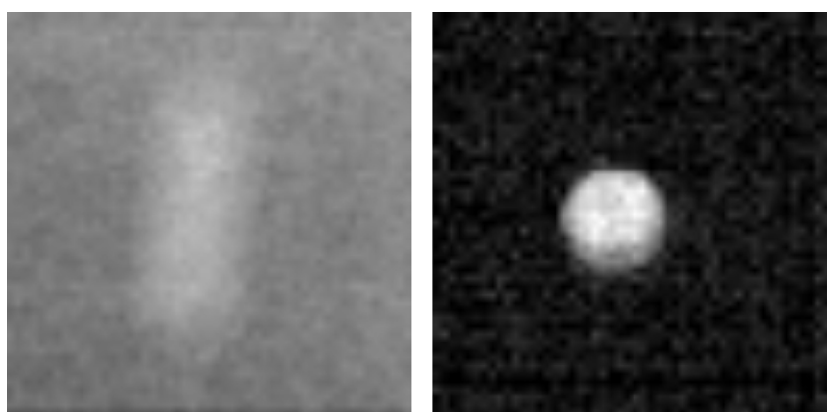


Figure 5. (Continued.)

amplitude, it was found that the RMS and maximum errors were reduced to 0.95 mm and 2.30 mm, respectively. The RMS errors in the LR, SI and AP directions were {0.43 mm, 0.75 mm, 0.40 mm} (see table 1). By proper breath coaching, 4 s period is usually achievable for the majority of patients. At this period, the RMS tracking error was within 1 mm even for large motion amplitude.

#### 4. Discussion

A critical step in dealing with intrafraction tumor motion is the real-time monitoring of the tumor position. Despite intense research effort in attempting to utilize the inherent image features to extract real-time information of tumor motion, at this point, fiducial implantation



**Figure 6.** An example of the detected marker on MV (left) and kV (right) images. The image size is 2 cm by 2 cm. The MV frame rate was 3.4 Hz, whereas the kV frame rate was 15 Hz.

remains the most reliable way to accomplish the stated goal. In this work we have presented an effective method of using a combined MV–kV fiducial tracking system during an arc therapy delivery process. Replacing the fiducial detection step with an advanced feature detection technique, the strategy may also be applied to tissue-feature-based tracking in the future.

Both intrinsic and extrinsic parameters of the kV and MV imaging systems need to be calculated at each nominal gantry angle and SID because mechanical flex can change the relative position between the imagers and sources during an arc therapy delivery. The conversion from the pixel coordinates to lab coordinates includes both intrinsic imaging system parameters and extrinsic parameters. Therefore, it is the combined transformation matrix that determines the accuracy of 3D reconstruction. After calibration, the averaged re-projection errors of the BBs in the QA phantom are around 1 pixel (see figure 3), which amounts to  $\sim 0.3$  mm on the iso-center plane. The errors arise mainly from two sources: inherent inaccuracy of the BB positions in the calibration phantom and the finite detection accuracy of the spatial locations of the BBs on the projection images. Due to the imperfection of MV–kV imager dark and flood field calibration and motion blur, the resulting MV or kV projection of a BB may not be radial symmetric. In addition, perspective projection is generally not a shape preserving transformation. Depending on the location of the BB relative to the center axis of the beam, the distortion caused by the perspective projection may result in the projected BB center not being at the same position as the center of mass of the projected shape although the error is quite small ( $\sim 0.2$  pixel) (Heikkila and Silven 1997). Considering all the described error sources and that there are only 13 BBs in our calibration phantom, the accuracy of the calibration is quite reasonable. By using a precisely fabricated phantom with sufficient number of fiducials (for example 5–10 times greater than the number of unknowns needs to be solved), it is anticipated that the re-projection error will be significantly reduced. This should lead to better tracking accuracy.

The slow MV imaging frame rate in currently available LINACs is a factor limiting the fiducial tracking accuracy in cases where the fiducial motion is much faster than an ordinary clinical situation. When the marker speed increases, the captured marker image becomes blurred and elongated in the MV image due to its low (3.4 Hz) capture rate. In figure 6, the image captured by the MV imager (3.4 Hz) and the kV imager (15 Hz) for a marker speed of  $2.6 \text{ cm s}^{-1}$ , which is similar to the motion blurring observed in other imaging systems (Li *et al*

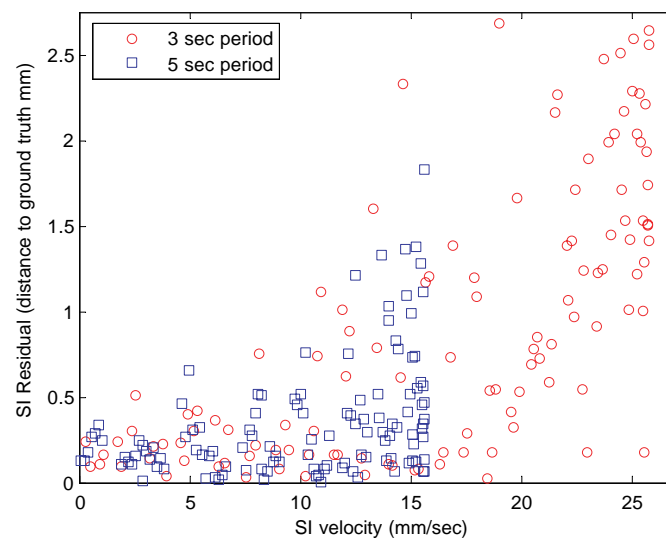


**Figure 7.** Absolute residual tracking error (the absolute value of the difference between the measured and the known positions of the fiducial) in the SI direction as a function of the fiducial velocity. The EPID image capture frame rate was 3.4 Hz. The maximum residual error increases with the motion speed.

2006, Thorndyke *et al* 2006, 2008). A slower frame rate of MV acquisition is primarily due to the limited efficiency of the flat panel detector at the MV energy range and the dose rate used. However, this issue should be resolvable as more advanced digital imaging technology is integrated into the onboard imaging system. In general, it was found that the tracking error increases with the marker velocity. Figure 7 shows the absolute residual tracking errors (the absolute value of the difference between the measured and the known positions of the fiducial) in SI direction (motion range was 25 mm—a more extreme case) for two different motion periods (3 and 5 s) when the EPID was operated at a frame rate of 3.4 Hz. The results clearly show that the residual error depends on the fiducial speed (not the motion period). The error was found to be negligible when the motion speed was less than  $10 \text{ mm s}^{-1}$ . Overall, the tracking accuracy is acceptable for a breathing period of 5 s, even though the motion range is much larger than ‘normal’. In this case, the maximum error was found to be 1.8 mm at the point with the maximum speed. For this breathing pattern, the mean and RMS errors for the points with motion speed greater than  $1.5 \text{ cm s}^{-1}$  were found to be 0.49 mm and 0.74 mm, respectively. However, for the breathing period of 3 s, the residual error is markedly increased at the points where the fiducial motion reaches its maximum speed. As seen from figure 7, the maximum error in this case is close to 3 mm. The mean and RMS errors for the points with motion speed greater than  $2.3 \text{ cm s}^{-1}$  were found to be 1.75 mm and 1.92 mm, respectively. The trends of residual errors in the LR and AP directions as a function of the fiducial velocity were observed to be similar to that in SI direction as described above. In general, an image acquired at a faster capture rate is similar to that acquired at a slower motion. According to the data presented in table 1, for the 3 s period motion with a larger amplitude, by increasing the frame rate from 3.4 Hz to 4.5 Hz, the RMS error can be controlled to below 1 mm. Dose rate of the investigated treatment plan was set to be  $300 \text{ MU min}^{-1}$  (according to the control panel display, the actual dose rate was about  $160 \text{ MU min}^{-1}$  during the arc delivery because the gantry cannot rotate faster than 1 min per rotation).

The proposed hybrid MV–kV imaging technique is readily applicable to facilitate conventional 3D arc therapy by providing real-time information of the implanted fiducials. When using an intensity modulated MV beam for in-line imaging, a potential difficulty is that the fiducials may be partially or completely blocked by the MLC leaves at certain angle(s). There are several sources of information that can help to estimate the 3D coordinates of the MLC-blocked fiducial in this situation. First, the coordinates of the fiducial in the plane perpendicular to the kV beam are still available from kV imaging, regardless whether the fiducial is blocked or not by the MLC. This piece of information is very valuable because it significantly reduces the dimensionality of the problem. It can be used together with a suitable motion prediction/correlation model to predict the missing dimension (since two marker dimensions are provided by the kV imager). Secondly, the fiducial kinetics attained by the MV–kV system at an earlier time when the marker(s) are not blocked can be utilized to adaptively predict the ‘missing’ coordinate of the marker in combination with the kV information. Thirdly, the MLC leaf positions are always available from the EPID images, which can serve as a useful landmark for fiducial position estimation. Finally, the 3D movement of the markers captured by the pre-treatment CBCT and planning CT is also available as a priori knowledge for better positional estimation. The development of such a multiple input single output (MISO) adaptive prediction algorithm is still in progress. Since only one coordinate needs to be estimated for a short interval of time, we foresee no major difficulty in accomplishing an accurate positional estimation. This remains true in a rare situation when all the fiducials are blocked by a MLC segment. For certain types of tumors that deform little during the treatment process (e.g. the prostate), the positions of unblocked fiducials can be employed as landmarks in allocating the MLC-blocked fiducial(s) (Mao *et al* 2008a). Note that, in reality, it is possible to take the fiducial information into consideration during the modulated arc therapy inverse planning process. This should be feasible to ensure the visibility of at least one fiducial during inverse planning. Of course, the addition of this type of constraint in inverse planning may compromise the achievable dose distribution. But it is arguable that the tradeoff will likely be minimal because, after all, for the majority of cases, the fiducials are placed inside the tumor target volume and represent high dose points. We are currently actively pursuing the study and the results will be reported elsewhere.

In practice, the kV imager does not have to be on throughout the whole arc delivery process. The usage of kV imaging may be potentially reduced by use of information provided by the MV imaging and a knowledge-based motion prediction algorithm. Our preliminary results have shown that the kV frame rate can be reduced to 1 Hz, while maintaining accurate 3D tumor tracking using an autoregressive and moving average model (Box *et al* 1994). We are also investigating the feasibility of 3D fiducial tracking using only the MV beam for arc based deliveries since the intrinsic motion of the gantry during these types of deliveries offers a natural way to take multiple images from different viewing angles. Here, it is anticipated that temporally fast, while still spatially accurate, 3D reconstruction may be challenging due to relatively small gantry angle difference between captured MV image frames of short time separation. For slow moving organs such as the prostate, tracking using MV images with larger angle separation is potentially possible, whereas, for fast targets as lung-based tumors, it may be possible to complement the MV imaging with occasional kV imaging.

Although internal marker positional information from the treatment beam (MV EPID images) can be acquired with no additional dose cost to the patient, real-time kV monitoring of tumor motion will introduce extra diagnostic dose to the patient. Wen *et al* (2007) have reported that skin doses for a Varian CBCT scan (with 660 images) is 3–6 cGy (less than 0.01 cGy/projection). For real-time marker motion tracking, as discussed above, the necessary frame rate can be reduced to an order lower or less. Therefore, for a typical 40-fraction

treatment, the total extra skin dose caused by kV imaging will be around 20 cGy or less, which is not considered significant for radiation therapy. It is envisioned that future advances in imaging hardware and software, together with the relative ease of detecting metallic fiducials in kV images, will lead to reduction in the necessary tracking dose. For example, recent advances in imaging algorithms based on x-ray image noise properties can further reduce the kV imaging dose without significantly sacrificing image quality (Wang *et al* 2008).

## 5. Conclusion

Through the use of combined MV and kV cine imaging, we have demonstrated a method of tracking the real-time location of internal fiducial markers during arc delivery with an accuracy better than 1 mm for typical adult breathing patterns. Unlike other fluoroscopy based tracking techniques, which require two or more kV sources, only one kV source is needed. The technique can be readily implemented on any LINACs equipped with onboard kV and EPID imaging devices. Furthermore, the problem of gantry blockage commonly seen in other stereostatic imaging systems is effectively alleviated in the proposed approach. Given the increased popularity of arc delivery and the general need of knowing the target position during a treatment fraction, the proposed technique is very promising for future use in the clinic.

## Acknowledgments

The authors wish to thank Dr Edwards Mok and Dr David Findley for their help on the experiments and Paul Keall's group for their help on 4D photon data acquisition. This project was supported in part by grants from National Cancer Institute (1R01CA98523 and CA104205), the Komen Breast Cancer Foundation (BCTR0504071) and the Department of Defense Prostate Cancer Research Program (PC073690).

## References

- Berbeco R I, Jiang S B, Sharp G C, Chen G T, Mostafavi H and Shirato H 2004 Integrated radiotherapy imaging system (IRIS): design considerations of tumour tracking with linac gantry-mounted diagnostic x-ray systems with flat-panel detectors *Phys. Med. Biol.* **49** 243–55
- Box G E P, Jenkins G M and Reinsel G C 1994 *Time Series Analysis: Forecasting and Control* (Englewood Cliffs, NJ: Prentice-Hall)
- Cameron C 2005 Sweeping-window arc therapy: an implementation of rotational IMRT with automatic beam-weight calculation *Phys. Med. Biol.* **50** 4317–36
- Crooks S M, Wu X D, Takita C, Watzich M and Xing L 2003 Aperture modulated arc therapy *Phys. Med. Biol.* **48** 1333–44
- Forsyth D and Ponce J 2003 *Computer Vision: A Modern Approach* (Englewood Cliffs, NJ: Prentice-Hall)
- Hartley R and Zisserman A 2003 *Multiple View Geometry in Computer Vision* (Cambridge, UK: Cambridge University Press)
- Heikkila J and Silven O 1997 Four-step camera calibration procedure with implicit image correction *IEEE Computer Society Conf. on Computer Vision and Pattern Recognition (San Juan, PR, USA)* (Los Alamitos, CA: IEEE) pp 1106–12
- Keall P J *et al* 2006 The management of respiratory motion in radiation oncology report of AAPM Task Group 76 *Med. Phys.* **33** 3874–900
- Li T, Schreiber E, Yang Y and Xing L 2006 Motion correction for improved target localization with on-board cone-beam computed tomography *Phys. Med. Biol.* **51** 253–67
- Malinowski K, Noel C, Lu W, Lechleiter K, Hubenschmidt J, Low D and Parikh P 2007 Development of the 4D Phantom for patient-specific, end-to-end radiation therapy QA *SPIE 6510— Medical Imaging, Physics of Medical Imaging, 65100E* ed J Hsieh and M J Flynn (San Diego, CA; SPIE International Society) p 65100E

- Mao W, Wiersma R D and Xing L 2008a Fast internal marker tracking algorithm for onboard MV and kV imaging systems *Med. Phys.* **35** 1942–9
- Mao W H, Lee L and Xing L 2008b Development of a QA phantom and automated analysis tool for geometric quality assurance of on-board MV and kV x-ray imaging systems *Med. Phys.* **35** 1497–506
- Maxim P G, Loo B W, Shirazi H, Thorndyke B, Luxton G and Le Q T 2007 Quantification of motion of different thoracic locations using four-dimensional computed tomography: implications for radiotherapy planning *Int. J. Radiat. Oncol. Biol. Phys.* **69** 1395–401
- openCV 2008 <http://opencvlibrary.sourceforge.net/>
- Otto K 2008 Volumetric modulated arc therapy: IMRT in a single gantry arc *Med. Phys.* **35** 310–7
- Ozhasoglu C and Murphy M J 2002 Issues in respiratory motion compensation during external-beam radiotherapy *Int. J. Radiat. Oncol. Biol. Phys.* **52** 1389–99
- Palma D, Vollans E, James K, Nakano S, Moiseenko V, Shaffer R, McKenzie M, Morris J and Otto K 2008 Volumetric modulated arc therapy for delivery of prostate radiotherapy: comparison with intensity-modulated radiotherapy and three-dimensional conformal radiotherapy *Int. J. Radiat. Oncol. Biol. Phys.* **72** 996–1001
- Ramsey C R, Spencer K M, Alhakeem R and Oliver A L 2001 Leaf position error during conformal dynamic arc and intensity modulated arc treatments *Med. Phys.* **28** 67–72
- rapidArc 2008 [http://www.varian.com/us/oncology/treatments/treatment\\_techniques/rapidarc/](http://www.varian.com/us/oncology/treatments/treatment_techniques/rapidarc/)
- Seppenwoolde Y, Shirato H, Kitamura K, Shimizu S, van Herk M, Lebesque J V and Miyasaka K 2002 Precise and real-time measurement of 3D tumor motion in lung due to breathing and heartbeat, measured during radiotherapy *Int. J. Radiat. Oncol. Biol. Phys.* **53** 822–34
- Sharp G C, Jiang S B, Shimizu S and Shirato H 2004 Tracking errors in a prototype real-time tumour tracking system *Phys. Med. Biol.* **49** 5347–56
- Shirato H, Shimizu S, Shimizu T, Nishioka T and Miyasaka K 1999 Real-time tumour-tracking radiotherapy *Lancet* **353** 1331–2
- Thorndyke B, Koong A and Xing L 2008 Reducing respiratory motion artifacts in radionuclide imaging through retrospective stacking: a simulation study *Linear Algebr. Appl.* **428** 1325–44
- Thorndyke B, Schreiber E, Koong A and Xing L 2006 Reducing respiratory motion artifacts in positron emission tomography through retrospective stacking *Med. Phys.* **33** 2632–41
- Verellen D, Linthout N and Storme G 1998 Target localization and treatment verification for intensity modulated conformal radiation therapy of the head and neck region—the AZ-VUB experience *Strahlentherapie Onkologie* **174** 19–27
- Verellen D, Linthout N, VandenBerge D, Bel A and Storme G 1997 Initial experience with intensity-modulated conformal radiation therapy for treatment of the head and neck region *Int. J. Radiat. Oncol. Biol. Phys.* **39** 99–114
- VMAT 2008 [http://www.elekta.com/healthcare\\_international\\_elekta\\_vmat.php](http://www.elekta.com/healthcare_international_elekta_vmat.php)
- Wang J, Zhu L and Xing L 2008 Noise reduction in low-dose X-ray fluoroscopy for image guided radiation therapy *Int. J. Radiat. Oncol. Biol. Phys.* at press
- Wen N, Guan H Q, Hammoud R, Pradhan D, Nurusev T, Li S D and Movsas B 2007 Dose delivered from Varian's CBCT to patients receiving IMRT for prostate cancer *Phys. Med. Biol.* **52** 2267–76
- Wiersma R D, Mao W H and Xing L 2008 Combined kV and MV imaging for real-time tracking of implanted fiducial markers *Med. Phys.* **35** 1191–8
- Wong E, Chen J Z and Greenland J 2002 Intensity-modulated arc therapy simplified *Int. J. Radiat. Oncol. Biol. Phys.* **53** 222–35
- Xing L, Thorndyke B, Schreiber E, Yang Y, Li T F, Kim G Y, Luxton G and Koong A 2006 Overview of image-guided radiation therapy *Med. Dosim.* **31** 91–112
- Yu C X 1995 Intensity-modulated arc therapy with dynamic multileaf collimation—an alternative to tomotherapy *Phys. Med. Biol.* **40** 1435–49

# A fiducial detection algorithm for real-time image guided IMRT based on simultaneous MV and kV imaging

Weihua Mao, Nadeem Riaz, Louis Lee, Rodney Wiersma, and Lei Xing<sup>a)</sup>

*Department of Radiation Oncology, Stanford University School of Medicine, Stanford, California 94305-5847*

(Received 9 January 2008; revised 2 May 2008; accepted for publication 11 June 2008; published 11 July 2008)

The advantage of highly conformal dose techniques such as 3DCRT and IMRT is limited by intrafraction organ motion. A new approach to gain near real-time 3D positions of internally implanted fiducial markers is to analyze simultaneous onboard kV beam and treatment MV beam images (from fluoroscopic or electronic portal image devices). Before we can use this real-time image guidance for clinical 3DCRT and IMRT treatments, four outstanding issues need to be addressed. (1) How will fiducial motion blur the image and hinder tracking fiducials? kV and MV images are acquired while the tumor is moving at various speeds. We find that a fiducial can be successfully detected at a maximum linear speed of 1.6 cm/s. (2) How does MV beam scattering affect kV imaging? We investigate this by varying MV field size and kV source to imager distance, and find that common treatment MV beams do not hinder fiducial detection in simultaneous kV images. (3) How can one detect fiducials on images from 3DCRT and IMRT treatment beams when the MV fields are modified by a multileaf collimator (MLC)? The presented analysis is capable of segmenting a MV field from the blocking MLC and detecting visible fiducials. This enables the calculation of nearly real-time 3D positions of markers during a real treatment. (4) Is the analysis fast enough to track fiducials in nearly real time? Multiple methods are adopted to predict marker positions and reduce search regions. The average detection time per frame for three markers in a  $1024 \times 768$  image was reduced to 0.1 s or less. Solving these four issues paves the way to tracking moving fiducial markers throughout a 3DCRT or IMRT treatment. Altogether, these four studies demonstrate that our algorithm can track fiducials in real time, on degraded kV images (MV scatter), in rapidly moving tumors (fiducial blurring), and even provide useful information in the case when some fiducials are blocked from view by the MLC. This technique can provide a gating signal or be used for intra-fractional tumor tracking on a Linac equipped with a kV imaging system. Any motion exceeding a preset threshold can warn the therapist to suspend a treatment session and reposition the patient. © 2008 American Association of Physicists in Medicine. [DOI: 10.1118/1.2953563]

## I. INTRODUCTION

Highly conformal radiation therapy techniques, such as three-dimensional conformal radiotherapy (3DCRT) and intensity-modulated radiation therapy<sup>1</sup> (IMRT), provide exquisitely shaped radiation doses that closely conform to tumor dimensions while sparing sensitive structures.<sup>1,2</sup> They require greater precision in tumor localization, treatment setup, and delivery than conventional techniques. In practice, inter- and intrafraction organ motion results in an uncertainty of tumor location. For example, respiratory and prostate tumors can move up to 3 cm over the course of routine radiotherapy.<sup>3–9</sup> Research activities on image-guided radiation therapy have emerged recently to improve targeting in radiation treatment.<sup>10</sup> It is essential to track the dynamical nature of human anatomy or at least the tumor motion in real time.<sup>11</sup>

Several methods of obtaining the real-time tumor position are available, and these can be categorized as being either indirect (external surrogate based) or direct (fiducial/image) in nature. In general, indirect tumor location methods, such as external skin marker tracking or breath monitoring techniques, rely on the correlation between external body param-

eters and the tumor.<sup>5,12</sup> In reality, the relationship between external parameters and internal organ motion is complex and a large uncertainty may be present in predicting the tumor location based on external markers. Direct tumor position measurement is highly desirable for therapeutic guidance. In the last decade, a number of direct real-time 3D tumor tracking methods have been implemented, primarily using fluoroscopy<sup>5,11,13</sup> or magnetic field localization.<sup>14</sup> Particularly, the feasibility of using electronic portal imaging devices (EPID) and stereoscopic x-ray imaging for real-time tumor tracking has been explored.<sup>3,5,6,15–26</sup>

A crucial component of an image based tracking system is the ability to successfully identify and track user-specified image-based features at a near real-time speed. The detection algorithm must also be able to segment markers from anatomic structures and simultaneously track multiple markers without confusing one marker for another. Generally, an intensity based fiducial marker detection algorithm tends to fail when the marker is in the vicinity of high contrast structures such as bone. This can be avoided by using template matching, as demonstrated by Shirato *et al.*, for the tracking of a single spherical gold marker using multiple kV fluoroscopic

imaging systems.<sup>25</sup> Tang *et al.* have further extended template matching by developing a cylindrical marker detection algorithm that takes into account the different possible projections of the marker based on its orientation and length on their custom designed stereoscopic kV on-board imaging systems.<sup>27</sup> Because a single in-line x-ray beam is only two dimensional, the 3D coordinates of the embedded fiducials are usually obtained by specially designed multiple kV x-ray sets.<sup>3,5,6,25–28</sup>

Recently, Wiersma *et al.* used combined kV and MV imaging systems to track the 3D location of a spherical metallic fiducial.<sup>29</sup> This technique has the inherent benefit in that only one kV source is required for full 3D marker positional information since the actual MV beam is also used for positioning. Compared to other stereoscopic systems, which generally require two or more kV imaging sets, this technique reduces the radiation dose to the patient and requires minimal modification of the current hardware. In Wiersma's work, a freely available third party software program was used to detect a spherical fiducial, 3 mm in diameter. As of yet, there have been few works presenting marker-tracking algorithms that are suitable for tracking internal markers using MV image data with high success rates because these images have significantly reduced contrast.<sup>18</sup> Further, it is a more challenging task to robustly detect small cylindrical fiducials (gold seeds) used clinically, in a realistic setting. This problem is exacerbated when the incident beam is an IMRT field instead of an open field, because one or all implanted fiducials may be blocked by the MLC at some segments during IMRT delivery.

In this article, using a new detection algorithm,<sup>30</sup> we will study four clinically relevant issues pertaining to the application of tracking fiducials in real time based on simultaneous kV and MV imaging:

- (1) How fast can a marker move and still be detectable? Motion will blur the fiducial and hinder tracking it. It is essential to investigate the maximum moving speed at which the markers can still be detected by this procedure.
- (2) How does the MV beam scattering affect kV imaging? It has been reported that if MV and kV images are acquired simultaneously, MV beam scattering has significant interference with kV imaging while kV beam scattering effect on MV images is minor.<sup>31</sup> A quantitative study is necessary to clarify if simultaneous MV beam scattering affects the detection of markers on kV images.
- (3) Can an algorithm reliably track markers in MV images with irregular fields? The aperture of MV beam is carefully modified by a multiple-leaf collimator (MLC) in any 3DCRT or IMRT treatment plans. A major challenge is that one or more markers may be outside of the MV fields/ images and this requires very high specificity detection, particularly when the MLC is moving. Is this tracking procedure capable of handling the MLC blocking problem?
- (4) Is this algorithm fast enough to track markers in nearly

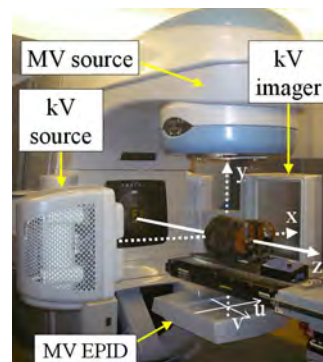


FIG. 1. A picture of the Trilogy with extended MV EPID, kV source, and kV imager. Room coordinates are illustrated.

real time? An analysis speed of 10 Hz is desirable for a nearly real-time 3D position tracking in order to gate treatment beam delivery.

## II. MATERIALS AND METHOD

### II.A. Hardware setup and computer calculation

All experiments were performed on a Varian Trilogy<sup>TM</sup> (Varian Medical System, Palo Alto, CA) with a MV EPID and a kV onboard imaging system as shown in Fig. 1. The onboard imaging system is located perpendicular to the treatment MV beam and consists of a kV x-ray tube together with an  $\alpha$ Si flat panel imager. Effective pixel sizes of the kV and MV detectors were 0.388 and 0.392 mm, respectively. Both detectors had a resolution of  $1024 \times 768$ , corresponding to an effective area of detection of approximately  $40 \text{ cm} \times 30 \text{ cm}$ . For both MV and kV systems, the default source-to-axis distances (SADs) and source-to-imager distances (SIDs) were set to 100 and 150 cm, respectively. Both dual MV energies, 6 and 15 MV, were used in this article. The MV EPID was capable of capturing images at a speed of 7.5 frames per second (fps) and 7.8 fps for 6 and 15 MV beams, respectively, while the kV imager had a capturing speed of 15 fps in the fluoroscopic or continuous imaging mode.

A sliced pelvic phantom was tested on a motion platform. Three gold cylindrical fiducial markers were embedded in the prostate position, each fiducial had a diameter of 1.2 mm and a length of 3.0 mm. The platform was driven by an electrical motor and could move linearly with an adjustable period between 2.0 and 6.0 s and its maximum motion amplitude was set to 1.0 cm.

A software program (C language) was developed to analyze projection images and obtain fiducial positions. All calculations were performed on a Dell Precision 470 workstation (3.4 GHz Xeon CPU and 4 GB RAM).

### II.B. Fiducial tracking algorithm

Figure 2 illustrates the complete procedure to track markers on open-field kV or MV images. Major steps are described in the following subsections.

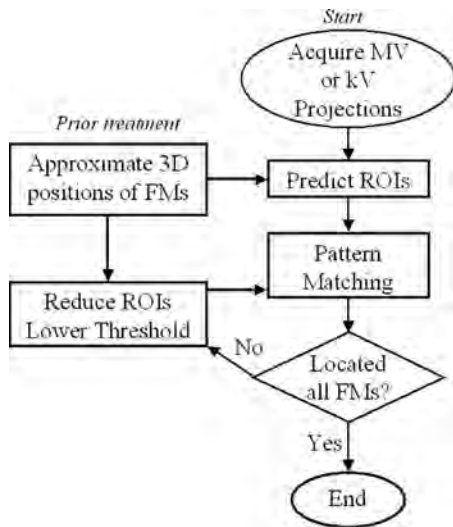


FIG. 2. Flow chart of detecting moving markers on open-field kV/MV images.

- Obtain approximate 3D positions of FMs from planning CT

The first step was to obtain approximate 3D positions of fiducials from the planning CT and then convert them to the treatment coordinates. A simple intensity-based search for the markers was performed on the planning CT. Due to the much larger CT numbers of the metallic markers relative to other anatomical structures, the markers were easily segmented from the image background. The displacement vector relating the CT iso-center to the treatment iso-center was then used to relocate marker CT coordinates relative to the treatment iso-center.

- Predict FM locations

The FM locations on projection images could be predicted by their approximate 3D positions obtained from prior planning CT images. For any FM having 3D position  $(x_M, y_M, z_M)$ , its expected projection location  $(u, v)$  on either the kV or MV detector was predicted by the following relationships:<sup>32</sup>

$$u = F \frac{\cos(\phi)x_M + \sin(\phi)y_M}{R - \sin(\phi)x_M + \cos(\phi)y_M} \quad (1)$$

$$v = F \frac{z_M}{R - \sin(\phi)x_M + \cos(\phi)y_M}, \quad (2)$$

where  $\phi$  was the Varian gantry angle,  $R$  was SAD, and  $F$  was SID. The  $x$  axis was in the lateral direction of patient couch, the  $y$  axis was in the anterior-posterior direction, the  $z$  axis was the superior-inferior (SI) direction, and the origin was the Linac's iso-center. The coordinates of the imagers  $(u, v)$  were defined on the imager and rotated with the gantry while  $v$  axis was parallel to  $z$  axis and  $u$ -axis laying the  $xy$  plane. Their origin is at the imager geometric center and their units are in mm or pixels (converted by effective pixel size).

The region to search for the fiducial marker was then

reduced to a small circular region of interest (ROI) centered on the predicted location. The ROI may be large or small depending on the range of tumor motion. Typically, a ROI with a radius of 75 pixels, or about 2 cm around the object, was found to be adequate for locating the moving markers in our studies.

For those markers located near each other, overlapping ROIs were combined into one larger ROI group containing both markers. In the case of multiple markers existing in the same ROI group, the detected marker positions in this ROI group were reordered based on the information from the planning CT results including the internal distances between markers and the shortest distances between detected and predicted marker projections, so that every detected fiducial would be identified without any confusion.

- Reduce ROIs

Two methods were used to reduce ROIs if possible. One method was to use the detected FM locations on the previous image during a continuous imaging course. Due to the short time interval between acquisitions ( $<0.1$  s) marker movement between consecutive images was limited so the new FM location should be close to the prior location. For instance, when the ROI radius was reduced to 25 pixels, this still covered a region with a radius of 6.7 mm, which corresponded to any movement with a speed less than 5 cm/s.

Another method was to use the relative positions among markers to locate undetected markers under the rigid body assumption. As long as one or more markers were detected, other markers' expected positions were calculated based on their relative locations to the detected markers by ignoring the internal motion among markers. The second search was usually performed in smaller ROIs with lower thresholds in order to detect markers with a weaker signal.

- Match patterns

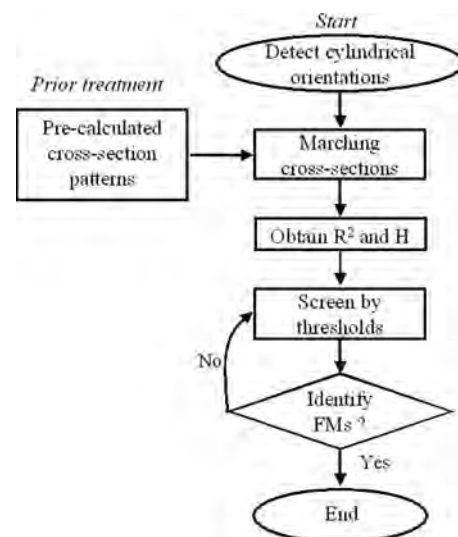


FIG. 3. Flow chart of pattern matching algorithm.

A novel fiducial tracking algorithm (pattern matching algorithm, as summarized in Fig. 3) has been developed to detect cylindrical fiducial markers on kV and MV projection images.<sup>20,30</sup> A cylindrical marker could be projected into different shapes depending on its orientation. A filter was applied to find the fiducial orientation at a given pixel. With this filter, we divided the angular space on a projection plane into eight bins. The average intensities of every bin adjacent to the given pixel were compared and the bin with the highest average intensity was presumed to correspond to the fiducial orientation. It should be noted that the cylindrical orientation results carried no information for most of the pixels and it was only valid for pixels on a cylindrical object.

A cylindrical marker can be projected into different

$$R_{u,v}^2 = \frac{\sum_{(i,j) \in \text{Pattern}} (f_{u+i,v+j} - \overline{f_{u,v}})(p_{i,j} - \bar{p})}{\sqrt{\sum_{(i,j) \in \text{Pattern}} (f_{u+i,v+j} - \overline{f_{u,v}})^2} \cdot \sqrt{\sum_{(i,j) \in \text{Pattern}} (p_{i,j} - \bar{p})^2}}, \quad (3)$$

$$H_{u,v} = \frac{\sum_{(i,j) \in \text{Pattern}} (f_{u+i,v+j} - \overline{f_{u,v}})(p_{i,j} - \bar{p})}{\sum_{(i,j) \in \text{Pattern}} (p_{i,j} - \bar{p})^2}, \quad (4)$$

where  $\overline{f_{u,v}}$  is the average intensity of the pattern region around pixel  $(u,v)$  and  $\bar{p}$  is the average intensity of the pattern distribution as given by

$$\overline{f_{u,v}} = \frac{1}{N} \sum_{(i,j) \in \text{Pattern}} f_{u+i,v+j}, \quad (5)$$

$$\bar{p} = \frac{1}{N} \sum_{(i,j) \in \text{Pattern}} p_{i,j}, \quad (6)$$

with  $N$  being the total pixel number of the pattern. The square of the coefficient of correlation or coefficient of determination for a linear regression is conveniently called  $R$  square or  $R^2$ . It varied from 0 (no correlation) to 1 (perfect correlation). The scaling factor,  $H$ , indicated the relative intensity of the object compared to the background. In an ideal case, the image was scaled from the pattern after a background shift,  $f_{u+i,v+j} = k \cdot p_{i,j} + b$ , where  $k$  and  $b$  were constants, and the pattern matching result would be  $R_{u,v}^2 = 1$  and  $H_{u,v} = k$ .

After the  $R^2$  and  $H$  values were calculated for every pixel in the ROIs, they were screened based on predefined thresholds. For pixels that passed the threshold, adjacent pixels were examined, and an overall length for the fiducial was determined. The presumed fiducial

shapes (length and orientation) depending on its orientation and the x-ray beam direction. However, its cross section, a narrow section perpendicular to the cylindrical orientation, is a unique feature and it only depends on the fiducial width and cylindrical orientation. For convenience, the cross-section patterns at all eight cylindrical orientations were precalculated for given widths. The cross section of every pixel was then matched with the predetermined cross-section pattern at the cylindrical orientation of that center pixel. At each pixel location  $(u,v)$  within ROIs, a comparison was made between the surrounding pixels ( $\{f_{u+i,v+j}\}$ ) and the pattern ( $\{p_{i,j}\}$ ) corresponding to the cylindrical orientation of that pixel. Two criteria were used to quantify the matching: The square of the correlation coefficient,  $R_{u,v}^2$ , and the scaling factor or intensity,  $H_{u,v}$ ,

would be rejected if its overall length was longer than a predefined maximum length.

#### • Calculate 3D coordinates from orthogonal dual projections

The nearly real-time 3D positions of fiducial markers were calculated from FM projections on two orthogonal imagers. Every marker  $(x_M, y_M, z_M)$  had two projections:  $(u_{MV}, v_{MV})$  on MV imager and  $(u_{kV}, v_{kV})$  on kV imager. The Trilogy might have a different SID and SAD,  $(F_{MV}, R_{MV})$  and  $(F_{kV}, R_{kV})$ , for the MV and kV imaging systems. Because the Trilogy kV imaging system always had a gantry angle of  $90^\circ$  larger than the MV imaging system, it is convenient to use the MV gantry angle to represent the Trilogy's rotation status. At a MV gantry angle of  $\phi$ , the fiducial marker's coordinates could be calculated from Eqs. (1) and (2):

$$\alpha = u_{MV} \frac{F_{kV} R_{MV} + R_{kV} u_{kV}}{F_{MV} F_{kV} + u_{MV} u_{kV}}, \quad (7)$$

$$\beta = u_{kV} \frac{F_{MV} R_{kV} - R_{MV} u_{MV}}{F_{MV} F_{kV} + u_{MV} u_{kV}}, \quad (8)$$

$$x_{FM} = \cos(\phi) \cdot \alpha - \sin(\phi) \cdot \beta, \quad (9)$$

$$y_{FM} = \sin(\phi) \cdot \alpha + \cos(\phi) \cdot \beta, \quad (10)$$

$$z_{FM} = \frac{1}{2} \left( \frac{R_{MV} + \beta}{F_{MV}} v_{MV} + \frac{R_{kV} - \alpha}{F_{kV}} v_{kV} \right). \quad (11)$$

## II.C. Experiments

### • Speed of moving FMs

The motion of fiducials would blur images and impede tracking. The maximum detectable moving speed is an important factor of this detection procedure. We tracked fiducial markers implanted in a phantom, which moved at various speeds, on open-field kV and MV images. The maximum linear speed can be calculated by Eq. (12)

$$\text{speed} = \frac{2\pi A}{T}, \quad (12)$$

where  $A$  was the motion amplitude and it was 10.0 mm in this study and  $T$  was the motion period.

Detection efficiency has been defined as the ratio between total number of detected fiducials and total number of fiducials in all images.

### • Test the effects of MV scattering on kV imaging

During simultaneous MV and kV imaging, scattering of the MV beam would significantly diminish kV imaging quality, but the diminished kV image might still be good enough to track fiducial markers. In general, the quality of kV images was inversely proportional to MV beam size and directly proportional to kV SID. In this study, the kV images were analyzed by varying the MV field size from the maximum of  $26 \times 20 \text{ cm}^2$  (open field) to  $10 \times 10 \text{ cm}^2$  and increasing the SID from 150.0 to 181.8 cm. Since the typical human abdomen has different thickness in lateral (LAT) and anterior-posterior directions and MV and kV beams are in orthogonal directions, the scattering effects on both AP and LAT directions were tested here.

### • Tracking fiducials with the presence of a MLC

In order to track fiducials during a treatment course, two phantom verification plans for 3DCRT and IMRT treatments from real patients were prepared on an Eclipse (Varian Medical System, Palo Alto, CA). The 3DCRT plan contains four fields: AP, PA, and two LAT fields. The step and shoot IMRT treatment plan included seven fields and 74 segments in total. All MV and kV images were acquired simultaneously during the delivery of the treatment plans. The pelvic phantom was placed on the motion platform and both plans were delivered multiple times at different motion cycle periods.

Figure 4 shows the flow chart to track markers when the MLC was moving (i.e., for an IMRT plan). An identical tracking method was applied for kV images as described in Sec. II B. The kV results were then used to help locate fiducials on MV images as shown in Fig. 4. Compared to tracking markers on open-field images, there was an additional step to screen and define the MLC field after MV images were acquired. An intensity threshold was computed from the minimum and maximum intensity of the whole image and then used for segmenting the MV field from the MLC blocked area by a simple intensity based screening process. The image was also linearly normalized for consistent analysis

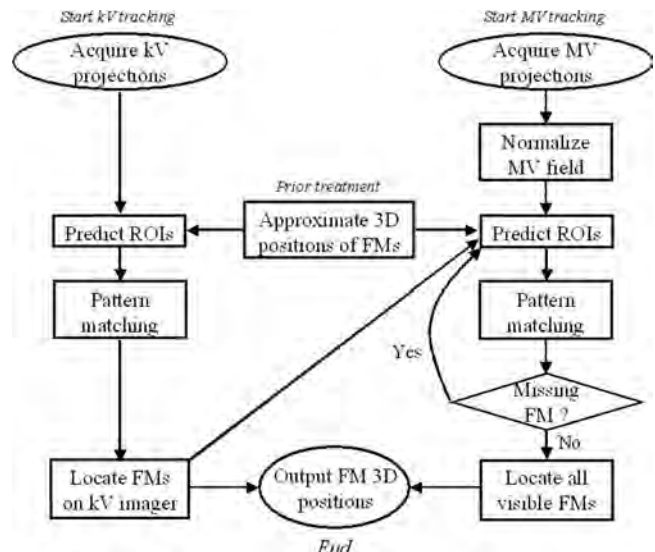


FIG. 4. Flow chart of detecting moving markers on IMRT kV/MV images.

across a series of projections. For convenience, the maximum intensity was normalized to 1000 while the minimum intensity was normalized to 0.

When using the treatment MV beam for in-line imaging, a potential difficulty is that the fiducials may be partially or completely blocked by the MLC at certain segments. There are five sources of information can help in this situation. First, the coordinates of any fiducial from the orthogonal kV imaging are always available. This piece of information is very valuable in estimating the position of this fiducial on MV imager because the kV projection result indicates that the fiducial locates on a kV x-ray trace from the kV source to the kV projection. Its possible projection on MV imager must be on the projection of this kV x-ray trace. Coordinates of kV and MV projections of the same fiducial on the common axis, the  $v$  axis, are close to each other. More details are presented in the Appendix. Second, fiducial kinetics obtained at the previous time point can be utilized by a prediction algorithm to facilitate estimation of marker position as discussed in the subsection II B. **Fiducial tracking algorithm, Reduce ROIs.** Third, the detected fiducials' positions could be helpful to locate other blocked fiducials based on their relative positions as discussed in the subsection II B. **Fiducial tracking algorithm, Reduce ROIs.** Fourth, the MLC leaf positions are always available from the EPID images, which can serve as a useful landmark for fiducial position estimation because the fiducials should be either detected or in the MLC leaf blocked area. Finally, the 3D movement of the markers captured by the pretreatment 4D CBCT and simulation 4D CT is also available for positional prediction. For example, an elliptic ROI may be used for a known tumor- motion direction instead of a circular ROI. This will reduce the size of possible MV projection locations in certain directions. Furthermore, it would reduce the length of 1D possible

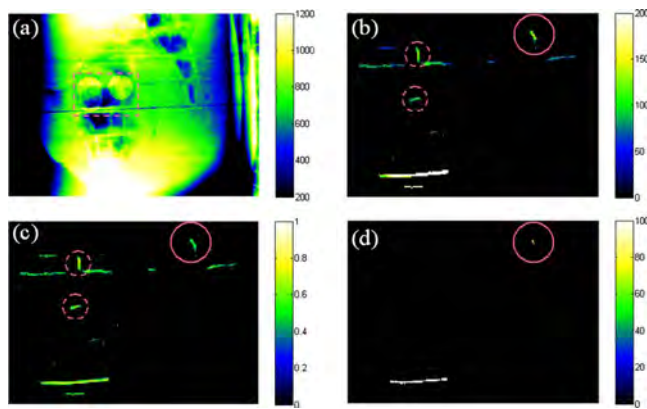


FIG. 5. Typical fiducial tracking. (a) Projection image in which the ROIs were highlighted. (b) Intensity results of pattern matching in the dash rectangle region of (a). (c)  $R^2$  results of pattern matching in the dash rectangle region of (a). (d) Qualified features after the primary search.

MV projection locations predicted by orthogonal kV imaging results.

### III. RESULTS

#### • An Example of fiducial tracking

Figure 5 illustrates a difficult fiducial tracking case on a lateral MV image. The ROIs for three fiducials were predicted by the planning CT results and highlighted in Fig. 5(a), in which the dash rectangle displayed a region including all ROIs. After pattern matching was performed on every pixel in the ROIs, intensity and  $R^2$  results were obtained as shown in Figs. 5(b) and 5(c), respectively. The intensity and  $R^2$  thresholds were determined based on the maximum values of that ROI group and predefined minimum values. After threshold screening, only one feature was qualified as a fiducial [enclosed by a solid circle in Fig. 5(d)] while another feature was rejected because its length was too long.

The second search then followed. The positions of undetected markers were closely estimated by the relative shifts among markers as enclosed by the small dashed circles in Figs. 5(b) and 5(c). After the thresholds were set at lower values, all markers were successfully detected.

#### • Speed limit for detecting moving fiducials

MV and kV image series were analyzed with the motion platform moving at different periods. Figure 6(a) illustrates the projection locations of one marker when the motion platform was moving at an amplitude of 10.0 mm with a period of 4 s. The traces were fit to sine waves shown in the Fig. 6(a). The fitting results indicated that the motion amplitudes for both axes were 3.38 and 9.49 mm, respectively. This means the total amplitude is 10.07 mm ( $=\sqrt{3.38^2+9.49^2}$ ), which is very close to the nominal amplitude (10.0 mm). Figure 6(b) illustrates the difference between measured projections and fitting results and the variations are less than 0.8 mm.

Images of the moving phantom were analyzed to test

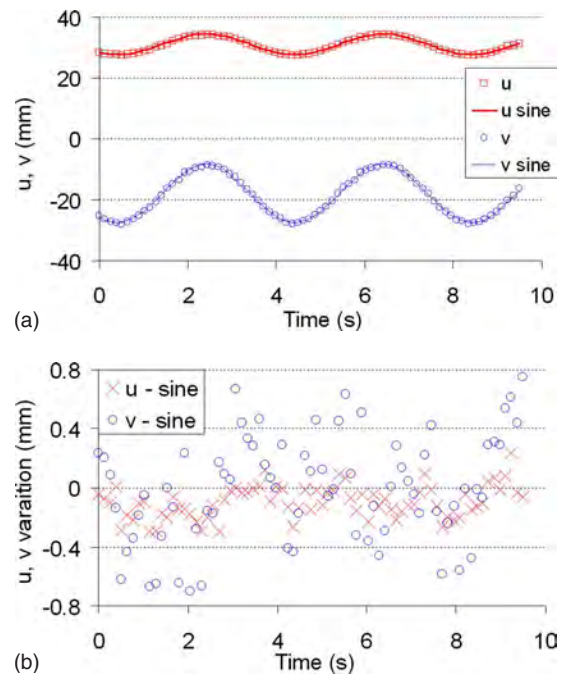


FIG. 6. Marker Detecting Accuracy. (a) Measured the projections against fitting results. (b) Differences between measured the projections against fitting results.

the detection efficiency for moving fiducials. In total, 877 kV and 456 MV images on both lateral ( $90^\circ$  gantry angle) and AP directions were acquired and analyzed for the motion study. It is always easier to detect markers on the AP images than on the LAT images, partially because of the increased scattering at the LAT direction. All markers in kV images and AP MV images (either 6 MV or 15 MV energy) were successfully detected (detection efficiency of 100%). For the difficult cases, detection efficiencies on LAT MV images are illustrated in Fig. 7. A detection efficiency of better than 95% is achieved for both MV energies when the motion period is 4 s or longer, which correlates to a maximum linear speed of 1.6 cm/s or slower.

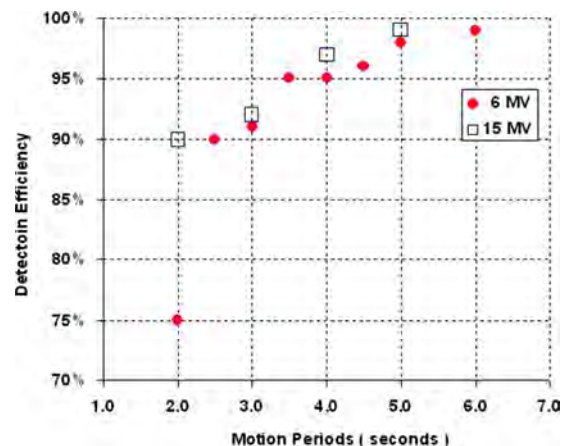


FIG. 7. Detection efficiencies of moving markers on LAT MV images of dual energies.

TABLE I. Summary of the kV detection efficiencies affected by MV field size and kV SID. Two efficiencies present MV field at AP and LAT directions, respectively.

kV SID (cm)		181.8		166.7		150.0	
MV direction		AP	LAT	AP	LAT	AP	LAT
MV field size (cm <sup>2</sup> )	10×10	100%	100%	100%	100%	100%	100%
	15×15	100%	100%	100%	100%	100%	4%
	26×20	100%	76%	61%	13%	6%	1%

#### • Effects of MV beam scattering on kV imaging

Usually scattering of the simultaneous MV and kV beams can cause concern for degrading the quality of the kV image. Fortunately, here only the fiducial markers are of interest and our analysis is capable of suffering a certain degree of scattering. The kV SID was extended further to reduce the scattering from MV beams; 842 kV images were acquired and analyzed while varying the SID and MV field size; the detection efficiency results are summarized in Table I. As expected, either a smaller MV field or a larger SID leads to better detection. It was found that the markers in kV images could be successfully analyzed even with the scattering from a common treatment MV field (10×10 cm or less). In addition, when our 3DCRT and IMRT plans were delivered, more than 5000 kV images were acquired and analyzed and all markers were successfully detected with a detection efficiency of 100%. This guarantees that kV imaging is always applicable for tracking fiducials during treatment.

#### • Tracking FMs in the presence of a MLC

The IMRT plan was delivered once without phantom motion and once with a motion period of 4.0 s. All MV and kV images were acquired and analyzed. Special attention was paid on treatment segments with fiducials

partially or completely blocked by the MLC. Figure 8 illustrates fiducial tracking on the MV field at a gantry angle of 235° with the static phantom. The fiducial coordinates obtained from orthogonal kV images were used to help locate projections on MV images [as shown in Fig. 8(a)]. The possible MV projection might not be exactly horizontal due to the divergence of the kV x-ray trace (as discussed in the Appendix). As long as a fiducial was detected at any segment [Figs. 8(c)–8(i)], the blocked fiducials could be estimated very closely by fiducial relative positions (circles in the MLC blocked area) and common axis kV coordinates (solid lines). The estimated position was limited on a horizontal line with a length corresponding internal deformation up to  $\pm 5$  mm. It is still possible that all fiducials are outside of the MV field because of small IMRT segments as shown in Fig. 8(b). In this case, the possible positions could be estimated as elliptic ROIs by 3D planning CT data and available 4D CT results. Their long and short axes correspond to possible motion of  $\pm 2$  cm and  $\pm 1$  cm in two directions, respectively. The orthogonal kV imaging results limit the estimation to horizontal lines with a length corresponding motion up to  $\pm 1$  cm.

The 3DCRT plan was delivered three times with the motion period varied at 2.0, 3.0, and 4.0 s. All MV and kV images were acquired and analyzed. Figure 9 displays the simultaneous MV and kV images when the phantom was moving. Most of the markers were suc-

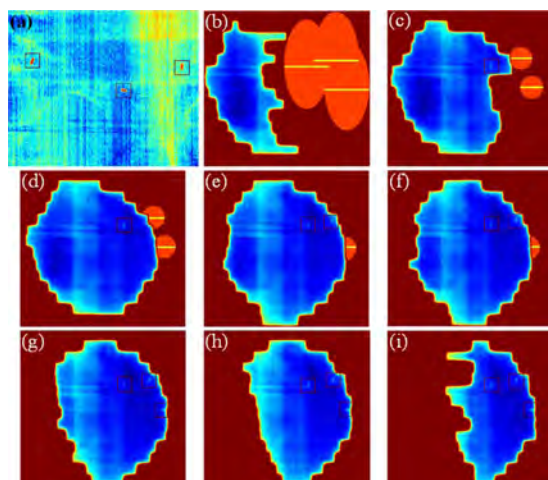


FIG. 8. Detect fiducials during an IMRT treatment. (a) Orthogonal kV image. (b)–(i) MV images for every segment. Detected fiducials were enclosed in square boxes. Ovals or circles in the MLC blocked region indicate the predicted fiducial projections and the horizontal line indicate the predicted fiducial projections based on orthogonal kV imaging results.

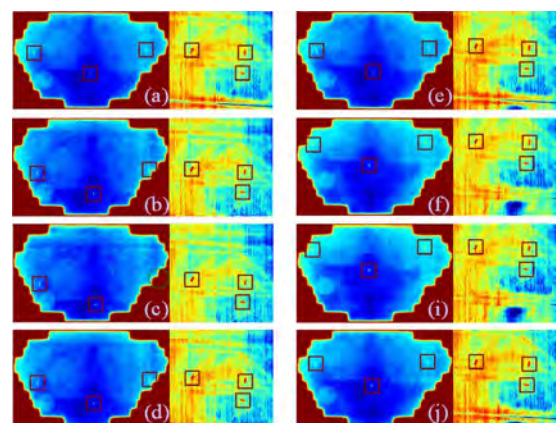


FIG. 9. Simultaneous MV and kV images with a MV gantry angle of 180° and a motion period of 4 s.

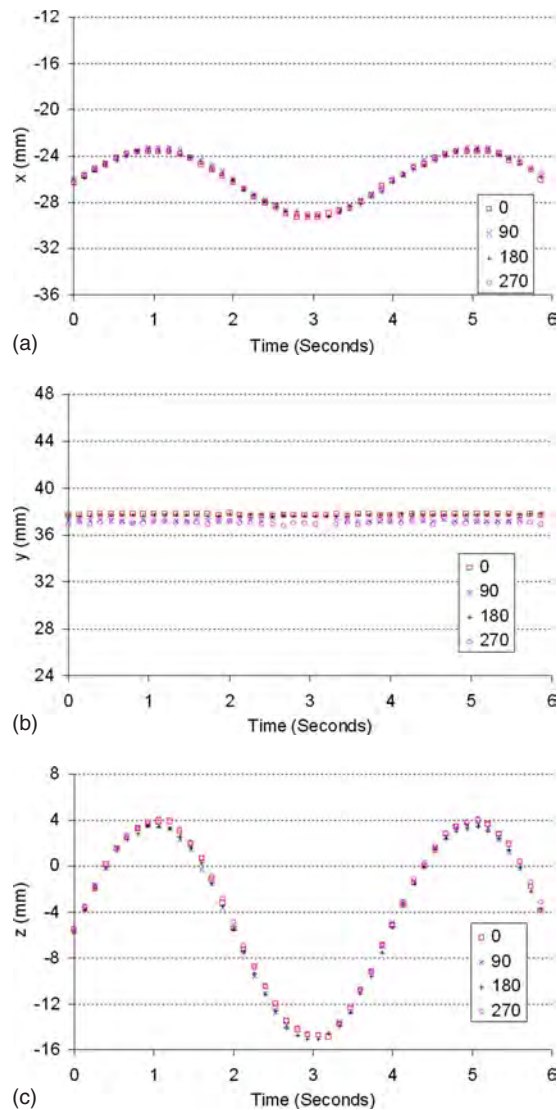


FIG. 10. Three-dimensional coordinates of one marker during the treatment. Results from four fields were synchronized for comparison purpose; (a)  $x$  coordinates, (b)  $y$  coordinates, (c)  $z$  coordinates.

successfully detected as enclosed in solid rectangles. Nearly real-time 3D positions of fiducial markers were calculated at all fields based on Eqs. (7)–(11). After synchronizing the results from different fields, it was found that results from different fields were within  $\pm 0.8$  mm of their average positions. Figure 10 illustrates 3D coordinates of one moving marker in every field with a period of 4 s.

It should be noted that the presence of a MLC does not affect the detection efficiency dependence on motion speed and all fiducial markers on every kV image were successfully detected.

#### • Performance of analysis software

Special attention was paid on the analysis software programming. It is essential to compute the location of a marker quickly so to be able to track the markers at a speed of 10 fps or higher. Most of the calculation time was spent on the pattern matching, including determin-

ing orientation and calculating intensity and  $R^2$ . A complete search on  $1024 \times 768$  pixels image costs about 1 s. The searching region of three markers with a radius of 75 pixels reduces the calculation time by an order of magnitude. The average search time for three markers was 0.08 s per frame.

Basically, kV and MV images could be analyzed independently. It is generally much easier to track markers on kV images than on MV images not only because kV images have better contrast but also because fiducials are always visible in kV images. However, this does not mean that double the calculation time is needed for simultaneous kV and MV image analysis because the kV tracking results might be used to reduce MV ROIs as shown in Fig. 4 in addition to the other two methods to reduce ROIs. This process significantly reduces the size of ROIs on MV images and further reduces the computation time. It is found that 0.1 s analysis time per kV/MV pair is achievable on our current single CPU architecture. Reduced computation time is expected if parallel computation is implemented on a multiple-core processor.

## IV. DISCUSSION

The four studies presented in this article pave the way to track 3D positions of multiple moving fiducial markers during treatment in nearly real time. We demonstrate that our algorithm is capable of tracking fast moving fiducial markers by simultaneous kV and treatment MV imaging. Furthermore, the analysis speed is fast enough to report nearly real-time 3D positions of the markers. It is also worthwhile to mention that this procedure does not need any assumed motion model. Although all motion experiments were performed on a periodic moving platform, the algorithm does not take this periodicity into consideration, meaning these results should just as easily apply to nonperiodic motion. This is also why the term nearly real-time 3D position was used instead of 4D position because the terminology of 4D usually refers to a periodic motion particularly when it is associated with 4D CT. This procedure detects any regular, irregular, or sudden motion as long as the maximum speed is not very fast.

We can track marker motion up to a period of 2 s in kV images, not only because of much higher contrast of kV images than MV images, but also because of its higher capture speed (15 fps). Currently, the acquisition speed of the MV imaging is less than 8 fps, which means that the marker may move about 2 mm ( $\sim 7.5$  pixels on imager) at a speed of 1.6 cm/s during one acquisition (marker width  $\sim 5$  pixels). The blurring induced by motion and small size of the marker make it difficult to track fiducials on MV images, particularly those with low image quality. It should also be noted that better hardware will improve performance, e.g., quicker MV image acquisition.

This method is suitable for tracking any tumor motion as long as fiducial markers or surgical clips are available. It is not limited to a certain type of site although the studies were performed on a pelvic phantom.

The proposed procedure will be an economic solution to nearly real-time tracking of tumor motion since more and more linear accelerators are coming equipped with an on-board kV imaging system. This procedure does not need any extra expensive equipment such as multiple kV imaging sets.

Another advantage of this procedure over stereoscopic kV tracking systems is that using the treatment beam as part of tracking reduces extra dose to the patient. Although kV imaging dose is still a concern, we would like to emphasize that the patient dose from a single kV imaging set here is 50% less than that from stereoscopic kV imaging sets. In this study, we used the typical kV CBCT imaging parameters (125 kV, 80 ms, and 25 mA). It has been reported that the dose to the soft tissue for such a CBCT scan (with 630 images) is  $\sim 5$  cGy.<sup>33</sup> Since an acquisition speed of 7.5 fps is sufficient, the kV dose is about 3.6 cGy/Min ( $5 \text{ cGy}/630 \times (7.5/\text{s}) = 0.06 \text{ cGy/s}$ ). A typical IMRT treatment has a beam on time of about 2 min for a 200 cGy dose delivery to the target. This implies that the kV imaging dose is about 7.2 cGy. However, this represents the worst case scenario where the kV beam is on throughout the IMRT beam delivery process. In reality, it is not necessary to keep the kV imaging system on all the time. The kV imaging may be switched off during the step mode of IMRT delivery. In addition, the kV field size can be reduced according to the fiducial motion range. All these strategies may further reduce the kV imaging dose.

The proposed hybrid MV/kV imaging technique is readily applicable to facilitate conventional 3D radiation therapy by providing real-time information of the implanted fiducials. When using IMRT MV beam for in-line imaging, a potential difficulty is that the fiducials may be partially or completely blocked by the MLC leaves at a certain segment(s). There are four sources of information that help to estimate the 3D coordinates of the MLC-blocked fiducial in this situation. First, the coordinates of the fiducial in the plane perpendicular to the kV beam are still available from kV imaging. This piece of information is very valuable because it significantly reduces the dimensionality of the problem. Second, the fiducial kinetics attained by the kV/MV system at earlier time when the marker(s) are not blocked can be utilized to adaptively predict the “missing” coordinate of the marker in combination with the kV information. Third, the MLC leaf positions are always available from the EPID images, which can serve as a useful landmark for fiducial position estimation. Finally, the 3D movement of the markers captured by the pretreatment CBCT and planning CT is also available as *a priori* knowledge for better positional estimation. The development of such a multiple input single output adaptive prediction algorithm is still in progress. Because there is only one coordinate that needs to be estimated for a short interval of time, we foresee no major difficulty in accomplishing an accurate positional estimation. This remains true in a rare

situation when all the fiducials are blocked by a MLC segment. For certain types of tumors that deform little during the treatment process (e.g., the prostate), the positions of unblocked fiducials can be employed as landmarks in allocating the MLC-blocked fiducial(s).

During our 3DCRT verification plan delivery, at least two of three fiducials were visible in every field even when the phantom was on a motion platform. All fiducials were visible in 95% of the segments. During the delivery of the verification IMRT plan, at least one fiducial was visible in about 75% of the segments. This percentage is highly dependent on the case and the treatment planning system. To increase the visible time of a fiducial, it is possible to add one or more imaging segments (i.e., a segmented field with small monitor unit for the purpose of imaging the fiducials) to the treatment IMRT leaf sequences to facilitate the detection of a fiducial at a certain point of IMRT delivery. Another avenue of research is to take the fiducial information into consideration during the IMRT inverse planning process. With the development of segment-based dose optimization methods,<sup>34,35</sup> it should be feasible to ensure the visibility of at least one fiducial during the inverse planning process. Of course, the addition of this type of constraint in inverse planning may compromise the achievable dose distribution. But it is arguable that the trade-off will likely be minimal because, after all, the fiducials are all inside the tumor target volume and represent high dose points. We are currently actively studying this issue and the results will be reported elsewhere.

## V. CONCLUSION

The four studies presented in this article pave the way to track nearly real-time 3D positions of multiple moving fiducial markers during treatment. It is demonstrated that this proposed process is capable of tracking fast moving fiducial markers (up to 1.6 cm/s) by analyzing simultaneous kV and treatment MV images. The analysis speed is as fast as 10 fps and can report nearly real-time 3D positions of markers with submillimeter accuracy.

## ACKNOWLEDGMENTS

This work was supported in part by grants from the Department of Defense (PC040282), the National Cancer Institute (1R01 CA104205), and the Komen Breast Cancer Foundation (BCTR0504071).

## APPENDIX

Any fiducial projects on kV imager at  $P$ ,  $(u_{kV}, v_{kV})$ . This fiducial must be on the line of KP (as shown in Fig. 11):

$$\begin{cases} x = R_{kV} - \gamma \cdot F_{kV} \\ y = \gamma \cdot u_{kV} \\ z = \gamma \cdot v_{kV} \end{cases} \quad (\text{A1})$$

While  $\gamma$  is arbitrary,  $F_{kV}$  and  $R_{kV}$  are the source-imager distance (SID) and the source-axis distance (SAD) of kV system, respectively.

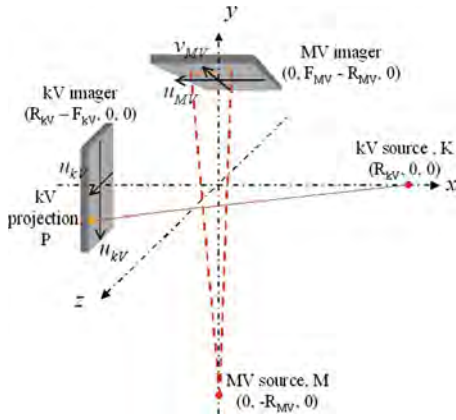


FIG. 11. Schematic diagram of relationship between kV and MV projections of the same fiducial.

This fiducial projects on MV imager on plane MKP (as shown in Fig. 11),

$$x + b \cdot (y + R_{MV}) + c \cdot z = 0, \quad (A2)$$

while  $b$  and  $c$  are constants and  $R_{MV}$  is the SAD of MV system. Input Eq. (A1) to Eq. (A2), we have

$$(R_{kV} - \gamma \cdot F_{kV}) + b \cdot \gamma \cdot u_{kV} + b \cdot R_{MV} + c \cdot \gamma \cdot v_{kV} = 0$$

or

$$R_{kV} + b \cdot R_{MV} + \gamma \cdot (-F_{kV} + b \cdot u_{kV} + c \cdot v_{kV}) = 0. \quad (A3)$$

Since  $\gamma$  is arbitrary, we get

$$b = -\frac{R_{kV}}{R_{MV}} \quad (A4)$$

and

$$-F_{kV} + b \cdot u_{kV} + c \cdot v_{kV} = 0,$$

or

$$c = \frac{F_{kV}R_{MV} + R_{kV}u_{kV}}{R_{MV}v_{kV}}. \quad (A5)$$

The projection on MV imager  $[B, (u_{MV}, v_{MV})]$  lies on a line in the MV imager plane  $v = F_{MV} - R_{MV}$ , so that the projection locations of A and B have a relationship:

$$\frac{v_{MV}}{v_{kV}} = \frac{F_{MV}R_{kV} + R_{MV}u_{MV}}{F_{kV}R_{MV} + R_{kV}u_{kV}}$$

or

$$(F_{kV}R_{MV} + R_{kV}u_{kV}) \cdot v_{MV} - R_{MV}v_{kV}u_{MV} = F_{MV}R_{kV}v_{kV}. \quad (A6)$$

Typically, both MV and kV systems have a SAD of 100 cm and a SID of 150 cm, approximately,

$$\frac{v_{MV}}{v_{kV}} \approx 1 + \frac{u_{kV} - u_{MV}}{F_{MV}}.$$

For a small target, whose fiducials are within a region with a

radius of 2 cm,  $|v_{MV}/v_{kV}|$  is usually very close to unity within  $\pm 4\%$ , i.e.,  $v_{MV}$  and  $v_{kV}$  are close to each other.

<sup>a)</sup> Author to whom correspondence should be addressed. Electronic mail: lei@reyes.stanford.edu

<sup>1</sup>IMRT Collaborative Working Group, "Intensity-modulated radiotherapy: Current status and issues of interest," *Int. J. Radiat. Oncol., Biol., Phys.* **51**(4), 880–914 (2001).

<sup>2</sup>J. M. Galvin et al., "Implementing IMRT in clinical practice. A joint document of the American Society for Therapeutic Radiology and Oncology and the American Association of Physicists in Medicine," *Int. J. Radiat. Oncol., Biol., Phys.* **58**(5), 1616–1634 (2004).

<sup>3</sup>K. Kitamura et al., "Three-dimensional intrafractional movement of prostate measured during real-time tumor-tracking radiotherapy in supine and prone treatment positions," *Int. J. Radiat. Oncol., Biol., Phys.* **53**(5), 1117–1123 (2002).

<sup>4</sup>J. M. Crook et al., "Prostate motion during standard radiotherapy as assessed by fiducial markers," *Radiother. Oncol.* **37**(1), 35–42 (1995).

<sup>5</sup>R. I. Berbeco et al., "Residual motion of lung tumors in end-of-inhale respiratory gated radiotherapy based on external surrogates," *Med. Phys.* **33**(11), 4149–4156 (2006).

<sup>6</sup>Y. Seppenwoolde et al., "Precise and real-time measurement of 3D tumor motion in lung due to breathing and heartbeat, measured during radiotherapy," *Int. J. Radiat. Oncol., Biol., Phys.* **53**(4), 822–834 (2002).

<sup>7</sup>Y. Xie et al., "Intrafraction motion of the prostate in cyberknife hypofractionated radiotherapy," *Int. J. Radiat. Oncol., Biol., Phys.* (2007). (submitted).

<sup>8</sup>K. L. Zhao et al., "Evaluation of respiratory-induced target motion for esophageal tumors at the gastroesophageal junction," *Radiother. Oncol.* **84**(3), 283–289 (2007).

<sup>9</sup>H. Shirato et al., "Speed and amplitude of lung tumor motion precisely detected in four-dimensional setup and in real-time tumor-tracking radiotherapy," *Int. J. Radiat. Oncol., Biol., Phys.* **64**(4), 1229–1236 (2006).

<sup>10</sup>L. Xing et al., "Overview of image-guided radiation therapy," *Med. Dosim.* **31**(2), 91–112 (2006).

<sup>11</sup>M. J. Murphy, "Fracking moving organs in real time," *Semin. Radiat. Oncol.* **14**(1), 91–100 (2004).

<sup>12</sup>P. C. Chi et al., "Relation of external surface to internal tumor motion studied with cine CT," *Med. Phys.* **33**(9), 3116–3123 (2006).

<sup>13</sup>H. Shirato et al., "Real-time tumour-tracking radiotherapy," *Lancet* **353**(9161), 1331–1332 (1999).

<sup>14</sup>P. Kupelian et al., "Multi-institutional clinical experience with the Calypso System in localization and continuous, real-time monitoring of the prostate gland during external radiotherapy," *Int. J. Radiat. Oncol., Biol., Phys.* **67**(4), 1088–1098 (2007).

<sup>15</sup>A. L. Boyer et al., "A review of electronic portal imaging devices (EPIDs)," *Med. Phys.* **19**(1), 1–16 (1992).

<sup>16</sup>L. Dong et al., "Verification of radiosurgery target point alignment with an electronic portal imaging device (EPID)," *Med. Phys.* **24**(2), 263–267 (1997).

<sup>17</sup>M. G. Herman et al., "Technical aspects of daily online positioning of the prostate for three-dimensional conformal radiotherapy using an electronic portal imaging device," *Int. J. Radiat. Oncol., Biol., Phys.* **57**(4), 1131–1140 (2003).

<sup>18</sup>P. J. Keall et al., "On the use of EPID-based implanted marker tracking for 4D radiotherapy," *Med. Phys.* **31**(12), 3492–3499 (2004).

<sup>19</sup>H. Dehnad et al., "Clinical feasibility study for the use of implanted gold seeds in the prostate as reliable positioning markers during megavoltage irradiation," *Radiother. Oncol.* **67**(3), 295–302 (2003).

<sup>20</sup>A. Nederveen, J. Lagendijk, and P. Hofman, "Detection of fiducial gold markers for automatic on-line megavoltage position verification using a marker extraction kernel (MEK)," *Int. J. Radiat. Oncol., Biol., Phys.* **47**(5), 1435–1442 (2000).

<sup>21</sup>A. J. Nederveen, J. J. Lagendijk, and P. Hofman, "Feasibility of automatic marker detection with an a-Si flat-panel imager," *Phys. Med. Biol.* **46**(4), 1219–1230 (2001).

<sup>22</sup>J. Pouliot et al., "(Non)-migration of radiopaque markers used for on-line localization of the prostate with an electronic portal imaging device," *Int. J. Radiat. Oncol., Biol., Phys.* **56**(3), 862–866 (2003).

<sup>23</sup>D. C. Schiffrer et al., "Daily electronic portal imaging of implanted gold seed fiducials in patients undergoing radiotherapy after radical prostatectomy," *Int. J. Radiat. Oncol., Biol., Phys.* **67**(2), 610–619 (2007).

- <sup>24</sup>L. Smith *et al.*, "Automatic detection of fiducial markers in fluoroscopy images for on-line calibration," *Med. Phys.* **32**(6), 1521–1523 (2005).
- <sup>25</sup>H. Shirato *et al.*, "Physical aspects of a real-time tumor-tracking system for gated radiotherapy," *Int. J. Radiat. Oncol., Biol., Phys.* **48**(4), 1187–1195 (2000).
- <sup>26</sup>T. R. Willoughby *et al.*, "Evaluation of an infrared camera and X-ray system using implanted fiducials in patients with lung tumors for gated radiation therapy," *Int. J. Radiat. Oncol., Biol., Phys.* **66**(2), 568–575 (2006).
- <sup>27</sup>X. Tang, G. C. Sharp, and S. B. Jiang, "Fluoroscopic tracking of multiple implanted fiducial markers using multiple object tracking," *Phys. Med. Biol.* **52**(14), 4081–4098 (2007).
- <sup>28</sup>K. Kitamura *et al.*, "Tumor location, cirrhosis, and surgical history contribute to tumor movement in the liver, as measured during stereotactic irradiation using a real-time tumor-tracking radiotherapy system," *Int. J. Radiat. Oncol., Biol., Phys.* **56**(1), 221–228 (2003).
- <sup>29</sup>R. D. Wiersma, W. Mao, and L. Xing, "Combined kV and MV imaging for real-time tracking of implanted fiducial markers," *Med. Phys.* **35**(4), 1191–1198 (2008).
- <sup>30</sup>W. Mao, R. Wiersma, and L. Xing, "Fast internal marker tracking algorithm for onboard MV and kV imaging systems," *Med. Phys.* **35**(5), 1942–1949 (2008).
- <sup>31</sup>W. Luo *et al.*, "Effect of Mv scatter on Kv image quality during simultaneous Kvmv imaging," *Int. J. Radiat. Oncol., Biol., Phys.* **69**(3), S671 (2007).
- <sup>32</sup>W. Mao *et al.*, "CT image registration in sinogram space," *Med. Phys.* **34**(9), 3596–3602 (2007).
- <sup>33</sup>N. Wen *et al.*, "Dose-delivered from Varian's CBCT to patients receiving IMRT for prostate cancer," *Phys. Med. Biol.* **52**(8), 2267–2276 (2007).
- <sup>34</sup>D. M. Shepard *et al.*, "Direct aperture optimization: A turnkey solution for step- and-shoot IMRT," *Med. Phys.* **29**(6), 1007–1018 (2002).
- <sup>35</sup>C. Cotrutz and L. Xing, "Segment-based dose optimization using a genetic algorithm," *Phys. Med. Biol.* **48**(18), 2987–2998 (2003).

# Fast internal marker tracking algorithm for onboard MV and kV imaging systems

W. Mao, R. D. Wiersma, and L. Xing<sup>a)</sup>

Department of Radiation Oncology, Stanford University School of Medicine, Stanford, California 94305-5847

(Received 12 October 2007; revised 31 January 2008; accepted for publication 26 February 2008; published 23 April 2008)

Intrafraction organ motion can limit the advantage of highly conformal dose techniques such as intensity modulated radiation therapy (IMRT) due to target position uncertainty. To ensure high accuracy in beam targeting, real-time knowledge of the target location is highly desired throughout the beam delivery process. This knowledge can be gained through imaging of internally implanted radio-opaque markers with fluoroscopic or electronic portal imaging devices (EPID). In the case of MV based images, marker detection can be problematic due to the significantly lower contrast between different materials in comparison to their kV-based counterparts. This work presents a fully automated algorithm capable of detecting implanted metallic markers in both kV and MV images with high consistency. Using prior CT information, the algorithm predefines the volumetric search space without manual region-of-interest (ROI) selection by the user. Depending on the template selected, both spherical and cylindrical markers can be detected. Multiple markers can be simultaneously tracked without indexing confusion. Phantom studies show detection success rates of 100% for both kV and MV image data. In addition, application of the algorithm to real patient image data results in successful detection of all implanted markers for MV images. Near real-time operational speeds of  $\sim 10$  frames/sec for the detection of five markers in a  $1024 \times 768$  image are accomplished using an ordinary PC workstation. © 2008 American Association of Physicists in Medicine. [DOI: [10.1118/1.2905225](https://doi.org/10.1118/1.2905225)]

Key words: fiducial tracking, IGRT, image guidance

## I. INTRODUCTION

Modern conformal radiation therapy techniques, such as intensity-modulated radiation therapy (IMRT), can provide radiation doses that closely conform to the tumor dimensions while sparing sensitive structures.<sup>1,2</sup> To be optimally effective, these techniques require a high geometric precision in both tumor localization and patient treatment setup. The presence of inter and intrafraction organ motion uncertainties can therefore reduce the benefit of using a highly conformal radiotherapy technique. For instance, intrafractional respiratory or prostate based tumor motion can lead to tumor displacements up to 2–3 cm over the course of routine radiotherapy.<sup>3–9</sup> The use of image-guided radiation therapy (IGRT) is a promising candidate to ensure proper targeting in radiation treatment deliveries.<sup>10</sup> Due to the dynamical nature of human anatomy, it is most advantageous when IGRT can be performed in real-time in order to ensure an accurate delivery of the planned conformal dose distribution.<sup>11</sup>

Several methods of obtaining real-time tumor position are available, and these can be categorized as being either indirect (external surrogate-based) or direct (fiducial/image) in nature. In general, indirect tumor location methods, such as external skin marker tracking or breath monitoring techniques, rely on the correlation between external body parameters and the tumor.<sup>5,12</sup> In reality, the relationship between external parameters and internal organ motion is complex

and a large uncertainty may be present in predicting the tumor location based on external signals. A direct tumor position measurement is therefore highly desirable for therapeutic guidance. In the last decade, a number of direct real-time 3D tumor tracking methods have been implemented, primarily using fluoroscopy<sup>5,11,13</sup> or magnetic field localization.<sup>14</sup> In addition, the feasibility of using an electronic portal imaging device (EPID) and stereoscopic x-ray imaging for tumor tracking has been explored.<sup>3,5,6,15–26</sup>

To be clinically useful, an internal marker tracking algorithm should reliably segment markers from varying complex anatomic image backgrounds, be able to track multiple markers simultaneously without indexing confusion, and be able to operate at near real-time speeds. Generally, marker segmentation algorithms based on pixel intensity tend to fail when markers are in the vicinity of high contrast structures such as bone. A more reliable solution is the use of template matching, as demonstrated by Shirato *et al.*, in the tracking of a spherical gold marker using multiple kV fluoroscopic imaging systems.<sup>25</sup> Tang *et al.* further extended the template matching technique to include detection of cylindrically shaped markers on an in-house built stereoscopic kV imaging system.<sup>27</sup> In their algorithm, the user first manually located and defined a region of interest (ROI) around each marker and determined the orientation of every cylindrical marker, and then a template matching algorithm was applied to the ROIs. The normalized cross correlation between the

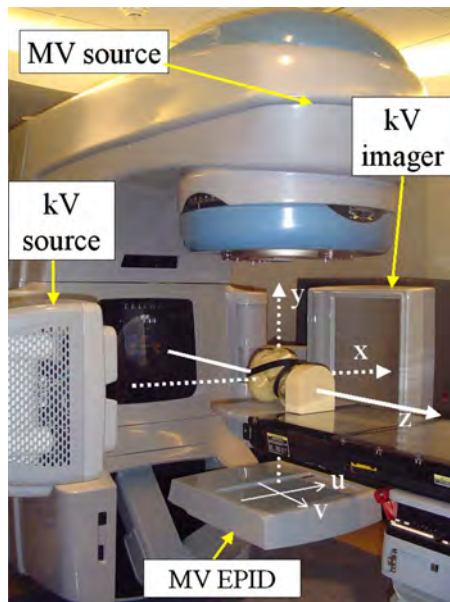


FIG. 1. Varian Trilogy with kV and MV imagers in extended positions. The system's frame of reference is denoted by arrows. A head phantom is located on the couch.

template and correlate pixels was calculated for every pixel and the highest cross correlation yielded the marker location. The detection failure rate for their method could be up to 12%.

As of yet, few works have presented algorithms suitable for tracking internal markers reliably using MV image data.<sup>18</sup> This is a consequence of the low inherent contrast between different materials in MV based images, making image based marker detection difficult.

This work proposes a novel pattern matching algorithm specifically designed to work with both kV and MV imaging systems. Unlike previous algorithms reported by Shirato *et al.* and Tang *et al.* where only the cross correlation is used for marker detection, this algorithm employs a criteria system based not on only the correlation score, but also the scaling factor and their combination. This is found to allow 100% successful marker detection rates, even on low contrast MV images. This algorithm is highly desirable since it can combine MV imaging with kV fluoroscopy imaging to locate real-time 3D tumor position during the actual radiotherapy process, as recently demonstrated by Wiersma *et al.*<sup>28</sup> Unlike other tracking techniques, which require two or more kV sources for 3D marker positioning,<sup>3,5,6,25–27,29</sup> this technique has the inherent benefit in that only one kV source is required for full 3D marker geometric information since the actual MV treatment beam is also used for positioning.

## II. MATERIALS AND METHOD

### II.A. Hardware setup

A Varian Trilogy (Varian Medical System, Palo Alto, CA) operating in the 6 MV photon mode was used for the study. Images of the MV beam were acquired by an aSi EPID

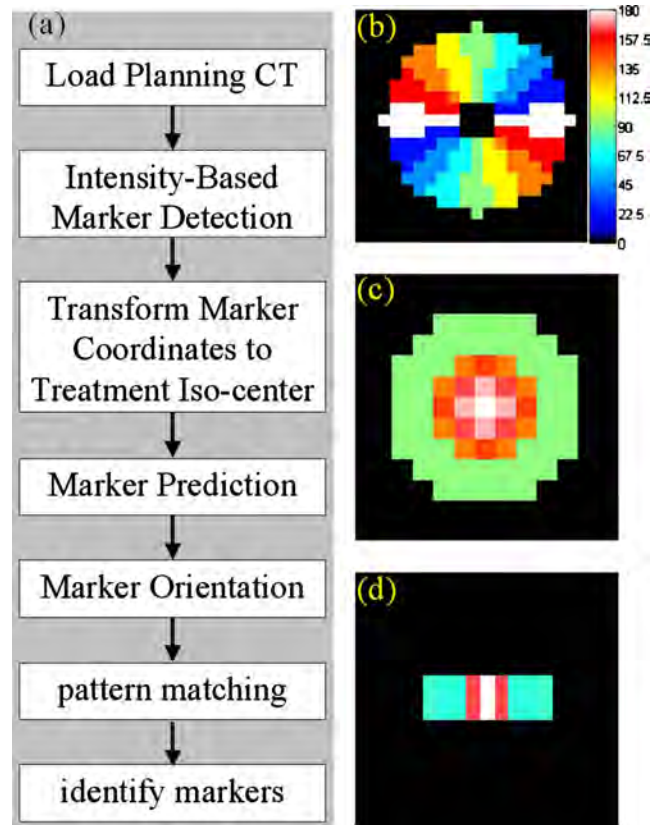


FIG. 2. (a) Flow chart algorithm computational path. (b) To the right is shown the eight-bin orientation segmentation filter, (c) spherical pattern, and (d) a cross section pattern for a vertical cylindrical marker.

(PortaVision aS-500, Varian Medical System, Palo Alto, CA) attached to the LINAC, as shown in Fig. 1. The kV imaging was accomplished using the onboard imaging system located perpendicular to the treatment beam (Fig. 1). The kV imaging system consisted of a 125 kV x-ray tube together with an aSi flat panel imager (PaxScan 4030CB, Varian Medical Systems, Salt Lake City, UT). Pixel sizes of the kV and MV detectors were 0.388 mm and 0.392 mm, respectively. Both detectors had a resolution of  $1024 \times 768$ , corresponding to an effective area of detection of approximately  $40 \text{ cm} \times 30 \text{ cm}$ . The source-to-axis distances (SAD) were set to 100 cm and source-to-imager distances (SID) were set to 150 cm for both MV and kV systems (Fig. 1).

The markers used were either stainless steel ball bearings (BB) or gold (Au) cylinders. The BB diameters varied from 1.57 mm to 4 mm, whereas the Au cylinders were 1.2 mm in diameter and 5 mm in length (North West Medical Physics Equipment, MED-TEC Company, Orange City, IA). Efficiency of the algorithm in segmenting markers from complex anatomical image background was tested using a head phantom (Fig. 1). The cylindrical fiducials were internally embedded into the phantom, whereas BBs were mounted externally on the phantom.

### II.B. CT based region-of-interest definition

Prior planning CT knowledge can provide valuable marker information that can be used to reduce the marker

search space. Reduction of search space in turn removes unnecessary image processing resulting in increased fiducial detection speeds. As displayed by the flow diagram in Fig. 2, a simple intensity based search for the markers was initially done on the planning CT. Due to the large CT numbers of the metallic markers relative to other anatomical structures, the markers were easily segmented from the image background. The displacement vector relating the CT isocenter to the treatment isocenter was then used to transform the marker CT coordinates to that of the treatment isocenter such that each marker was given a 3D position  $(x_B, y_B, z_B)$  relative to the machine isocenter. The expected projection location  $(u, v)$  of each marker on either the kV detector or the EPID can then be predicted by the following relationships

$$u = F \frac{\cos(\phi)x_B + \sin(\phi)y_B}{R - \sin(\phi)x_B + \cos(\phi)y_B}, \quad (1)$$

$$v = F \frac{z_B}{R - \sin(\phi)x_B + \cos(\phi)y_B}, \quad (2)$$

where  $\phi$  was the gantry angle,  $R$  was SAD, and  $F$  was SID. As seen in Fig. 1, the  $x$ -axis was in the lateral direction of patient couch, the  $y$ -axis was in the anterior-posterior direction, the  $z$ -axis was the superior-inferior direction, and the origin was the LINAC's isocenter. The coordinates of the imagers were defined in the  $(u, v)$  plane in Fig. 1.

Having located the expected positions of the marker projections, the search region was reduced to a small circular ROI around each marker projection center. Typically, a ROI with a radius of 75 pixels on the imager, or about 2 cm around the fiducial position, was found to be adequate in locating the marker. For markers located near each other, overlapping ROIs would be grouped together. The fiducial search was then performed group by group in order to avoid redundancy.

### II.C. Marker orientation

With a cylindrical marker of fixed length ( $l$ ) and width ( $w$ ), the unsymmetrical shape could lead to a host of different possible projection images depending on the marker's particular orientation relative to the source/imager setup. Parameters subject to variation were the marker's projection length and orientation (from  $0^\circ$ – $180^\circ$ ). The marker projection length might vary from “ $1.5 \times w$ ” (if the projection direction was along its longitudinal direction) to “ $1.5 \times 1$ ” (if the projection direction was perpendicular to its longitudinal di-

rection) with an amplification factor of 1.5 (=SID/SAD). To take into account the different possible orientations, the  $180^\circ$  rotation was divided into a number of bins, as shown in Fig. 2(b). As seen in the figure, each of the eight bins represented two possible opposite directions, such that each bin covered an angle of  $22.5^\circ$ . The center of this orientation filter was placed on each pixel in a ROI group, and all adjacent pixels from the center pixel were then grouped into eight bins corresponding to their particular angle. The average intensity of each bin was computed and the bin with the highest number was taken as the orientation of the center pixel. It should be noted that the orientation results carried no information for most of the pixels and it was only valid for pixels on a cylindrical object. The eight-bin pattern was chosen based on the limited pixel resolution of a projected marker. Due to the small marker size, a detected projection was composed of a limited number of pixels and therefore mosaic in nature (typically with a width of  $\sim 5$  pixels and a length of  $\sim 20$  pixels or less). Therefore, for small angles of rotation, only a few pixels would change. Using bin numbers greater than eight generally did not lead to a more accurate angle determination since now the pixel noise could be the deciding factor in a particular angle bin.

### II.D. Pattern matching algorithm

Different patterns were used for spherical and cylindrical markers. Due to rotational symmetry, a simple spherical marker pattern [Fig. 2(c)] was universally used for all BBs with the same physical diameter. For cylindrically shaped markers, a trapezoidal pattern [Fig. 2(d)] was used. The rationale behind this pattern was that even though a cylindrical marker projection might undergo a wide variety of rotational and length changes, the signal intensity distribution along the cross section of the cylinder projection remained constant. This cross section had a unique trapezoidlike pattern that was experimentally found to be dependent on the marker's width, but independent of projection length. Searching for these unique cross-sectional patterns along the orientation of every pixel in each ROI allowed for identification of fiducials.

Depending on the sought-after marker, either a spherical or cylindrical cross-sectional pattern  $\{p_{i,j}\}$  is used for the matching procedure. At each pixel location  $(x, y)$  within a ROI group, a comparison was made between the pattern and the surrounding pixels ( $\{f_{x+i,y+j}\}$ ). Two basic criteria were calculated: the square of the correlation coefficient  $R_{x,y}^2$  and the scaling factor  $H_{x,y}$

$$R_{x,y}^2 = \frac{\sum_{(i,j) \in \text{Pattern}} (f_{x+i,y+j} - \overline{f_{x,y}})(p_{i,j} - \overline{p})}{\sqrt{\sum_{(i,j) \in \text{Pattern}} (f_{x+i,y+j} - \overline{f_{x,y}})^2} \cdot \sqrt{\sum_{(i,j) \in \text{Pattern}} (p_{i,j} - \overline{p})^2}}, \quad (3)$$

$$H_{x,y} = \frac{\sum_{(i,j) \in \text{Pattern}} (f_{x+i,y+j} - \overline{f_{x,y}})(p_{i,j} - \overline{p})}{\sum_{(i,j) \in \text{Pattern}} (p_{i,j} - \overline{p})^2}, \quad (4)$$

where  $\overline{f_{x,y}}$  was the average intensity of the pattern region around pixel  $(x,y)$  and  $\overline{p}$  was the average intensity of the pattern distribution as given by

$$\overline{f_{x,y}} = \frac{1}{N} \sum_{(i,j) \in \text{Pattern}} f_{x+i,y+j}, \quad (5)$$

$$\overline{p} = \frac{1}{N} \sum_{(i,j) \in \text{Pattern}} p_{i,j}, \quad (6)$$

with  $N$  being the total pixel number of the pattern. The square of the coefficient of correlation ( $R^2$ ) for a linear regression could vary from 0 (no correlation) to 1 (perfect correlation). The scaling factor  $H$  indicated the relative intensity of the object compared to the background. As an example, in an ideal case, the image was scaled from the pattern after a background shift,  $f_{x+i,y+j} = k \cdot p_{i,j} + b$ , where  $k$  and  $b$  were constants. The pattern matching result would be  $R_{xy}^2 = 1$  and  $H_{x,y} = k$ .

Because the cylindrical cross sectional pattern is unable to determine correct marker lengths, it was necessary to group adjacent qualified cross sections and reconstruct their overall lengths. If the calculated length was found to be longer than the maximum projection length, the feature would be rejected. Here the maximum projection length was defined by multiplying the actual physical marker length by the imager magnification factor ( $=1.5$ ) plus a reasonable margin.

### II.E. Marker identification

With multiple markers it was easy to confuse the individual marker labeling for kV or MV projections at different gantry angles. The simplest case was when only one marker exists in each ROI group. From Eqs. (1) and (2) there was a direct correlation of the ROI group to a specific marker. In the case of multiple markers existing in the same ROI group, the detected marker positions in this ROI group were correlated to the planning CT markers corresponding to this ROI group, while indexing was based on the shortest distances between detected and predicted marker projections by using Eqs. (1) and (2). At certain gantry angles, it was possible that two or more markers may be projected on the same  $(u,v)$  location. In this case the number of detected markers in the ROI group would be fewer than the number of expected markers, indicating projection overlapping. This was resolved by comparing the measured to the predicted projections. If one or more of the projections was found missing, but was calculated to be in close proximity to another marker, this projection would be double counted.

### II.F. Experimental validation and patient data analysis

To evaluate the algorithm's efficiency when markers overlap or near different anatomical structures, a  $360^\circ$  gantry rotation was performed around a head phantom. Images were acquired every  $0.56^\circ$  for the kV imager ( $\sim 640$  images in total) and every  $10^\circ$  with the MV imager (36 images in total). Having obtained the projection locations for each marker, 3D spatial information could be calculated by using

projections at different gantry angles together with Eqs. (1) and (2). Particularly, the results from pairs of MV and kV projections were calculated.

As a preliminary test, this algorithm was also applied to actual patient images previously acquired for patient setup by onboard MV EPID. Five prostate patients with implanted cylindrical fiducial markers were treated in the past two years. Every patient had two or three fiducials (with a diameter of 1.2 mm and a length of 3 mm) implanted. They were treated on a conventional LINAC with MV EPID only. A total of 196 MV projection images were acquired for patient setup at anterior/posterior (AP) and lateral (LAT) directions before every treatment fraction. After all images were analyzed, the 3D spatial positions were calculated from every pair of AP and LAT images based on Eqs. (1) and (2).

An in-house software (C language) was specified to analyze projection images and obtain fiducial positions. All calculations were performed on a Dell Precision 470 workstation (3.4 GHz Xeon CPU and 4 GB RAM).

## III. RESULTS

As a demonstration of the orientation and cross-sectional pattern matching, a MV image of a head phantom with five embedded cylindrical markers was examined [Fig. 3(a)]. For a selected marker enlarged in Fig. 3(b), the eight-bin orientations are shown in Fig. 3(c). As can be seen, for pixels located around the fiducial, the  $\sim 45^\circ$  angle was favored, corresponding to the actual projection orientation. Having determined the orientation, a  $90^\circ$  rotation was made and the marker's cross section was segmented from the image back-

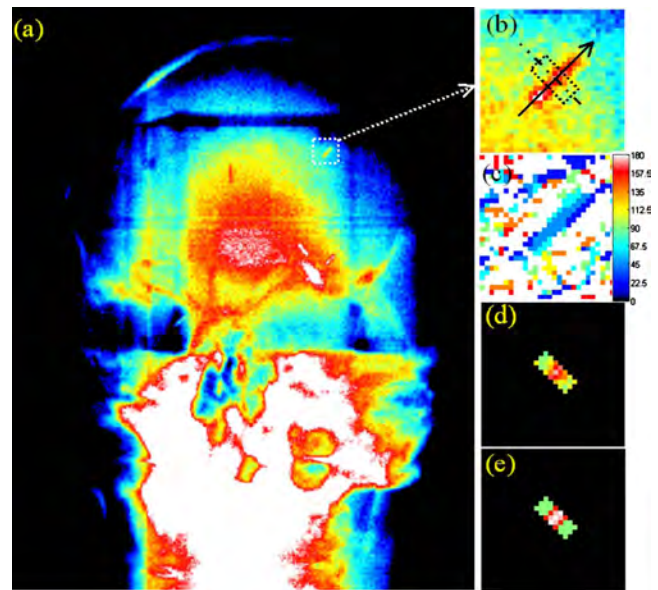


FIG. 3. (a) MV image of a head phantom with embedded Au cylindrical fiducial. (b) On the right shows magnified image of the selected marker displaying orientation and cross section (dotted line). (c) Orientation map with pixel intensity corresponding to adjacent intensity orientation for the selected marker. (d) Segmented cross-section. (e) Application of the cross-section pattern.

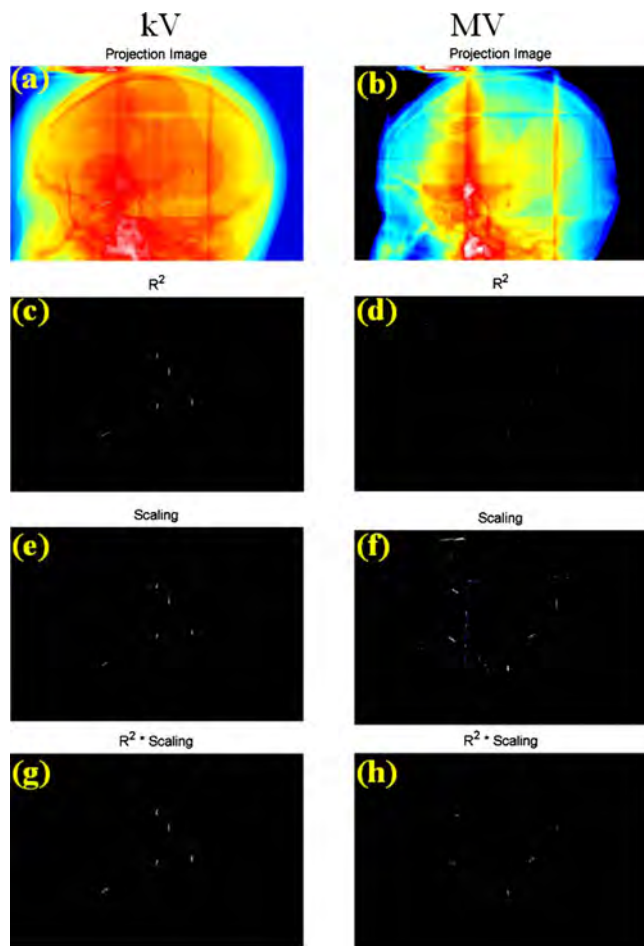


FIG. 4. Side-by-side kV (left column)/MV (right column) comparison of marker detection for five gold markers embedded in a head phantom. (a) and (b) Projection image and the predicted BB ROIs were highlighted, (c) and (d)  $R^2$  results (threshold applied), (e) and (f) scaling factors (threshold applied), and (g) and (h) searching index =  $R^2 \cdot$  scaling factor.

ground [Fig. 3(d)]. Then the cross-sectional pattern at  $45^\circ$  orientation [Fig. 3(e)] was applied to calculate  $R^2_{x,y}$  and  $H_{x,y}$ .

Figure 4 is a side-by-side comparison of the kV and MV detection process for five cylindrical Au markers embedded in a head phantom. The kV and MV images were acquired at a MV gantry angle of  $220^\circ$ . It should be noted that the on-board kV x-ray source is always rotated  $90^\circ$  relative to the MV source (Fig. 1). Application of the algorithm uses prior planning CT information to first define the ROI for each fiducial, as shown by the circular highlighted regions in Figs. 4(a) and 4(b). After ROIs were defined and grouped, orien-

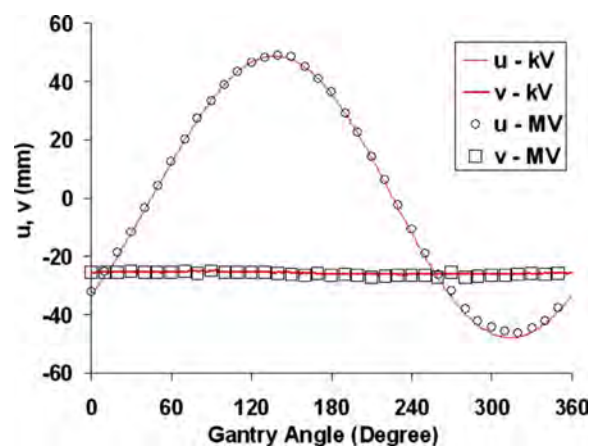


FIG. 5. Projection locations of one cylindrical fiducial on kV and MV images as functions of kV and MV gantry angles, respectively.

tation and pattern matching were applied to each ROI group and resulted in only image data that conformed to the cross-sectional pattern [Figs. 4(c)–4(f)]. The scaling of the ROIs led to greater background image segmentation for the kV case [Fig. 4(e)] over the MV case [Fig. 4(f)]. The product of the scaling factor  $H$  and the correlation  $R^2$  led to complete segmentation of the markers, as displayed in Figs. 4(g) and 4(h). In this case a threshold of 0.6 and 0.006 for  $R^2$  and  $H$ , respectively, were determined by previous trials and used through all our analyses.

Both kV and MV projections were analyzed using our detection algorithm, where it was found that all five markers were correctly detected for every kV and MV projection. Figure 5 plots the  $(u, v)$  coordinates on both the kV and MV detectors for one of the markers. Spatial positions of every marker were calculated for all MV projection images with their corresponding kV partner images gathered over the  $360^\circ$  gantry rotation. Table I summarizes these results, where it can be seen that the standard deviation of the location is better 0.5 mm and the errors are within 1 mm.

All patient images were analyzed similarly. In all cases the detection success rate was 100%. Figure 6 displays AP (left column) and LAT (right column) images of three markers embedded in a prostate. Three-dimensional positions of markers were calculated from pairs of AP and LAT projections. Figure 7 shows a fiducial marker's various 3D positions for 14 fractions. It should be noted that those images were taken at the beginning of patient setup and these positions were not yet the treatment position.

TABLE I. Variation of FM 3D positions calculated from MV/kV pair projections at 36 different gantry angles.

	FM #1			FM #2			FM #3			FM #4			FM #5		
	x	y	z	x	y	z	x	y	z	x	y	z	x	y	z
Mean	-22.9	22.3	-17.2	20.7	24.1	0.0	2.5	-31.9	2.5	-17.3	-32.7	22.7	19.5	22.8	30.4
Max-Mean	0.7	0.7	0.3	0.4	0.6	0.4	0.5	0.6	0.3	0.6	0.7	0.3	0.5	0.6	0.6
Min-Mean	-0.6	-0.7	-0.3	-0.7	-0.6	-0.3	-1.0	-0.6	-0.3	-0.8	-0.8	-0.4	-0.7	-0.9	-0.4
Standard Dev	0.4	0.4	0.2	0.3	0.4	0.2	0.4	0.4	0.2	0.4	0.4	0.2	0.3	0.4	0.2

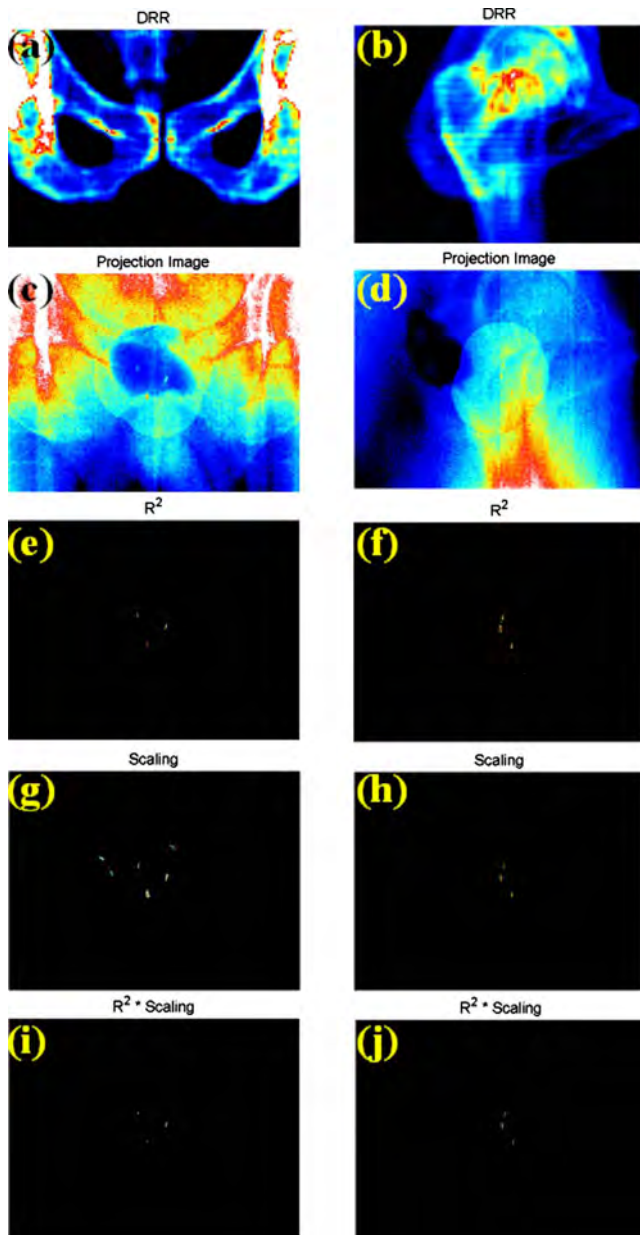


FIG. 6. Analyzing five cylindrical fiducials in a prostate patient MV image at AP (left column) and LAT (right column) directions. (a) and (b) DRR images, (c) and (d) Projection image and the predicted BB ROIs were highlighted, (e) and (f)  $R^2$  results (threshold applied), (g) and (h) scaling factors (threshold applied), and (i) and (j) searching index= $R^2 \cdot$  scaling factor.

In the case for symmetrical markers such as BBs, the algorithm can be easily modified by using the spherical pattern, as shown in Fig. 2(c). This detection is more simplistic compared to cylindrical marker detection since the BB projection image is independent of the BB's orientation. More than 2000 combined kV and MV projection images were made of four spherical BB markers (Fig. 8). For all images the algorithm was able to successfully detect the markers.

#### IV. DISCUSSION

The continued advancement of medical imaging technology is reaching the stage where procurement of high reso-

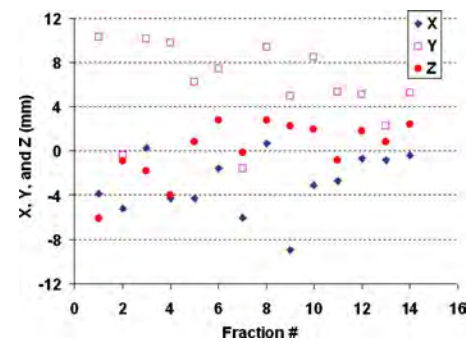


FIG. 7. 3D spatial position of a fiducial in a prostate patient before treatment setup at 14 treatment fractions.

lution anatomical images can be acquired rapidly and with low diagnostic dosages. In addition, utilizing the actual MV treatment beam for imaging has the potential to further reduce diagnostic doses. These various imaging modalities pave the way for real-time IGRT. For the tested projection images, the algorithm demonstrates high successful detection rates together with near real-time speeds. As seen in Figs. 4, 6, and 8, reliance on only  $R^2$  can lead to false positive marker

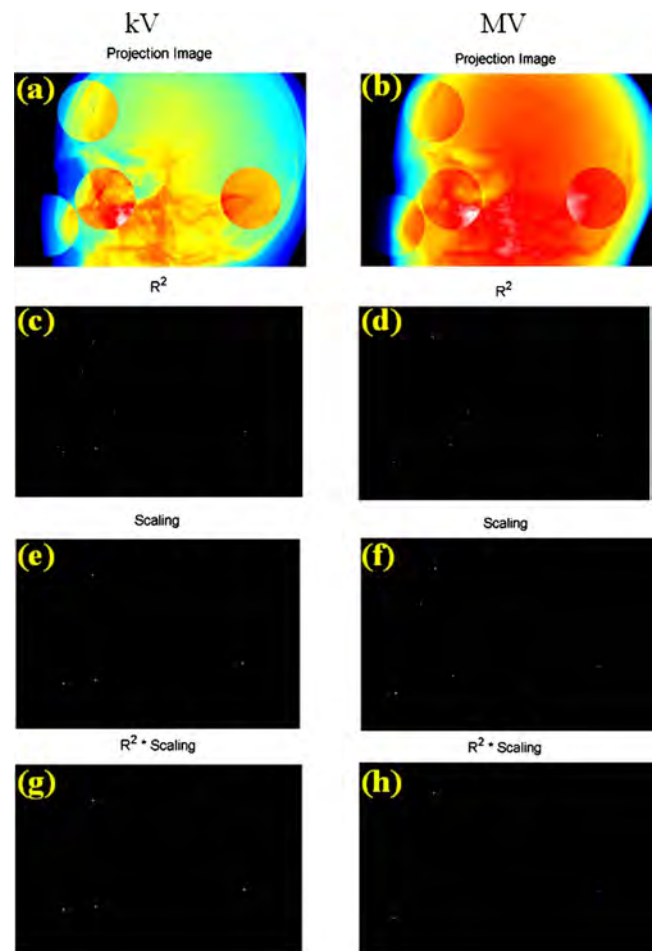


FIG. 8. Analyzing four BBs on kV (left column) and MV (right column) images. (a) and (b) Projection image and the predicted BB ROIs were highlighted, (c) and (d)  $R^2$  results (threshold applied), (e) and (f) scaling factors (threshold applied), and (g) and (h) searching index= $R^2 \cdot$  scaling factor.

detection, especially for MV based projections. The combination of these two criteria resulted in 100% success detection rates for all 3500 images kV or MV projections analyzed. It is important to emphasize that multiple markers could be successfully tracked on MV images.

Fast marker detection is a crucial component of real-time image based tracking. This algorithm quickens the search process in two aspects. First, the orientation and cross-sectional pattern matching for cylindrical markers simplifies the problem due to cylindrical orientation and projection length, which would otherwise require a large number of patterns to be tested.<sup>27</sup> Secondly, the search space is significantly reduced by incorporating prior CT marker location knowledge. For a typical  $1024 \times 768$  image with five cylindrical markers, the processing time is reduced from  $\sim 1$  s to 0.1 s upon incorporating ROI selection. For fewer markers this time would be reduced even further. Generally, spherical marker detection requires approximately half the computational time as compared to detecting the same number of cylindrical markers. In addition, this process is completely automated and does not need any manual location initializations, which is another asset.

Currently, the EPID imager used in this study is hardware limited to a maximum frames-per-sec (fps) rate of  $\sim 7.5$  fps. It is, however, envisioned that as future faster kV and MV detectors become available, the algorithm's detection time can be further reduced. In general, the maximum clinically seen velocity of a tumor is  $\sim 4.0$  cm/s (respiratory based). With the current 7.5 fps imaging speed this would correspond to a between frame marker travel distance of  $\sim 0.5$  cm. This distance is small in comparison to the 2 cm in radius ROI used for detection. To increase computational speeds it is beneficial to reduce the search space defined by the ROI. This could be accomplished by recalculating a new 0.5 cm in radius ROI for each new frame analyzed. The location of this ROI would be centered on the marker's location in the previous frame, thus ensuring that the marker is located within the ROI.

As demonstrated in Fig. 5, the orthogonal location of the kV imager relative the MV imager allows for calculation of the 3D position of the markers from the isocenter. Although this current work consists of retrospective analysis, it is expected that this tracking algorithm can provide real-time 3D tracking in such a system. This is especially convenient on treatment systems pre-equipped with kV and MV onboard imaging equipment as it should only require minimal hardware changes, thus being a cost effective solution for implementing IGRT.

## V. CONCLUSION

Fast and reliable localization of implanted metallic fiducials of various shapes has been an important yet challenging problem in kV stereoscopic image guided RT. This problem is further aggravated by much reduced image contrast when MV beam imaging is involved for therapeutic guidance. A new pattern matching algorithm has been proposed to track multiple spherical or cylindrical fiducial markers on both

MV and kV projection images. A completely automated detection, 100% detection efficiency, and fast detection speed (10 frames/sec) enable tracking tumor motion in real-time on a LINAC with both kV and MV imaging systems. This algorithm makes it a suitable candidate for future image-guided radiosurgical procedures.

## ACKNOWLEDGMENTS

This work was supported in part by grants from the Department of Defense (Grant No. PC040282), the National Cancer Institute (Grant No. 1R01 CA104205), and the Komen Breast Cancer Foundation (Grant No. BCTR0504071).

<sup>a)</sup> Author to whom all correspondence should be addressed. Electronic mail: lei@reyes.stanford.edu; Telephone: 650-498-7896; Fax: 650-498-4015.

<sup>1</sup>IMRT Collaborative Working Group, "Intensity-modulated radiotherapy: Current status and issues of interest," *Int. J. Radiat. Oncol., Biol., Phys.* **51**, 880–914 (2001).

<sup>2</sup>J. M. Galvin *et al.*, "Implementing IMRT in clinical practice: A joint document of the American Society for Therapeutic Radiology and Oncology and the American Association of Physicists in Medicine," *Int. J. Radiat. Oncol., Biol., Phys.* **58**, 1616–1634 (2004).

<sup>3</sup>K. Kitamura *et al.*, "Three-dimensional intrafractional movement of prostate measured during real-time tumor-tracking radiotherapy in supine and prone treatment positions," *Int. J. Radiat. Oncol., Biol., Phys.* **53**, 1117–1123 (2002).

<sup>4</sup>J. M. Crook *et al.*, "Prostate motion during standard radiotherapy as assessed by fiducial markers," *Radiother. Oncol.* **37**, 35–42 (1995).

<sup>5</sup>R. I. Berbeco *et al.*, "Residual motion of lung tumours in end-of-inhale respiratory gated radiotherapy based on external surrogates," *Med. Phys.* **33**, 4149–4156 (2006).

<sup>6</sup>Y. Seppenwoolde *et al.*, "Precise and real-time measurement of 3D tumor motion in lung due to breathing and heartbeat, measured during radiotherapy," *Int. J. Radiat. Oncol., Biol., Phys.* **53**, 822–834 (2002).

<sup>7</sup>Y. Xie *et al.*, "Intrafraction motion of the prostate in cyberknife hypofractionated radiotherapy," *Int. J. Radiat. Oncol., Biol., Phys.* (accepted).

<sup>8</sup>K. L. Zhao *et al.*, "Evaluation of respiratory-induced target motion for esophageal tumors at the gastroesophageal junction," *Radiother. Oncol.* **84**, 283–289 (2007).

<sup>9</sup>H. Shirato *et al.*, "Speed and amplitude of lung tumor motion precisely detected in four-dimensional setup and in real-time tumor-tracking radiotherapy," *Int. J. Radiat. Oncol., Biol., Phys.* **64**, 1229–1236 (2006).

<sup>10</sup>L. Xing *et al.*, "Overview of image-guided radiation therapy," *Med. Dosim.* **31**, 91–112 (2006).

<sup>11</sup>M. J. Murphy, "Tracking moving organs in real time," *Semin. Radiat. Oncol.* **14**, 91–100 (2004).

<sup>12</sup>P. C. Chi *et al.*, "Relation of external surface to internal tumor motion studied with cine CT," *Med. Phys.* **33**, 3116–3123 (2006).

<sup>13</sup>H. Shirato *et al.*, "Real-time tumour-tracking radiotherapy," *Lancet* **353**, 1331–1332 (1999).

<sup>14</sup>P. Kupelian *et al.*, "Multi-institutional clinical experience with the Calypso System in localization and continuous, real-time monitoring of the prostate gland during external radiotherapy," *Int. J. Radiat. Oncol., Biol., Phys.* **67**, 1088–1098 (2007).

<sup>15</sup>A. L. Boyer *et al.*, "A review of electronic portal imaging devices (EPIDs)," *Med. Phys.* **19**, 1–16 (1992).

<sup>16</sup>L. Dong *et al.*, "Verification of radiosurgery target point alignment with an electronic portal imaging device (EPID)," *Med. Phys.* **24**(2), 263–267 (1997).

<sup>17</sup>M. G. Herman *et al.*, "Technical aspects of daily online positioning of the prostate for three-dimensional conformal radiotherapy using an electronic portal imaging device," *Int. J. Radiat. Oncol., Biol., Phys.* **57**, 1131–1140 (2003).

<sup>18</sup>P. J. Keall *et al.*, "On the use of EPID-based implanted marker tracking for 4D radiotherapy," *Med. Phys.* **31**, 3492–3499 (2004).

<sup>19</sup>H. Dehnad *et al.*, "Clinical feasibility study for the use of implanted gold seeds in the prostate as reliable positioning markers during megavoltage

- irradiation," *Radiother. Oncol.* **67**, 295–302 (2003).
- <sup>20</sup>A. Nederveen, J. Lagendijk, and P. Hofman, "Detection of fiducial gold markers for automatic on-line megavoltage position verification using a marker extraction kernel (MEK)," *Int. J. Radiat. Oncol., Biol., Phys.* **47**, 1435–1442 (2000).
- <sup>21</sup>A. J. Nederveen, J. J. Lagendijk, and P. Hofman, "Feasibility of automatic marker detection with an a-Si flat-panel imager," *Phys. Med. Biol.* **46**, 1219–1230 (2001).
- <sup>22</sup>J. Pouliot *et al.*, "(Non)-migration of radiopaque markers used for on-line localization of the prostate with an electronic portal imaging device," *Int. J. Radiat. Oncol., Biol., Phys.* **56**, 862–866 (2003).
- <sup>23</sup>D. C. Schiffner *et al.*, "Daily electronic portal imaging of implanted gold seed fiducials in patients undergoing radiotherapy after radical prostatectomy," *Int. J. Radiat. Oncol., Biol., Phys.* **67**, 610–619 (2007).
- <sup>24</sup>L. Smith *et al.*, "Automatic detection of fiducial markers in fluoroscopy images for on-line calibration," *Med. Phys.* **32**, 1521–1523 (2005).
- <sup>25</sup>H. Shirato *et al.*, "Physical aspects of a real-time tumor-tracking system for gated radiotherapy," *Int. J. Radiat. Oncol., Biol., Phys.* **48**, 1187–1195 (2000).
- <sup>26</sup>T. R. Willoughby *et al.*, "Evaluation of an infrared camera and x-ray system using implanted fiducials in patients with lung tumors for gated radiation therapy," *Int. J. Radiat. Oncol., Biol., Phys.* **66**, 568–575 (2006).
- <sup>27</sup>X. Tang, G. C. Sharp, and S. B. Jiang, "Fluoroscopic tracking of multiple implanted fiducial markers using multiple object tracking," *Phys. Med. Biol.* **52**, 4081–4098 (2007).
- <sup>28</sup>R. D. Wiersma, W. Mao, and L. Xing, "Combined kV and MV imaging for real-time tracking of implanted fiducial markers," *Med. Phys.* **35**, 1191–1198 (2008).
- <sup>29</sup>K. Kitamura *et al.*, "Tumor location, cirrhosis, and surgical history contribute to tumor movement in the liver, as measured during stereotactic irradiation using a real-time tumor-tracking radiotherapy system," *Int. J. Radiat. Oncol., Biol., Phys.* **56**, 221–228 (2003).

# Combined kV and MV imaging for real-time tracking of implanted fiducial markers<sup>a)</sup>

R. D. Wiersma,<sup>b)</sup> Weihua Mao, and L. Xing

*Department of Radiation Oncology, Stanford University School of Medicine, Stanford, California 94305-5847*

(Received 29 August 2007; revised 15 January 2008; accepted for publication 17 January 2008; published 6 March 2008)

In the presence of intrafraction organ motion, target localization uncertainty can greatly hamper the advantage of highly conformal dose techniques such as intensity modulated radiation therapy (IMRT). To minimize the adverse dosimetric effect caused by tumor motion, a real-time knowledge of the tumor position is required throughout the beam delivery process. The recent integration of onboard kV diagnostic imaging together with MV electronic portal imaging devices on linear accelerators can allow for real-time three-dimensional (3D) tumor position monitoring during a treatment delivery. The aim of this study is to demonstrate a near real-time 3D internal fiducial tracking system based on the combined use of kV and MV imaging. A commercially available radiotherapy system equipped with both kV and MV imaging systems was used in this work. A hardware video frame grabber was used to capture both kV and MV video streams simultaneously through independent video channels at 30 frames per second. The fiducial locations were extracted from the kV and MV images using a software tool. The geometric tracking capabilities of the system were evaluated using a pelvic phantom with embedded fiducials placed on a moveable stage. The maximum tracking speed of the kV/MV system is approximately 9 Hz, which is primarily limited by the frame rate of the MV imager. The geometric accuracy of the system is found to be on the order of less than 1 mm in all three spatial dimensions. The technique requires minimal hardware modification and is potentially useful for image-guided radiation therapy systems. © 2008 American Association of Physicists in Medicine. [DOI: [10.1118/1.2842072](https://doi.org/10.1118/1.2842072)]

Key words: EPID, OBI, marker tracking, 4D radiotherapy

## I. INTRODUCTION

In radiation therapy (RT), delivering a highly conformal dose distribution to a static three-dimensional (3D) target is largely solved by techniques such as intensity modulated radiation therapy (IMRT).<sup>1,2</sup> What remains problematic is how to take into account the dynamic nature of human anatomy, where both inter- and intrafraction organ motion can limit target dose conformity<sup>3,4</sup> and therefore local tumor control.<sup>5</sup> Tumor motion can be addressed by increasing the planning target volume (PTV) to include the entire range of motion of the target, however, usually at the cost of irradiating more healthy tissue. Other techniques used to address tumor motion are direct patient intervention through breath-hold techniques<sup>6</sup> or the delivery of radiation only when the target is in a known geometric location by the use of gating.<sup>7-10</sup> These techniques transform the problem of targeting a moving tumor into a more easily manageable static treatment case. Ideally, one would like to deliver highly conformal radiation, as in a static IMRT case, to a moving target without beam interruption or patient intervention. Promising candidates in this direction include tumor tracking by moving the radiation source itself<sup>11-13</sup> or the beam defining multileaf collimator.<sup>14-16</sup>

To successfully guide a gating or tracking RT delivery system, real-time knowledge of the target geometric location is necessary. Several methods of obtaining the real-time tumor position are available and these can be categorized as

being either indirect (surrogate-based) or direct (fiducial/image) in nature. In general, indirect tumor location methods, such as external skin marker tracking<sup>10,17,18</sup> or breath monitoring techniques,<sup>19</sup> rely on the correlation between external body parameters and the tumor. In reality, the relationship between external parameters and internal organ motion is complex and a large uncertainty may be present in predicting the tumor location based on external signals.<sup>20,21</sup> The unreliable correlation represents one of the weakest links in the quality chain of respiration-gated and four-dimensional (4D) RT. A direct tumor position measurement is highly desirable for therapeutic guidance. In the last decade, a number of direct real-time 3D tumor tracking methods have been implemented, primarily using fluoroscopy<sup>22,23</sup> or magnetic field localization.<sup>24</sup> The feasibility of using electronic portal imaging devices (EPID) for real-time tumor targeting has also been explored.<sup>25</sup> However, since only a single in-line MV beam was employed, this approach suffers from insufficient information to completely define the 3D coordinates of the embedded fiducials.

With the emergence of linear accelerators (LINACs) equipped with both onboard kV imaging and EPID, the potential exists to obtain the tumor position in real-time during the radiation delivery process through the combined use of the MV treatment beam and kV projection images. In this work we report our implementation of such a real-time 3D tracking system and demonstrate that a spatial accuracy of

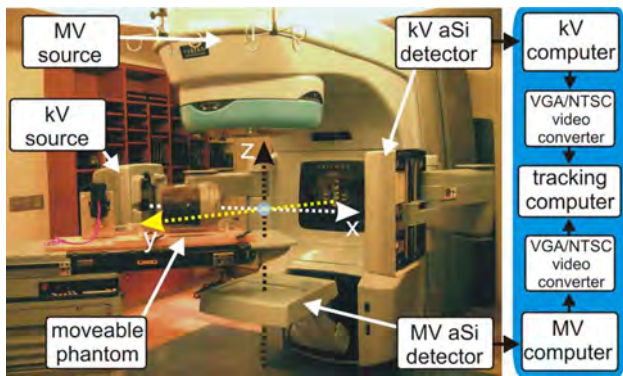


FIG. 1. Varian Trilogy with kV and MV imagers in extended positions. System frame of reference is denoted by dashed arrows. A pelvic phantom, placed on a movable stage, is located on the couch. To the right is displayed the process path used for image acquisition.

$<1$  mm is achievable in tracking fiducials using the proposed technique. The method takes advantage of the kV/MV imaging devices already mounted on commercially available treatment machines, thus providing an easily implemented method for monitoring intrafractional tumor motion. Since projection data containing two-dimensional target information is obtained using the actual treatment beam, the proposed method only requires the use of one kV source in gaining the other spatial dimension necessary for full 3D target localization. Compared to other fluoroscopic tracking systems, which require the use of two or more additional kV x-ray imaging systems, the technique may offer potential radiation sparing to the patient and overall system cost reductions. With the use of real-time spatial trajectory information of fiducials in the future, it is hoped that uncertainties in intrafraction target localization can be greatly reduced, thus ensuring a more accurate delivery of the planned conformal dose distribution.

## II. MATERIALS AND METHOD

### II.A. Hardware setup

A Varian Trilogy<sup>TM</sup> system (Varian Medical Systems, Palo Alto, CA) operating in the 6 MV photon mode was used for this study. Images of the MV beam were acquired using an aSi EPID (Portal Vision MV AS-500, Varian Medical Systems, Palo Alto, CA) attached to the LINAC as shown in Fig. 1. The kV imaging was obtained by using the onboard kV imaging system located perpendicular to the treatment beam (Fig. 1). The device consists of a 125 kV x-ray tube together with an aSi flat panel imager (PaxScan 4030CB, Varian Medical Systems, Salt Lake City, UT). Both kV and MV detectors have a pixel width of 0.392 mm and a maximum resolution of  $1024 \times 768$ , corresponding to a  $40 \text{ cm} \times 30 \text{ cm}$  effective area of detection. The maximal frames per second (fps) obtainable from the kV and MV detectors in this work are 15 and 9 Hz, respectively. The kV and MV source detector distances (SDD) are set to 180 and 150 cm, respectively, though in principle this can be varied to a wide variety of distances as allowed by the robotic arms (Fig. 1).

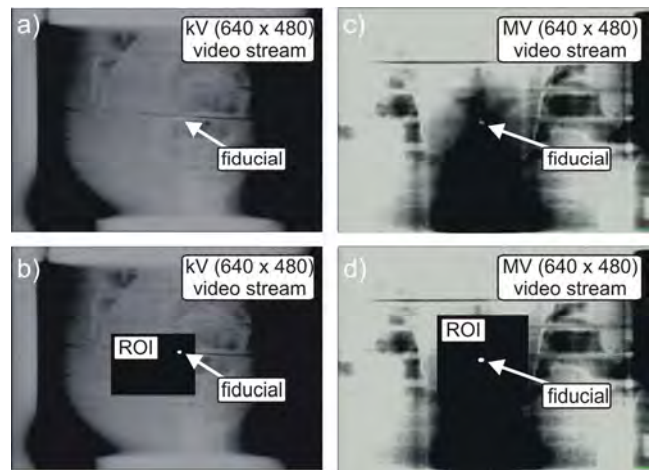


FIG. 2. Displayed snap shots of a BB fiducial in a pelvic phantom for the kV and MV video streams before [(a) and (c)] and after [(b) and (d)] applying the fiducial detection algorithm on the selected ROI.

### II.B. kV/MV image acquisition and marker localization

A dedicated image processing PC was used to process and analyze both kV and MV video streams simultaneously as detailed in Fig. 1. Two channels of a four channel PCI video grabber (ProVideo 149P, ProVideo Co., Taipei Hsien, Taiwan) were used to grab the kV and MV video streams at 30 fps per channel with a resolution of  $640 \times 480$ . A freely available third party software program,<sup>26</sup> designed for machine vision prototyping, was used to interface with the capture card and analyze the video. The software contains a large database of common video processing filter modules and allows the user to apply, or remove, various combinations of filters to the video pipeline in real time. In addition, the program allows customized script filters to be created. The following sequence of filters were found to be adequate in detecting the fiducial; (1) a region-of-interest (ROI) filter, (2) pseudocolor filter to convert the grayscale captured image into a color image, (3) a color filter to extract the fiducial color value, (4) a mean filter to average pixel values to reduce noise, (5) a detect blob filter to segment the fiducial from the background, (6) a center-of-mass filter to calculate the central pixel location of the blob, and (7) an in-house written script filter to convert the pixel location to a real-space location from system isocenter.

The ROI filter requires the operator to manually enter pixel locations to define a rectangle encompassing the fiducial's range of motion (Fig. 2). Through a process of visual inspection and identification, the operator must initially define the ROI for both kV and MV video streams. Use of the ROI filter has the benefit of removing unnecessary background pixel information from the image-processing pipeline, thereby increasing computational speed. In the event of a large change in fiducial motion (couch shift or phantom repositioning), the ROI may no longer encompass the entire range of motion of the fiducial, in this case the ROI must be redefined.

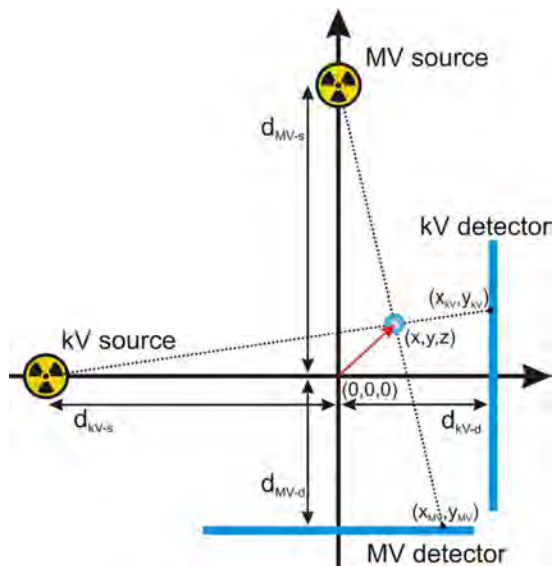


FIG. 3. Geometric sketch detailing variables used for calculation of a marker's  $(x, y, z)$  position from isocenter  $(0,0,0)$ . The  $xz$  plane is shown with the  $y$  axis pointing out of the page.

The pseudocolor filter converted the grayscale image to a spectrum of colors ranging from red to blue, with black corresponding to blue and white to red. Thus, metallic fiducials appeared reddish after application of the filter. This allowed for easy detection using a red color filter (step 3). It should be noted, that an intensity based fiducial segmentation can also be performed, however, in this study we found the pseudocolor followed by a color filter technique to be adequate.

The blob filter module was provided by the software package and allows identification of a cluster of pixels, or blob, based on its particular features. By providing features as the size and shape of blobs pertaining to fiducials, the blob filter is able to identify and segment the fiducial from the image even in the presence of a noisy background.

Having detected the fiducial's center-of-mass, the real-space  $(x, y, z)$  marker locations from system isocenter were calculated using the geometric relationships depicted in Fig. 3 and given by the following relations [Eqs. (1) and (4)]:

$$\frac{x_{MV}}{d_{MV-s} + d_{MV-d}} = \frac{x}{d_{MV-s} - z}, \quad (1)$$

$$\frac{y_{MV}}{d_{MV-s} + d_{MV-d}} = \frac{y}{d_{MV-s} - z}, \quad (2)$$

$$\frac{x_{kV}}{d_{kV-s} + d_{kV-d}} = \frac{z}{d_{kV-s} + x}, \quad (3)$$

$$\frac{y_{kV}}{d_{kV-s} + d_{kV-d}} = \frac{y}{d_{kV-s} + x}. \quad (4)$$

Here  $(x, y, z)$  corresponds to the marker's position from system isocenter where the isocenter is defined at 100 cm source axis distance (SAD) and the center of the MV beam. The kV

and MV photon source-to-isocenter distances are given by  $d_{kV-s}$  and  $d_{MV-s}$ , respectively. The isocenter to kV and MV detector distances are given by  $d_{kV-d}$  and  $d_{MV-d}$ , respectively. The algorithm also takes into account gantry angle ( $\theta$ ) by use of a rotational transform matrix equation to connect the systems frame of reference with that of the laboratory

$$\begin{bmatrix} \cos \theta & 0 & \sin \theta \\ 0 & 1 & 0 \\ -\sin \theta & 0 & \cos \theta \end{bmatrix} \begin{pmatrix} x \\ y \\ z \end{pmatrix} = \begin{pmatrix} x' \\ y' \\ z' \end{pmatrix}, \quad (5)$$

where  $(x', y', z')$  denotes the marker's coordinates from system isocenter in the laboratory's frame of reference.

Although the fiducial detection and localization algorithm lowers the processing speed to 15 fps due to processing time, the main bottleneck is found to be the  $\sim 9$  fps hardware limitation of the EPID *aSi* detector. Therefore, the maximum 3D fiducial tracking speed of the system is approximately 9 fps.

## II.C. kV and MV tracker calibration

Calibration of the tracking system was necessary in order to convert the detected location of the center-of-mass of the fiducial in the image frame to the real space coordinate of the fiducial in the laboratory frame of reference. The calibration technique used a single 3.0 mm diameter stainless steel ball bearing (BB) fixed near the end of a Styrofoam block-like phantom with a dimension of 600 mm  $\times$  200 mm  $\times$  23 mm. The end, not containing the BB, was rigidly mounted to a 3D displacement stage place on the couch, whereas, the other end, extended 500 mm over the couch toward the gantry. This setup allowed images of the BB containing little background artifacts due to removal of the couch from the kV and MV imagers' field of view. In addition, the low mass density of the Styrofoam support structure made it relatively transparent to kV and MV radiation, allowing easy detection of the fiducial. Using the manually operated displacement stage, the BB was moved in 3D space with a precision better than 0.5 mm. The calibration consisted of two parts: (1) defining the isocenter position in the laboratory frame of reference and (2) making known displacements of the BB from the isocenter. The LINAC's isocenter was used as the origin of the laboratory frame (Fig. 1). A mechanical front pointer assembly (Varian Medical System, Palo Alto, CA) was locked in the LINAC's collimator and a mechanical measurement rod was used to position the BB at system isocenter with a precision better than 1.0 mm. The BB's  $x, y$  pixel location was then detected using the kV and MV video streams and the pixel locations recorded. The BB was then shifted using the 3D stage to ten known static geometric locations and the resulting  $x, y$  pixel locations were recorded (Fig. 4). The theoretical BB displacements from isocenter were calculated using Eqs. (1)–(4) for each imager and plotted in Fig. 4. Linear fitting allowed extraction of the pixel sizes, which for the kV detector are  $x$  axis =  $0.860 \pm 0.01$  mm/pixel and  $y$  axis  $0.849 \pm 0.008$  mm/pixel, and for the MV detector are  $x$  axis =  $0.669 \pm 0.007$  mm/pixel and

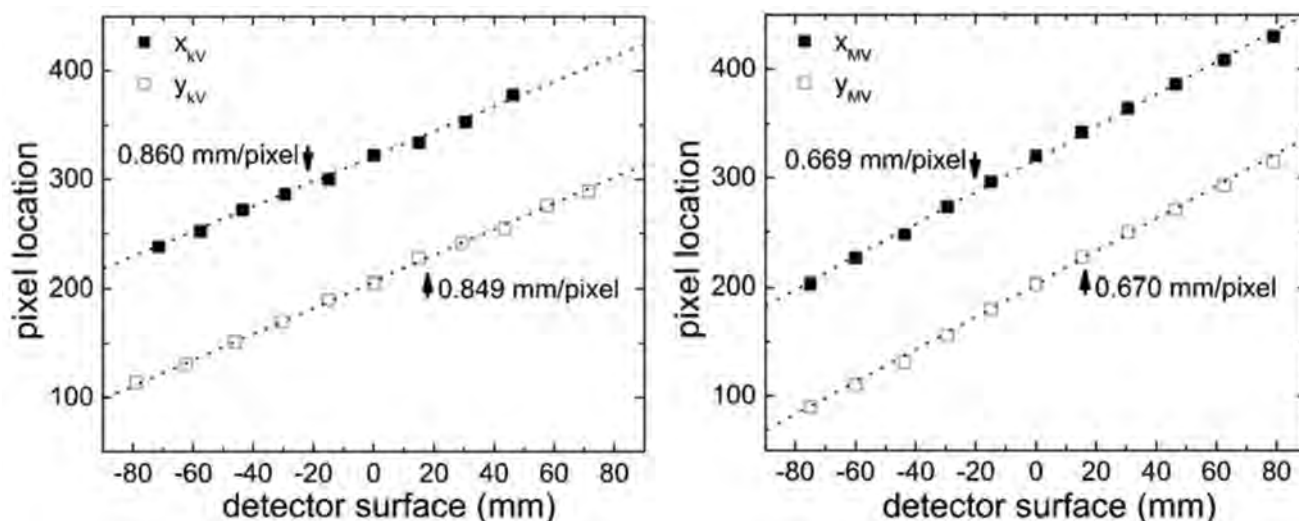


FIG. 4. Detected pixel location on the kV (left) and MV (right) detector surfaces for several well known displacements of a 3 mm diameter BB. Slope of linear fit (dotted line) allows calibration of pixel size.

y axis  $0.670 \pm 0.008$  mm/pixel. After calibration, the displacement vector from isocenter can be calculated for an arbitrary movement of the BB in 3D space.

Due to the weight of the gantry and imaging devices, gantry sag may happen during rotation, resulting in geographical inaccuracies. Therefore, at each new gantry angle investigated, the calibration procedure was repeated to get a calibration tuned to that specific gantry angle. It was necessary to perform calibration only one time for a specific gantry angle. Only in the event of changes to the system setup, as kV/MV imager realignment, was it necessary to repeat the tracker calibration. In general, this is similar to the geometric calibration done during the commissioning of a new machine, where the gantry angle specific calibration data is used for accurate imaging or cone beam reconstruction.

#### II.D. Quality and accuracy evaluation

To quantify the accuracy and precision of the tracking technique, an in-house built movable platform was used to move a pelvic phantom containing a stainless steel BB of 3 mm in diameter (Fig. 1). Both amplitude and period of the platform can be adjusted. In this study, the amplitude of oscillation was fixed to 20 mm along the y axis, whereas the period was varied to 1.8, 3.0, 3.4, and 5.0 s. The platform is supported by four high precision wheels on each of its four corners and is oscillated using an electronic variable speed gear motor connected via a rigid drive shaft. Four custom built wedges were placed underneath each of the stage's wheels, creating movement in the z direction with amplitude 7.5 mm. For a given sinusoidal wave driving the platform, the sinusoidal motion generated was verified, using an electronic caliper with 0.02 mm accuracy, to have a root mean square (RMS) deviation of no more than 0.2 mm from the theoretical value in both the y and z directions. To generate motion in the x axis, the platform was rotated by  $45^\circ$  with

respect to the y axis, as shown in Fig. 1. This enables the stage to move along both the x and y axis with an amplitude  $\sim 20/\sqrt{2}$  mm.

### III. RESULTS

Using the system setup in Fig. 1, the pelvic phantom was oscillated at a fixed period of 3.4 s. The tracked fiducial motion from isocenter is plotted in Fig. 5 along all x, y, and z spatial components as a function of time. As can be seen, the tracked fiducial location undergoes sinusoidal motion with a fixed amplitude and period along the three coordinates. The tracked motion agrees well with the known movement of the fiducial embedded in the pelvic phantom. The measured amplitudes in the x- and y-axis directions are approximately 13.6 and 14.2 mm, respectively. These values are very close to  $20/\sqrt{2}$  mm, as expected for a motion along  $45^\circ$ . As shown in Fig. 5, the theoretically sinusoidal function inputted in the motion platform (denoted by the solid curves) agrees well with the measured data points. Comparison of the expected and measured curves reveals RMS values of 0.86 and 0.55 mm for the x- and y-axis motion, respectively. The amplitude of fiducial movement along the z axis is measured to be 8.1 mm, which is also in close agreement with the actual 7.5 mm amplitude of the stage. Here the RMS is calculated to be 0.50 mm from the expected value. These measurements were done at a gantry angle of  $180^\circ$  and were repeated for different gantry angles of  $90^\circ$ ,  $135^\circ$ ,  $270^\circ$ , and  $360^\circ$ , in which similar results were obtained after applying Eq. (5).

The net magnitude of the fiducial away from system isocenter is plotted in Fig. 6. From the figure it is seen that the amplitude of displacement of the fiducial from isocenter is  $\sim 21.3$  mm, which agrees well with the calculated ground truth value of 21.4 mm. The mean square deviation of the measured from the expected values is found to be 0.63 mm.

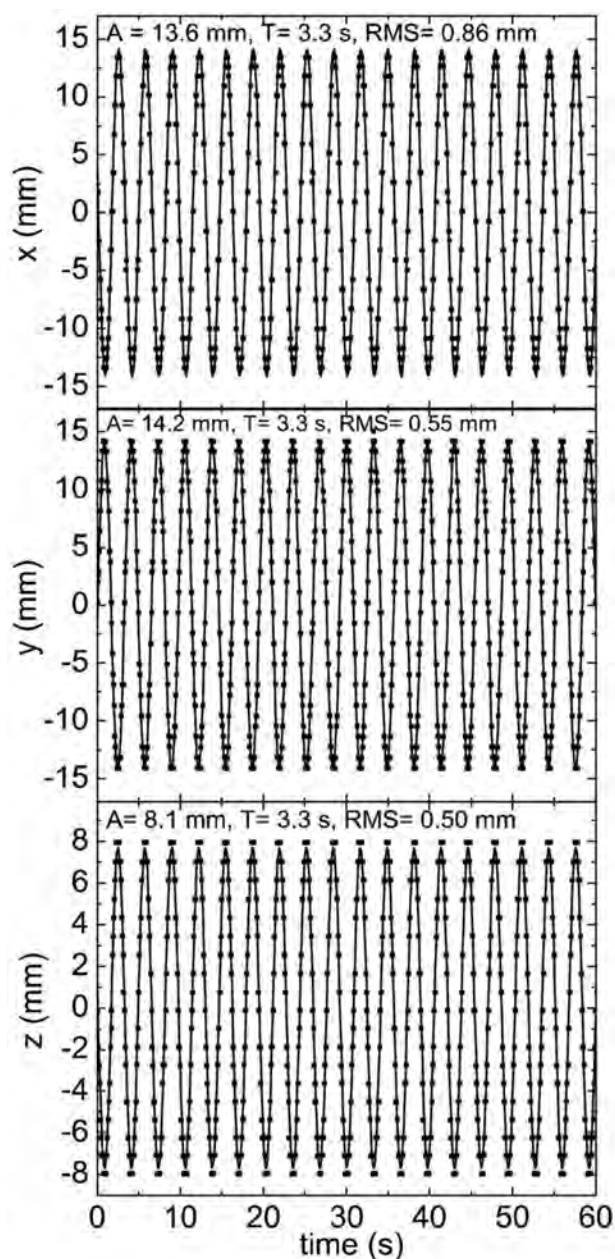


FIG. 5. Plot of real-time fiducial motion along  $x$ ,  $y$ ,  $z$  obtained using simultaneous kV/MV imaging. Motion is with respect to system isocenter. Solid curve is predicted motion. Deviation between predicted and experimental data points expressed as RMS.

Investigation of system tracking speed response was accomplished by varying the platform period of oscillation from 5.0 s to the lowest settable value of 1.8 s. The measured  $y$  displacement for different frequencies were compared to each other and also to the known values shown in Fig. 7. This comparison is possible due to the geometric setup, where both kV and MV detectors are able to detect motion along the  $y$  axis (Fig. 1).

Figure 8 is a plot of the measured  $y_{kV}$  and  $y_{MV}$  as a function of time. The larger amplitude of the kV trace in comparison with the MV trace relates to the kV detector being

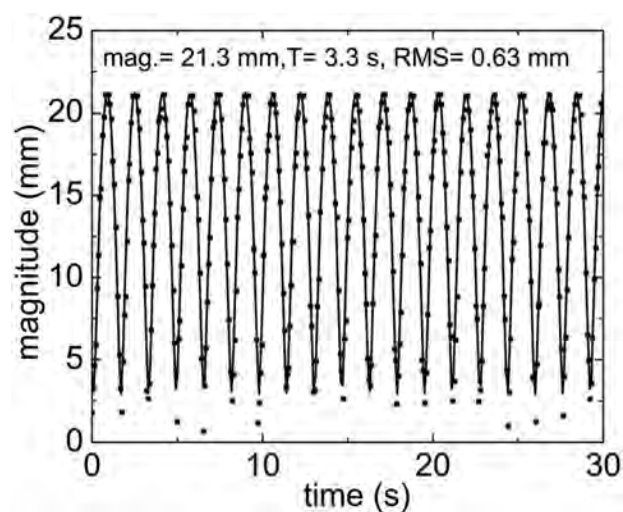


FIG. 6. Plot of magnitude of fiducial away from isocenter as a function of time. Solid curve is predicted motion with deviation between theoretical and experimental expressed as RMS.

further away from the system isocenter ( $d_{kV-d}=80$  cm) than the MV detector ( $d_{MV-d}=50$  cm), leading to increased magnification. As can be seen, it is found that the MV trace lags behind the kV trace by approximately  $\sim 70$  ms.

#### IV. DISCUSSION

A critical step in dealing with intrafraction tumor motion is the real-time monitoring of the tumor position. Despite intense research effort in attempting to utilize the inherent image features to extract real-time information of tumor motion, at this point, implantation of metallic or electromagnetic field based fiducials remains the most reliable way to accomplish the stated goal. In this work we have described a combined kV/MV fiducial tracking system using a commercially available Trilogy system. It allows us to monitor fiducial motion by use of the system's pre-equipped onboard imager and EPID.

The program used for fiducial detection has the flexibility of allowing a large number of different types of image analysis techniques to be applied with minimal programming effort. Although, by no means a fully optimized and robust solution for the clinic, the fiducial detection algorithm, was found to be adequate in providing a proof-of-concept that kV/MV tracking is indeed possible. The main weakness of the method used for fiducial segmentation and sequentially detection was it being intensity based in nature, and thus not robust against large intensity fluctuations. This may be problematic when the fiducial is moving in the vicinity of high density objects such as the bone that can have similar intensity values as the fiducial, resulting in loss of the tracking signal. Use of a ROI to remove any high contrast background objects from the analyzed area did correct this problem for the pelvic phantom used in this study, however, in actual patient situations, where fiducials can move below bony structure, loss of tracking signal may occur. In addition, an inherent problem with the use of EPID imaging is that the

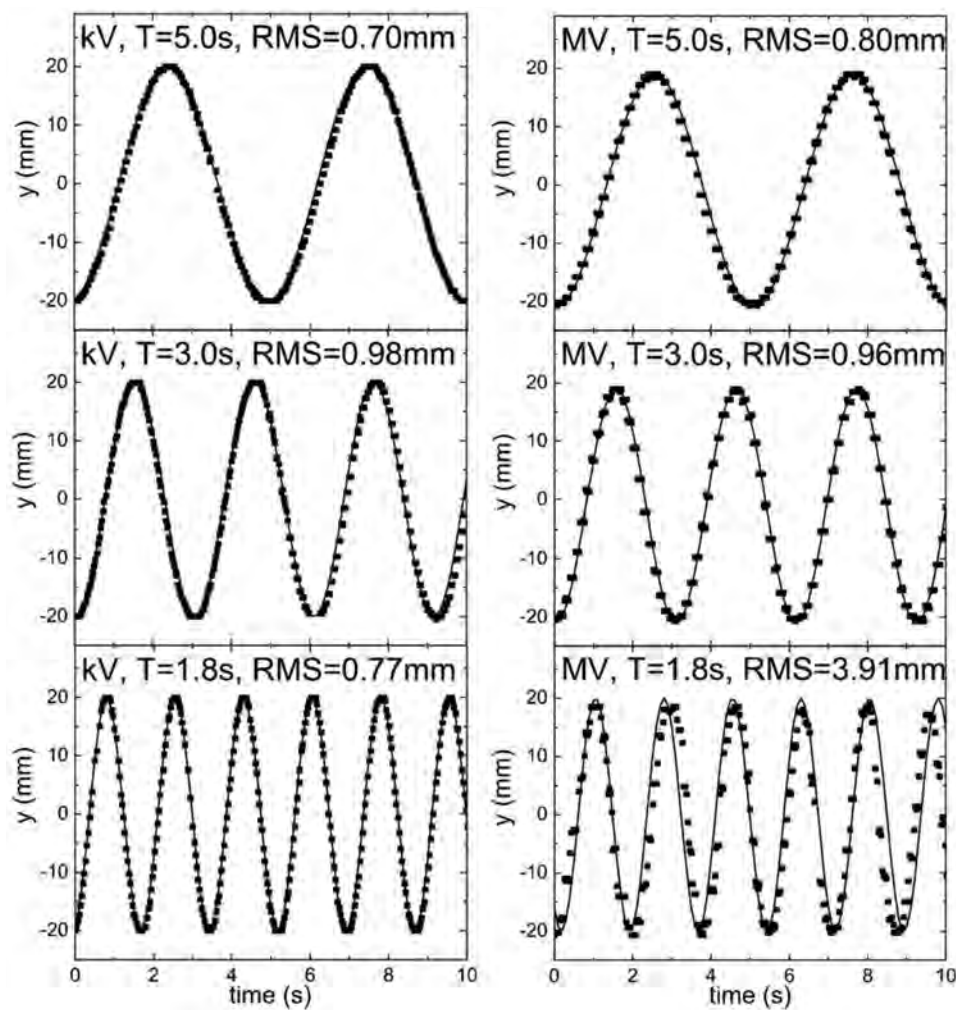


FIG. 7. Comparison of fiducial motion along the  $y$  axis at isocenter for the kV (left) and MV (right) detectors for different periods of oscillation. Solid curve is expected motion.

contrast between different material densities is significantly lower than with kV imaging. Even with the use of radio opaque markers as gold fiducials, the photon mass attenuation coefficient ratio  $(\mu/\rho)_{\text{Au}}/(\mu/\rho)_{\text{H}_2\text{O}}$  is near 1.0 at 1 MeV, compared to 30 at 100 keV. This poses a strong incentive in developing EPID image enhancement techniques targeted specifically to deal with poor material density distinction.

The 3.0 mm diameter stainless steel BB used in the study is larger than the gold fiducial markers used clinically (typically 1.2 mm in diameter and 3–5 mm in length). Due to the decrease in resolution as the frames are down converted from their native  $1024 \times 768$  format to  $640 \times 480$  for video based analysis, the subsequent worsening of image quality may make the use of the smaller clinical fiducials more problematic. For proof-of-concept demonstration that kV/MV tracking is feasible, it was decided that a more easy to detect 3.0 mm BB should be employed. It is, however, envisioned that detection of smaller cylindrical gold fiducials is possible at a near real-time speed provided that one can access the native  $1024 \times 768$  images directly captured by the kV and MV detectors. This would require cooperation with the

equipment manufacturer and will be investigated in future work. In addition, a more advanced fiducial detection algorithm will most likely be necessary for the successful implementation of the kV/MV tracking technique. Tang *et al.* have recently demonstrated tracking of multiple cylindrical fiducials through the use of pattern recognition and fiducial prediction.<sup>27</sup> Additionally, their algorithm allowed tracking of fiducials near or under high density objects. Under current investigation is a prior knowledge based adaptive method capable of temporal and spatial marker prediction. The technique is particularly valuable in locating the fiducials that are partially or completely blocked by the MLC at certain segments during the IMRT delivery. It is anticipated that this type of fiducial detection algorithm will be useful for the kV/MV tracking technique.

Currently, the ROI is manually defined by the operator through a process of visual inspection and identification of the fiducials in the kV and MV images. The ROI procedure is straightforward and can be done in less than a minute. This procedure can be further simplified by use of a pointer interface device, such as a computer mouse, to draw a ROI di-

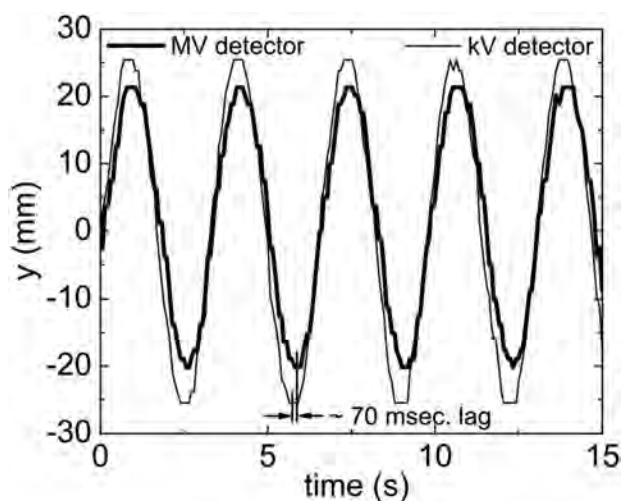


FIG. 8. Comparison of tracked real-time fiducial motion along the  $y$  axis as detected by the kV and MV detectors.

rectly on the image as opposed to manual entry through the keyboard. A more automated approach is to use an algorithm to examine the prior planning CT image data to locate the fiducials and to evaluate their motion on the kV and MV imagers. A ROI, large enough to encompass the entire range of motion for the fiducial, can then be automatically defined around each fiducial.

To investigate velocity response of kV/MV system, the 3 mm BB is oscillated at various sinusoidal frequencies as plotted in Fig. 7. As can be seen, for periods approximately  $T \geq 3$  s, the detected pixel location of the fiducial corresponds well to the theoretically predicted position of a generated sinusoidal function with the corresponding amplitude and period set by the movable platform. For  $T < 3$  s, it is found that the kV detector is able to maintain a high fiducial tracking accuracy, whereas, the detected positions of the fiducial from the MV detector is found to deviate from the predicted ones. Visual observation of the kV and MV detector video streams reveals this as resulting from motion induced blurring. For all periods of oscillation produced by the motion stage it is seen that the kV detector accurately captures an image of the spherical BB without distortion. This is in contrast to the MV detector, where it is seen that for  $T = 1.8$  s, the spherical shape of the BB becomes elongated along the direction of motion. The image distortion is found to be most severe during mid, or the highest velocity, portion of the oscillation curve. In the  $T = 1.8$  s case, this corresponds to a BB velocity of  $\sim 7$  cm/s at midoscillation. The elongated BB image resulted in a larger detected pixel group, leading to an erroneous center-of-mass pixel calculation. A motion restoration algorithm may be useful in this situation to deblur motion artifacts. However, in real patient scenarios, the maximum tumor velocity is generally observed to be less than 4 cm/s. As shown by the  $T = 3.0$  s (maximum velocity  $\sim 4.2$  cm/s) case, the response speed of the imagers should be adequate for most clinical situations.

As shown in Fig. 5, for a particular sinusoidal wave set by the moving stage, the kV/MV tracking system measures a similar function that is found to differ no more than 1 mm RMS. Considering the 0.2 mm RMS error generated by the platform, it can be assumed that the kV/MV system is measuring with an actual RMS under the reported values in Fig. 5. This is expected due to the detector pixel sizes being measured at  $\sim 0.85$  and  $\sim 0.67$  mm/pixel at the surface of the detector, even with a down converted image frame ( $1024 \times 768$  to  $640 \times 480$ ). With the amplification factor ( $\sim 1.5$  in the kV/MV system) the pixel size is further reduced to  $\sim 0.57$  and  $\sim 0.44$  mm/pixel at the isoplane for the kV and MV imagers, respectively. These accuracy numbers are expected to further increase once full image frames at their native  $1024 \times 768$  can be captured without down conversion.

As pointed out in a previous work,<sup>28</sup> mechanical and electronic response times, that may be acceptable in 3D RT, can limit the precision of dose delivery in the 4D case. This is also seen in the presented kV/MV tracking system, which, as detailed in Fig. 1, is comprised of two separate systems that each suffer from their own particular processing and electronic delay times. This manifests itself in the data of Fig. 8, where the phase of the MV signal lags behind the kV signal by approximately  $\sim 70$  ms. In calculating the fiducial coordinates using Eqs. (1)–(4), this lag will lead to positional errors since the EPID position ( $x_{MV}, y_{MV}$ ) is not in sync with the kV position ( $x_{kV}, y_{kV}$ ) for a particular CPU clock cycle. In general, this systematic error can be corrected for by pairing the current MV imager ( $x_{MV}, y_{MV}$ ) data with kV ( $x_{kV}, y_{kV}$ ) data retrospectively delayed by 70 ms. Fortunately, in this study, the 70 ms processing delay resulted in a negligible positional error for all periods of oscillation investigated. Consultation with the manufacture revealed a  $\sim 0.67$  ms delay time for the kV imaging system. Combined with the 70 ms MV imager lag and associated video processing time a total delay time of  $\sim 150$ – $200$  ms can be estimated. Since no prediction filters are used in the tracking system, the marker is measured with a  $\sim 150$ – $200$  ms time lag. For short periods, or fast velocities, these electronic response times may hamper the geometric accuracy of fiducial tracking. Adaptive motion prediction filters<sup>29–31</sup> may be useful in compensating for these electronic delay times. In general, response time is judged to be primarily a technological issue and will most likely be improved with the development of future fast response detector and image processing systems.

When using the pelvic phantom, it was found that scattered radiation from the treatment beam can blur the kV images. This is especially noticeable for isocenter-to-imager distances of  $d_{kV-d} < 70$  cm. The scattered MV radiation superimposes over the kV imaging beam at the kV  $aSi$  detector, making fiducial detection difficult. Increasing  $d_{kV-d}$  to 80 cm reduced the contribution of scattered MV photons, allowing detection of the fiducial using the aforementioned intensity based algorithm. Another potential solution for reducing the influence of the scattered MV radiation is the use of multiplexing through kV beam pulsation.<sup>32</sup> This technique

separates the kV source image from any MV scattered radiation, allowing  $d_{kV-d}$  distances of less than 70 cm to be used. Another potential method would be through controlled kV/MV beam switching (i.e., quick beam gating or pulsing), such that at a given instant of time, either the kV or MV source is on, but not both simultaneously. This would completely remove any MV radiation during the kV imaging process. It is also likely that the optimal kV/MV switching rate will be disease site dependent. For certain sites, such as the prostate, it is expected that the kV beam is needed less frequently.

## V. CONCLUSION

A real-time 3D fiducial tracking system using combined kV and MV imaging has been successfully demonstrated for the first time. This technique is especially suitable for RT systems already equipped with on board kV and EPID imaging devices. The geometric accuracy of the system is found to be on the order of 1 mm in all three spatial dimensions. Given its simplicity and achievable accuracy, the proposed approach, should find widespread clinical application in real-time monitoring of the tumor position and in providing a control signal to respiration-gated and even 4D radiation therapy.

## ACKNOWLEDGMENTS

This work was supported in part by grants from the Komen Breast Cancer Foundation (BCTR0504071) and National Cancer Institute (1R01 CA98523 and CA104205).

<sup>a)</sup>U.S. Patent pending (Stanford Office of Technology Licensing, Disclosure #S07-268)

<sup>b)</sup>Author to whom correspondence should be addressed. Present address: Stanford University School of Medicine, Department of Radiation Oncology, 875 Blake Wilbur Drive, Stanford, CA 94305-5847. Telephone: 1-650-498-7896; Fax: 1-650-498-4015. Electronic mail: r.wiersma@stanford.edu

<sup>1</sup>G. A. Ezzell *et al.*, "Guidance document on delivery, treatment planning, and clinical implementation of IMRT: Report of the IMRT subcommittee of the AAPM radiation therapy committee," *Med. Phys.* **30**, 2089–2115 (2003).

<sup>2</sup>L. Xing, Q. Wu, Y. Yong, and A. L. Boyer, in *Physics of IMRT and Inverse Treatment Planning in Intensity Modulated Radiation Therapy: A Clinical Perspective*, edited by A. F. Mundt and J. C. Roeske (BC Decker, Inc., Hamilton, Canada, 2005), pp. 20–51.

<sup>3</sup>H. Shirato *et al.*, "Intrafractional tumor motion: Lung and liver," *Semin. Radiat. Oncol.* **14**, 10–18 (2004).

<sup>4</sup>L. Xing *et al.*, "Overview of image-guided radiation therapy," *Med. Dosim.* **31**, 91–112 (2006).

<sup>5</sup>M. van Herk, "Errors and margins in radiotherapy," *Semin. Radiat. Oncol.* **14**, 52–64 (2004).

<sup>6</sup>J. Hanley *et al.*, "Deep inspiration breath-hold technique for lung tumors: The potential value of target immobilization and reduced lung density in dose escalation," *Int. J. Radiat. Oncol., Biol., Phys.* **45**, 603–611 (1999).

<sup>7</sup>H. D. Kubo *et al.*, "Breathing-synchronized radiotherapy program at the University of California Davis Cancer Center," *Med. Phys.* **27**, 346

(2000).

<sup>8</sup>S. S. Vedam *et al.*, "Determining parameters for respiration-gated radiotherapy," *Med. Phys.* **28**, 2139–2146 (2001).

<sup>9</sup>X. A. Li, C. Stepaniak, and E. Gore, "Technical and dosimetric aspects of respiratory gating using a pressure-sensor motion monitoring system," *Med. Phys.* **33**, 145–154 (2006).

<sup>10</sup>N. Wink *et al.*, "Individualized gating windows based on four-dimensional CT information for respiration gated radiotherapy," *Med. Phys.* **34**, 2384 (2007).

<sup>11</sup>A. Schweikard *et al.*, "Robotic motion compensation for respiratory movement during radiosurgery," *Comput. Aided Surg.* **5**, 263–277 (2000).

<sup>12</sup>P. J. Keall *et al.*, "A four-dimensional controller for DMLC-based tumor tracking," *Int. J. Radiat. Oncol., Biol., Phys.* **60**, S338–S339 (2004).

<sup>13</sup>C. Ozhasoglu, "Synchrony—Real-time respiratory compensation system for the CyberKnife," *Med. Phys.* **33**, 2245–2246 (2006).

<sup>14</sup>P. J. Keall *et al.*, "Motion adaptive x-ray therapy: A feasibility study," *Phys. Med. Biol.* **46**, 1–10 (2001).

<sup>15</sup>T. Neicu *et al.*, "Synchronized moving aperture radiation therapy (SMART): Average tumour trajectory for lung patients," *Phys. Med. Biol.* **48**, 587–598 (2003).

<sup>16</sup>L. Papiez, "The leaf sweep algorithm for an immobile and moving target as an optimal control problem in radiotherapy delivery," *Math. Comput. Modell.* **37**, 735–745 (2003).

<sup>17</sup>H. D. Kubo and B. C. Hill, "Respiration gated radiotherapy treatment: A technical study," *Phys. Med. Biol.* **41**, 83–91 (1996).

<sup>18</sup>C. Ozhasoglu and M. J. Murphy, "Issues in respiratory motion compensation during external-beam radiotherapy," *Int. J. Radiat. Oncol., Biol., Phys.* **52**, 1389–1399 (2002).

<sup>19</sup>L. Simon *et al.*, "Lung volume assessment for a cross-comparison of two breathing-adapted techniques in radiotherapy," *Int. J. Radiat. Oncol., Biol., Phys.* **63**, 602–609 (2005).

<sup>20</sup>S. S. Vedam *et al.*, "Quantifying the predictability of diaphragm motion during respiration with a noninvasive external marker," *Med. Phys.* **30**, 505–513 (2003).

<sup>21</sup>J. D. P. Hoisak *et al.*, "Correlation of lung tumor motion with external surrogate indicators of respiration," *Int. J. Radiat. Oncol., Biol., Phys.* **60**, 1298–1306 (2004).

<sup>22</sup>R. I. Berbeco *et al.*, "Integrated radiotherapy imaging system (IRIS): Design considerations of tumour tracking with linac gantry-mounted diagnostic x-ray systems with flat-panel detectors," *Phys. Med. Biol.* **49**, 243–255 (2004).

<sup>23</sup>H. Shirato *et al.*, "Real-time tumour-tracking radiotherapy," *Lancet* **353**, 1331–1332 (1999).

<sup>24</sup>P. Kupelian *et al.*, "Multi-institutional clinical experience with the Calypso System in localization and continuous, real-time monitoring of the prostate gland during external radiotherapy," *Int. J. Radiat. Oncol., Biol., Phys.* **67**, 1088–1098 (2007).

<sup>25</sup>P. J. Keall *et al.*, "On the use of EPID-based implanted marker tracking for 4D radiotherapy," *Med. Phys.* **31**, 3492–3499 (2004).

<sup>26</sup>Roborealm, <http://roborealm.com/>.

<sup>27</sup>X. L. Tang, G. C. Sharp, and S. B. Jiang, "Fluoroscopic tracking of multiple implanted fiducial markers using multiple object tracking," *Phys. Med. Biol.* **52**, 4081–4098 (2007).

<sup>28</sup>R. D. Wiersma and L. Xing, "Examination of geometric and dosimetric accuracies of gated step-and-shoot intensity modulated radiation therapy," *Med. Phys.* **34**, 3962–3970.

<sup>29</sup>G. C. Sharp *et al.*, "Prediction of respiratory tumour motion for real-time image-guided radiotherapy," *Phys. Med. Biol.* **49**, 425–440 (2004).

<sup>30</sup>S. S. Vedam *et al.*, "Predicting respiratory motion for four-dimensional radiotherapy," *Med. Phys.* **31**, 2274–2283 (2004).

<sup>31</sup>M. J. Murphy, "Tracking moving organs in real time," *Semin. Radiat. Oncol.* **14**, 91–100 (2004).

<sup>32</sup>J. Zhang *et al.*, "Multiplexing radiography for ultra-fast computed tomography: A feasibility study," *Med. Phys.* **34**, 2527 (2007).